

Basic creep and autogenous shrinkage of Limestone Calcined Clay Cement (LC³)

Thèse N° 9321

Présentée le 3 mai 2019

à la Faculté des sciences et techniques de l'ingénieur
Laboratoire des matériaux de construction
Programme doctoral en science et génie des matériaux

pour l'obtention du grade de Docteur ès Sciences

par

Julien STON

Acceptée sur proposition du jury

Prof. V. Michaud, présidente du jury
Prof. K. Scrivener, directrice de thèse
Prof. L. Sorelli, rapporteur
Prof. V. Mechtcherine, rapporteur
Prof. E. Brühwiler, rapporteur

2019

Somewhere, something incredible
is waiting to be known.

— Carl Sagan

Acknowledgements

Warm thanks to the Swiss Agency for Development and Cooperation for supporting the LC³ project, whose this thesis is part of, and to Karen for the opportunity to work in her fabulous lab. Many thanks also to the members of my jury for their time and feedback.

Big thanks to the actual PhD students team for keeping the bright atmosphere in the lab! Wioletta, Franco for your discussions and (bad) jokes, Anna for your everyday energy, Solène for the café-caramel, Yosra, Mahsa, Sarra, Yu, Maya (the young) and Gabie for the puns and the American dream, Masood, Andrea and Qiao.

I had the chance to work with many students and interns: Vincent, Kilian and Margot, Delphine, Eléonore, Aigoul, Joanne, Jessica and Eléonore, Benoît, Pablo, Romans, Edgar and George. Your efforts will be remembered!

The LC³ project unites many researchers throughout the world, and I could meet amazing people: Fernando, Adrian, Abdel and Roger from Cuba, Anuj, Sreejith, Yuvaraj, Arun, Sundar, Ravindra and Manu from far India. The local, past and present LC³ team also provided great discussions and interactions: many thanks to François, Mink, Franco, Silas, Hamed, Aurélie and Rob.

LMC would collapse without the brainpower of all its post-docs! Huge thanks to François for the precious inputs and exotic trips, William for the ideas and accent, Élise for absolutely everything, Emmanuelle for the compulsory coffee breaks, Diana for the good mood and Fabien for his rigorous nerdiness! But also, thanks to Xuerun for the passion, the spirit and – of course – the XRD, Aurélie for the intense concrete casting, Hamed for the coolness, BBQ and forward thinking, Adrien for the help with everything, Cyrille for the code and his availability, and (drum roll) Hadi for the crazy discussions, hikes, dinners and what not!

Specials thanks to Mateusz at EMPA for his always interesting inputs and dialogue and above all Lily for the precious heritage you left me.

I have been around LMC since 2011... Needless to say that I met quite a few people! Many many thanks to Amélie for the support and the rest, John for the IT poison gift (just joking!), Julien, Mariana, Paweł, Cédric, Christophe, Théo, Mo, Arnaud for the random chats and trips.

Le "L" de LMC veut dire Lionel. Il est les bras et les jambes du labo (pas le dos). C'est lui qui vient te débusquer au sous-sol pour résoudre un problème Matlab et qui se décarcasse pour que ton set-up ronronne comme un chat. Merci Lionel pour tes coups de mains, tes vieilles blagues et surtout tes bonnes idées, et merci à ton équipe : Jean, Tonio, Paul et les apprentis pour être là quand il faut.

I had the privilege to share my office with amazing colleagues and friends: Julien and his everyday class (e grazie ancora per l'aiuto con \LaTeX), Berta with her bright laughter and good advices, Alex the greatest thinker, astronomer and friend I met at LMC, Shiyu the quiet, and Khalil (t'as une question ?) with his perpetually positive attitude.

Bien sûr, un immense merci à Maude, Anne-Sandra, Mirabella et Marie-Alix pour leurs talents d'organisation et les discussions autour d'un café.

Et encore merci à Maude, Élise et Alex, la "green running team" pour tous ces moments passés à rire, discuter, courir ou simplement manger ! Ces 4 ans (et quelques) n'auraient pas été pareils sans vous :)

Extra kudos to Élise and John for the (complete!) proof reading!
And of course, my deepest thanks to my family and friends for their constant support. Surtout, merci à toi Lætitia pour ton soutien inusable durant ces années !

Lausanne, 3 mai 2019

J.S.

Abstract

The use of supplementary cementitious materials (SCM) to lower the clinker factor of cements is now commonplace, for it benefits performance, economics and ecology. This thesis focuses on ternary blends of limestone and calcined kaolinitic clays, two very promising SCM thanks to their worldwide availability. In particular, this research aims to get an insight on the delayed strains in sealed condition of such binders, christened LC^3 for Limestone - Calcined Clay Cement. Delayed strains refer to time-dependent deformations undergone by the material during its lifetime, such as *shrinkage* and *creep*.

This work evaluates the impact of the calcined kaolinite content of the clay — which can vary in accordance with the origin of the clay — on the autogenous shrinkage and basic creep properties of LC^3 . Compressive creep tests on mature paste samples indicated that the presence of limestone and calcined clay dramatically reduced creep compliance. This reduction is significant even with lower grade clays and does not depend on the clay purity if it has at least 40% of calcined kaolinite. A two-dimensional finite elements model was used to simulate the creep response of the tested microstructures in order to try to determine whether the compliance reduction originated from a different phase assemblage or a higher viscosity of the C–S–H. The outputs pointed towards a different rheology of C–S–H gel.

Autogenous shrinkage measurements on LC^3 binders showed that these ternary blends had a lower or comparable shrinkage to plain cement reference during the two first months of hydration. Shrinkage rate and amplitude was found to be close for LC^3 mixes using medium to high grade clays of natural origin. A study of the evolution of microstructure with shrinkage demonstrated that if the calcined clay contained enough metakaolin to consume most of the available portlandite, the porosity and desaturation of the microstructure were very similar regardless of the clay. As these features play a large role on the origin of shrinkage force, the macroscopic response is comparable among these specific mixes.

Keywords: Limestone, calcined clay, basic creep, autogenous shrinkage, modelling

Résumé

L'utilisation de matériaux cimentaires de substitution (SCM) est désormais un moyen répandu de limiter le contenu en clinker d'un ciment, tout en apportant des bénéfices de performance, économiques et écologiques. Ce travail de thèse se concentre sur les liants ternaires à base de calcaire et d'argiles kaolinitiques calcinées, deux substituts à fort potentiel grâce à leur disponibilité dans le monde entier. Cette recherche tente en particulier d'examiner les déformations différées en environnement scellé de ce genre de liants, baptisés LC^3 pour Limestone - Calcined Clay Cement. Les déformations différées se réfèrent aux changements dimensionnels subis par le matériau durant son cycle de vie, tels le *retrait* et le *fluage*.

Ce travail a pour but d'évaluer l'impact du contenu en kaolinite calcinée de l'argile — qui peut largement varier en fonction de sa provenance — sur le retrait endogène et le fluage propre des LC^3 . Des essais de fluage en compression sur pâte de ciment mature ont indiqué que la présence de calcaire et d'argile calcinée réduit considérablement la complaisance. Cette diminution est présente également avec des argiles de moindre qualité et ne dépend pas du contenu en kaolinite calcinée, si celui-ci est supérieur à 40% environ. Le comportement en fluage des microstructures testées a été modélisé par éléments finis pour tenter de déterminer si la réduction de complaisance provenait d'un assemblage de phases différent ou d'un C-S-H plus visqueux. Les résultats pointent vers une rhéologie différente du gel de C-S-H.

Les mesures de retrait endogène sur les liants LC^3 ont montré que ces mélanges ternaires subissaient moins ou autant de retrait que les ciments de référence durant les deux premiers mois d'hydratation. Le taux et l'amplitude du retrait sont similaires pour des LC^3 contenant des argiles d'origine naturelle de moyenne ou haute qualité. Une analyse de l'évolution de la microstructure au cours du retrait a démontré que, si l'argile calcinée contient suffisamment de metakaolin pour consommer la majeure partie de la portlandite disponible, la porosité et la désaturation du réseau poreux sont similaires pour toute argile. Étant donné que ces caractéristiques jouent un grand rôle sur l'origine des forces de retrait, la réponse macroscopique est comparable pour ces mélanges particuliers.

Mots-clé : Calcaire, argile calcinée, fluage propre, retrait endogène, modélisation

Riassunto

L'uso di materiali cementizi supplementari è ormai un modo diffuso per limitare la proporzione di clinker nel cemento, mentre ne favorisce robustezza, costo e impatto sull'ambiente. Questa tesi si concentra su leganti ternari a base di calcare e argilla caolinica calcinata, due sostituti ad alto potenziale per via della loro disponibilità in tutto il mondo. Questa ricerca tenta in particolare di esaminare le deformazioni differite in condizione endogena di tali leganti, battezzati LC^3 , per Limestone - Calcined Clay Cement. Le deformazioni differite riguardano le variazioni di dimensioni subite da un materiale durante il suo ciclo di vita, come il *ritiro* e lo *scorrimento* (creep).

L'obiettivo di questo lavoro è di valutare l'impatto del contenuto in caolinite calcinata dell'argilla — che può variare ampiamente secondo la sua origine — sul ritiro endogeno e lo scorrimento proprio degli LC^3 . Misure di scorrimento in compressione su paste di cemento mature hanno indicato che l'aggiunta di calcare e argilla calcinata diminuiva considerevolmente la *compliance*. Questa diminuzione si osserva pure con argille di minore qualità e non dipende del suo contenuto in caolinite calcinata se superiore a circa 40%. Il comportamento viscoso delle microstrutture testate è stato simulato tramite un'analisi agli elementi finiti per determinare se la riduzione di *compliance* derivava da un assemblaggio diverso delle fasi o da un C-S-H più viscoso. I risultati puntano verso una reologia differente del gel di C-S-H.

Le misure di ritiro endogeno su i leganti LC^3 hanno indicato che questi subivano un ritiro inferiore o uguale ai cementi di riferimento durante i due primi mesi d'idratazione. La velocità e l'ampiezza del ritiro sono simili per gli LC^3 contenenti argille di origine naturale di media o alta qualità. Un'analisi dell'evoluzione della microstruttura al corso del ritiro ha dimostrato che se l'argilla conteneva abbastanza metacaolino per consumare tutta la portlandite disponibile, la porosità e la desaturazione della rete porosa erano simili per qualsiasi argilla. Dato che queste caratteristiche svolgono un ruolo importante sull'origine delle forze di ritiro, la risposta macroscopica è paragonabile per questi leganti particolari.

Parole chiave : Calcare, argilla calcinata, scorrimento proprio, ritiro endogeno, modellizzazione

Contents

Acknowledgements	v
Abstract (English/Français/Italiano)	vii
Table of contents	xv
List of figures	xix
List of tables	xxi
Glossary	xxiii
1 Introduction	1
1.1 Preamble	2
1.2 Limestone and Calcined Clay Cements	3
1.2.1 The calcined kaolinite content	4
1.3 Goals of this project	5
1.4 Structure of the thesis	6
1.5 References	7
2 Materials and methods	9
2.1 Raw materials	10
2.1.1 Chemical and physical properties	10
2.1.2 Mix designs	12
2.2 Microstructure characterization	13
2.2.1 Scanning electron microscopy and energy dispersive spectroscopy	13
2.2.2 X-Ray diffraction, Rietveld quantification and mass balance	16
2.2.3 Mercury intrusion porosimetry	19
2.2.4 Saturation degree of the porosity	20
2.3 Mechanical properties	22
2.3.1 Compressive strength	22
2.3.2 Young's modulus	22
2.4 References	26
3 Basic creep on mature paste samples	27

Contents

3.1	Literature review	29
3.1.1	Creep mechanisms in cement	29
3.1.2	The role of supplementary cementitious materials	32
3.1.3	Creep modelling	35
3.1.4	Basic creep and autogenous shrinkage	37
3.2	Experimental methods	38
3.2.1	Sample preparation	38
3.2.2	Compressive creep frames	38
3.2.3	Results processing	39
3.2.4	Basic creep kinetics	39
3.3	Experimental results	43
3.3.1	Influence of cement type	43
3.3.2	LC ³ with natural calcined clays	45
3.3.3	Influence of initial water content	48
3.3.4	Model clays	50
3.3.5	Fitting results	52
3.3.6	Creep rate and microstructure	54
3.3.7	Summary of the results	56
3.4	Modelling	57
3.4.1	Finite Elements Modelling	57
3.4.2	Rheological modelling	65
3.5	Conclusions	69
3.6	References	72
4	Autogenous shrinkage	77
4.1	Literature review	79
4.1.1	Shrinkage mechanisms	79
4.1.2	Measurement methods	82
4.1.3	Autogenous shrinkage modelling	84
4.2	Experimental methods	89
4.2.1	Autogenous shrinkage measurement	89
4.2.2	Relative humidity	90
4.3	Experimental results	91
4.3.1	Influence of cement type	91
4.3.2	Influence of initial water content	94
4.3.3	Natural calcined clays	96
4.3.4	Model clays	99
4.3.5	Average pore pressure	101
4.4	Shrinkage and microstructure evolution	102
4.5	Modelling	105
4.5.1	Numerical scheme	105
4.5.2	Inputs of the model	105

4.5.3 Model output and discussion	110
4.6 Conclusions	112
4.7 References	113
5 Conclusions and future perspectives	117
5.1 Basic creep of LC ³ mature paste	118
5.1.1 Experimental part	118
5.1.2 Creep kinetics and microstructure	118
5.1.3 Basic creep modelling	119
5.1.4 Perspectives	120
5.2 Autogenous shrinkage	122
5.2.1 Experimental part	122
5.2.2 Shrinkage and hydration	122
5.2.3 Autogenous shrinkage modelling	123
5.2.4 Perspectives	123
5.3 Closing words	124
5.4 References	124
A Experimental data processing	125
A.1 References	126
B Data on concrete	127
B.1 Materials and method	127
B.2 Experimental results	127
List of publications	129
Curriculum Vitae	131

List of Figures

1.1	Greenhouse gases emissions by sectors	2
1.2	Calcined kaolinite content and mechanical properties	4
2.1	Comparison of EDS protocols	14
2.2	Example of volume balance	18
2.3	Mercury intrusion porosimetry	19
2.4	Saturation level of porosity	20
2.5	Evolution of Young's modulus	25
3.1	Power and Brownyard C–S–H model	31
3.2	CM-II C–S–H model	31
3.3	Feldman and Sereda C–S–H model	32
3.4	Effects of metakaolin on C–S–H chemistry	33
3.5	Creep of concrete with metakaolin	34
3.6	Creep rate at different loading ages	35
3.7	Example of multiscale modelling	37
3.8	Scheme of the compressive creep set-up	39
3.9	Example of processed creep strain data	40
3.10	Fitting of first derivative	41
3.11	Examples of first derivative integration	42
3.12	Creep compliance of plain cement paste mixes	43
3.13	Creep compliance of plain cement and LC ³ mixes	44
3.14	Creep properties of plain cement and LC ³ mixes cast with different cements	44
3.15	Creep compliance of LC ³ -50 mixes with different grades of clay	45
3.16	Creep properties of LC ³ -50 mixes with different grades of clay	46
3.17	Creep compliance of the LC ³ -50 and LC ³ -65 mixes with varying clay content	47
3.18	Creep properties of the LC ³ -50 and LC ³ -65 mixes with varying clay content	47
3.19	Creep compliance of mixes with different W/B	48
3.20	Creep properties of mixes with different W/B	49
3.21	Creep compliance of LC ³ -50 type mixes using model clays	50
3.22	Creep properties of of LC ³ -50 type mixes using model clays	51
3.23	Creep rate for all mixes	53
3.24	Creep amplitude from the power law fit versus C–S–H content	54

List of Figures

3.25 Creep amplitude from the logarithmic fit versus C–S–H content	55
3.26 Creep amplitude compared to C–S–H composition	55
3.27 Creep amplitude factor compared to initial metakaolin content	56
3.28 Schematic of the 2D FE microstructure	58
3.29 Visualisation of Gaussian random fields	59
3.30 Example of FEM results processing	62
3.31 C–S–H compliance of the cement mixes	62
3.32 C–S–H compliance of the LC ³ -50 mixes with natural clays	63
3.33 C–S–H compliance of the LC ³ -65 mixes	63
3.34 C–S–H compliance of the LC ³ -50 with model clays	64
3.35 Creep compliance at different loading ages	66
3.36 Diagram of the Kelvin-Voigt model used	67
3.37 Evolution of the springs stiffness	68
3.38 Fit using the rheological model	68
3.39 Contact creep modulus versus Al content in C–S–H matrix	70
4.1 Schematic of disjoining pressure mechanisms	80
4.2 Illustration of capillary pressure	82
4.3 Example of autogenous shrinkage results	84
4.4 Summary of Hu's results on autogenous shrinkage modelling	88
4.5 Corrugated tubes set-up	89
4.6 Autogenous shrinkage during 56 days of plain cement paste mixes	91
4.7 Autogenous shrinkage during 28 days for mixes with different cements	92
4.8 Autogenous shrinkage during 56 days of LC ³ -50 and plain cement samples with comparable mix designs	93
4.9 Autogenous shrinkage during 28 days for mixes with different initial water content	94
4.10 Autogenous shrinkage during 56 days of samples with varying water content	95
4.11 Autogenous shrinkage of LC ³ -50 samples with natural clays	96
4.12 Autogenous shrinkage during 56 days of LC ³ -50 and LC ³ -65 samples with varying clay content	97
4.13 Internal relative humidity evolution of LC ³ -50 and LC ³ -65 mixes	98
4.14 Autogenous shrinkage during 28 days for mixes with model clays	99
4.15 Internal relative humidity during 28 days for the model clay systems	100
4.16 Autogenous shrinkage during 56 days of the model clay systems	100
4.17 Autogenous shrinkage compared to average pore pressure	101
4.18 Autogenous shrinkage compared to main phases hydration for LC ³ -50 2:1 mixes	102
4.19 Autogenous shrinkage compared to main phases hydration for LC ³ -65 mixes and model mix MQ95	103
4.20 Autogenous shrinkage compared to main phases hydration for plain cement and model LC ³ -50 using white cement	104
4.21 Degree of hydration over time	106
4.22 Evolution of RH _k	107

4.23 Evolution of the saturation level	107
4.24 Evolution of the average pore pressure	108
4.25 Evolution of Young's modulus	109
4.26 Autogenous shrinkage modelling results	110
5.1 Creep amplitude factor compared to initial metakaolin content	118
5.2 Summary of the back-calculated C–S–H elastic properties	120
5.3 C–S–H compliance of the LC ³ -50 mixes with natural clays	121
5.4 Autogenous shrinkage compared to main phases hydration	123
B.1 Basic creep compliance and autogenous shrinkage of tested concrete	128

List of Tables

2.1	XRF composition of raw materials	10
2.2	XRF composition of calcined clays	11
2.3	Phase assemblage of the cements	11
2.4	Detailed mix designs for the plain cement and LC ³ -50	12
2.5	Detailed mix designs for the LC ³ -65 group	13
2.6	Detailed mix designs for the model clays group	13
2.7	Average C–A–S–H composition at 28 days	15
2.8	Phase assemblage by volume for all samples at 28 days	17
2.9	Compressive strength at 28 days	22
2.10	Young's modulus at 28 days	24
3.1	Fitting results	52
3.2	Mechanical properties of the elastic phases	57
3.3	Results from the elasticity modelling	60
4.1	Summary of water content of some samples	94
B.1	Mix design of concrete samples	127

Glossary

Cement shorthand notation

C: CaO (Calcium Oxide) S: SiO₂ (Silicon dioxide) A: Al₂O₃ (Aluminium oxide)
F: Fe₂O₃ (Iron oxide) \$: SO₃ (Sulfate) H: H₂O (Water) c: CaCO₃

Abbreviation of materials and phases

OPC: Ordinary Portland cement

PC: Plain cement

SCM: Supplementary cementitious material(s)

LC³: Limestone calcined clay cement

HPC: High performance concrete

UHPC: Ultra high performance concrete

C₃S: Tricalcium silicate

C₂S: Dicalcium silicate

C₃A: Tricalcium aluminate

C₄AF: Tetracalcium aluminoferrite

C\$H₂: Gypsum

AS₂ or MK: Metakaolin

CC : Calcined clay

Cc: Calcium carbonate (calcite)

LS : Limestone (calcite)

C–S–H: Calcium silicate hydrate

CH: Calcium hydroxide (portlandite)

Ett: Ettringite

Glossary

Ms: Monosulfoaluminate

Mc/Hc: Mono- / Hemicarboaluminate

Ht: Hydrotalcite

Hg: Ferrous hydrogarnet

SP: Superplasticizer

Abbreviations of techniques

MIP: Mercury intrusion porosimetry

SEM: Scanning electron microscopy

EDS: Energy dispersive X-Ray spectroscopy

BET: Brunauer-Emmett-Teller

XRF : X-Ray fluorescence

XRD: X-Ray diffraction

EMM-ARM: Elastic modulus measurement through ambient response method

LVDT: Linear variable differential transformer

Miscellaneous abbreviations

W/C: Water to cement ratio

W/B: Water to binder ratio

W/S: Water to solid ratio

RH: Relative humidity

PSD: Particle size distribution

LOI: Loss on ignition

FEM: Finite element method

AMIE: Automated mechanics for integrated experiments

RMSE: Root-mean-square error

1 Introduction

This chapter sets the context of this thesis. It briefly presents the state of the research in the field and sets the goals of this work. In addition, the structure of the thesis is presented, along with a brief summary of each chapter.

Contents

1.1 Preamble	2
1.2 Limestone and Calcined Clay Cements	3
1.2.1 The calcined kaolinite content	4
1.3 Goals of this project	5
1.4 Structure of the thesis	6
1.5 References	7

1.1 Preamble

Concrete is to this day the most modern and widespread construction material. It is the trademark of industrialized society, and no other class of material could compete with concrete. Its availability, ease of production, cost and environmental impact make it the best choice for most applications. In spite of its low ecological footprint, the extensive amount of concrete manufactured yearly brings a significant contribution to the anthropic CO₂ emissions and consumption of natural resources. As a reference, in 2010 the building sector was responsible for about 6.4% of the total CO₂-equivalent emissions for that year [1]. This is about half of the contribution due to the transport sector, and it is estimated that about twice as much CO₂-equivalent is emitted *yearly* solely to bring heating and power to the existing buildings. More recent studies indicated that the cement sector could be responsible for up to 8% of the global CO₂ emission when including direct emission from fuel burning, indirect emissions from electricity production and land-use change [2]. For these reasons, even slight improvements in the building sector can have a significant impact on a global scale. In addition, even though cement has a very similar composition to the Earth's crust, the availability of the raw materials is not boundless.

Fortunately, the cement industry started to address some of these issues at the beginning of the production chain already decades ago. One of the most efficient solutions — which brings economic and performance advantages as well — is to blend clinker from the cement kiln with other reactive materials, called supplementary cementitious materials (SCM). One has to know that a large part of the CO₂ emissions associated to cement production comes from the high-temperature calcination: energy is required to keep the kiln at around 1500°C and CO₂ is released during limestone decarbonation. Replacing part of the clinker in a binder with a material requiring less processing is therefore an easy way to lower the greenhouse gases

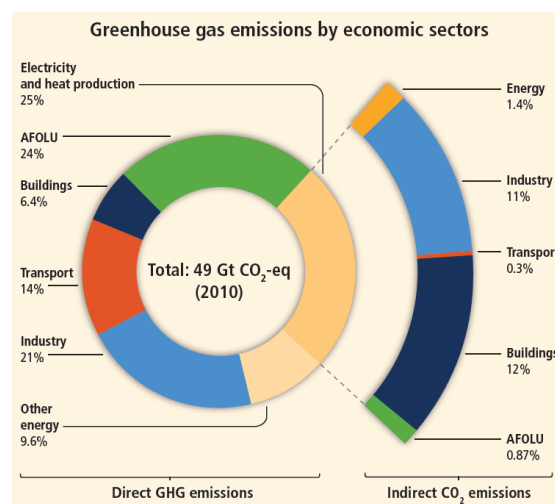


Figure 1.1 – Total anthropogenic greenhouse gas (GHG) emissions from economic sectors in 2010. AFOLU stands for agriculture, forestry and other land use. Adapted from [1].

emissions. These materials are generally by-products of other sectors, such as blast-furnace slag from steel industry or fly ashes from coal power plants, which, when correctly processed, show some valuable cementing properties. Alas, the production of currently used SCM is far from enough to meet the demand from the cement sector, leaving very little room for further improvement. Moreover, only a fraction of the fly ashes is actually suitable as SCM and its production should drop in the decades to come, as burning coal is a very unsustainable energy source. Slag production is declining as well as steel is getting more and more recycled [11].

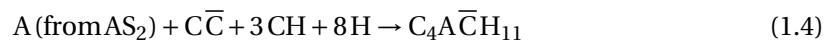
Nevertheless, there are two sources of SCM found in abundance and in most regions of the world: limestone and clays. Depending on their chemical purity, they can be source material for clinker production, or simply considered as mine tailings. Blended individually with cement, they bring only very modest improvement to performance, mostly coming from the filler effect. However, upon correctly selecting and processing the clay, it becomes a valuable SCM together with limestone.

1.2 Limestone and Calcined Clay Cements

In a binary mix, limestone mostly acts as a filler [8], promoting the precipitation of hydrates through extra surface for nucleation [9], [7]. When used in conjunction with C₃A-rich Portland cement, carboaluminate hydrates will form instead of sulphoaluminate. Eq. 1.1 describes the precipitation of hemicarboaluminate, whereas Eq. 1.2 shows the precipitation of monocarboaluminate. A raw clay used as SCM has little to no interest, as it will only behave as a filler, and can possibly decrease workability. On the other hand, kaolinitic clays contain *kaolinite* (Al₂Si₂O₅(OH)₄), which will turn into amorphous and reactive *metakaolin* (AS₂ in cement notation) after calcination. Metakaolin is a pozzolana, meaning it can react with portlandite from clinker hydration and water to form Al-rich C-A-S-H (see Eq. 1.3). This further refines the porosity and increases strength and durability.



Pure metakaolin is quite an expensive SCM, as it is also a valuable material for industries other than construction. Using calcined kaolinitic clays as a source of metakaolin is a very inexpensive yet efficient way to add a pozzolanic component to a cement blend, as it was demonstrated by Fernandez [6]. Further studies by Antoni [3] showed that the combined presence of both limestone and calcined clay in a ternary blend caused some extra carboaluminate formation thanks to the supplementary aluminium supply from metakaolin. This reaction consumes some portlandite, so it can be interpreted as a supplementary pozzolanic reaction, see Eq. 1.4.



As this additional reaction only occurs when both components are present, it is known as a *synergetic reaction*. Such ternary blends have been christened *Limestone and Calcined Clay Cements*, or LC^3 for short.

1.2.1 The calcined kaolinite content

One of the latest works to this date within the LC^3 project at EPFL was carried out by Avet and — among many other findings — pointed up the overwhelming influence of the amount of metakaolin in the calcined clay on the mechanical properties [4]. The common feature between clays suitable for LC^3 is the presence of kaolinite. This mineral can be found in varying proportions and often accompanied by other clayey compounds. It appeared that the calcined kaolinite content was the main factor influencing strength in LC^3 mortar samples, at constant mix design.

It is important to stress that the influencing parameter is the *calcined kaolinite content* and not the initial kaolinite content. If calcination is carried out properly, those figures are identical, but it is not the case if not all the kaolinite is turned into metakaolin during the calcination process. It is therefore important to know the actual metakaolin content (or calcined kaolinite content) of a clay to assess its properties.

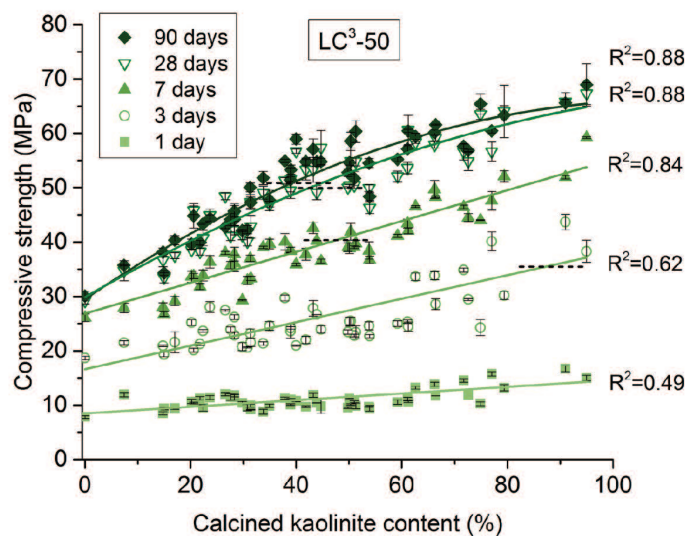


Figure 1.2 – This figure from [4] shows the dependency of compressive strength on calcined kaolinite content in the clay, especially when the pozzolanic reaction starts after about 3 days of hydration.

1.3 Goals of this project

The previously mentioned studies focused on the feasibility of limestone and calcined clay blends, the ongoing chemical reactions and the mechanical properties of such mixes. Durability against external chemical agents, such as chloride, was also assessed, showing very good results [12]. So far, the volume stability over time of such blends — what could be called *physical durability* — has only been marginally studied and reported [5]. Volume stability covers all sorts of time-dependent strains, in particular creep and shrinkage. Creep is defined as the progressive deformation of a material under a sustained load. This is the same phenomenon that causes stress relaxation when restricting a material to a given strain. Shrinkage and expansion of cementitious materials can have different origins, but a hydrating binder will undergo some shrinkage even when sealed from the environment and kept at constant temperature. This is called *autogenous shrinkage*.

Both shrinkage and creep can have a deleterious impact on the durability of structures, when not properly controlled. For instance, shrinkage can provoke cracks, which then become short-cuts for harmful chemical species. Creep on the other hand can relax shrinkage-induced strains, but also cause a loss of rebar tension in pre-stressed concrete. It is then primordial to know these behaviours in order to be able to build large and long-lasting structures. These properties have to be studied together, as shrinkage stress will cause creep and creep under external load will happen on top of on-going shrinkage.

SCM in general have a positive or neutral impact on the shrinkage and creep properties, which is attributed to a finer porosity thanks to the filler effect and additional hydration reactions from these materials [13]. Highly reactive pozzolans, such as silica fume, can however cause an increase of shrinkage, especially when used in high performance concrete with low W/B, as their reaction consumes a large amount of water.

Therefore, this study will try to get an insight on the creep and shrinkage properties of LC³ mixtures. These phenomena are part of the *delayed strains*, as they occur progressively over potentially long time scales. Keeping in mind the important role of the calcined kaolinite content on mechanical strength, this research is also carried out using a variety of kaolinitic clays of different origins and compositions. Experimental measurements are focused on paste samples, taking advantage of the varied microstructures and chemical compositions to potentially broaden knowledge of those phenomena. It is believed that the behaviour at the paste scale can be qualitatively applied at the concrete scale, as demonstrated by numerical modelling using homogenization schemes from paste to concrete scale [10]. Creep tests on LC³ samples with varied microstructure could also help identify the presence of viscous phases other than amorphous C–S–H, which is considered as the main phase responsible for creep. This study focused on delayed strains in sealed condition. The main reasons were the simpler control of the experimental conditions and to access intrinsic properties of the binders. The next section presents the layout of the thesis, together with a brief summary on the content of each chapter.

1.4 Structure of the thesis

Chapter 2 presents the materials and mix designs used throughout this study. The nomenclature used to differentiate the designs is also introduced. The physical and chemical characteristics of the anhydrous components and hydrating sample are regrouped in this chapter.

Chapter 3 concerns the investigation on basic creep behaviour of LC³ materials. The results of the compressive creep campaign are presented and interpreted to the light of microstructural properties. A finite element model is applied to the materials, followed by an analytical, poromechanical approach to obtain the viscous properties of the C-(A)-S-H gel.

Chapter 4 deals with autogenous shrinkage measurement. Its kinetics are compared to the evolution of microstructure. This strain is also a required input to process the basic creep results. An analytical model is used to try to predict the autogenous strain as the sum of elastic strain and viscous flow caused by the capillary forces.

Chapter 5 is the conclusive chapter. It summarizes the main findings from this research and proposes further paths to explore in order to answer the remaining questions.

The appendixes contain details about the numerical algorithm used to process the raw data and results on compressive creep of concrete samples.

1.5 References

- [1] Myles R Allen et al. “IPCC fifth assessment synthesis report-climate change 2014 synthesis report” (2014).
- [2] Robbie M Andrew. “Global CO₂ emissions from cement production”. en (2018), p. 23.
- [3] Mathieu Antoni. “Investigation of cement substitution by blends of calcined clays and limestone” (2013).
- [4] François Henri Avet. “Investigation of the grade of calcined clays used as clinker substitute in Limestone Calcined Clay Cement (LC3)” (2017), p. 169.
- [5] Yuvaraj Dhandapani et al. “Mechanical properties and durability performance of concretes with Limestone Calcined Clay Cement (LC3)”. *Cement and Concrete Research* 107 (May 2018), pp. 136–151.
- [6] Rodrigo Fernandez Lopez. “Calcined clayey soils as a potential replacement for cement in developing countries” (2009), p. 178.
- [7] Barbara Lothenbach et al. “Influence of limestone on the hydration of Portland cements”. *Cement and Concrete Research* 38.6 (2008), pp. 848–860.
- [8] Thomas Matschei, B Lothenbach, and Fredrik P Glasser. “The role of calcium carbonate in cement hydration”. *Cement and Concrete Research* 37.4 (2007), pp. 551–558.
- [9] Jean Péra, Sophie Husson, and Bernard Guilhot. “Influence of finely ground limestone on cement hydration”. *Cement and Concrete Composites*. Portland Limestone Cements 21.2 (1999), pp. 99–105.
- [10] Ch. Pichler and Roman Lackner. “A multiscale creep model as basis for simulation of early-age concrete behavior”. 2008.
- [11] Karen L Scrivener, Vanderley M John, and Ellis M Gartner. “Eco-efficient cements: Potential economically viable solutions for a low-CO₂ cement-based materials industry” (2016).
- [12] Karen Scrivener et al. “Calcined clay limestone cements (LC3)”. *Cement and Concrete Research*. Report of UNEP SBCI WORKING GROUP ON LOW-CO₂ ECO-EFFICIENT CEMENT-BASED MATERIALS 114 (Dec. 2018), pp. 49–56.
- [13] Michael Thomas. *Supplementary Cementing Materials in Concrete*. Anglais. CRC Press, 2013.

2 Materials and methods

In this chapter, all the materials used for the experimental parts are described, with a detailed chemo-physical characterization. This part also contains the nomenclature used to reference the different mix designs. The second part of the chapter deals with the main experimental techniques used to obtain the phase assemblage of the hardened paste samples. It also includes all the results from these techniques, as they will be useful for interpretation in the following chapters and as inputs for the models.

Contents

2.1 Raw materials	10
2.1.1 Chemical and physical properties	10
2.1.2 Mix designs	12
2.2 Microstructure characterization	13
2.2.1 Scanning electron microscopy and energy dispersive spectroscopy	13
2.2.2 X-Ray diffraction, Rietveld quantification and mass balance	16
2.2.3 Mercury intrusion porosimetry	19
2.2.4 Saturation degree of the porosity	20
2.3 Mechanical properties	22
2.3.1 Compressive strength	22
2.3.2 Young's modulus	22
2.4 References	26

2.1 Raw materials

Three CEM-I type cements were used as a base for the ternary blends: a laboratory cement from *Heidelberg Cement*, Normo 4 from *LafargeHolcim* and *Aalborg* white cement. All are 42.5N class cements. The first is produced in a dedicated kiln, with a very low variability of properties throughout the year, the others are commercial cements produced in Siggenthal (CH) for the Normo 4 and in Denmark for the Aalborg white. The limestone used to prepare LC³ was exclusively *Omya Durcal 5*, and the sulfate source was lab-grade gypsum from *Acros Organics* or *Merck*. The most variable component was naturally the calcined clay, as clays from different parts of the world and with varying chemical composition were used. The clays were gathered within the LC³ project, and where either received raw or already calcined. In the case of the raw clays, calcination was carried out at the laboratory in a static, lab-size kiln at 800°C for 60 minutes. If necessary, the materials were ground with a disc mill during 40 to 60 s, down to flour-like fineness.

2.1.1 Chemical and physical properties

Chemical characterization of all the mentioned components is obtained through XRF. Table 2.1 summarizes the oxide composition for cements, limestone and gypsum, whereas

Table 2.1 – Physical properties and main oxides composition of the raw materials (%wt)

Physical properties					
Component	Holcim Normo 4	Heidelberg LabCement	Aalborg white	Omya Durcal 5	Gypsum
Origin	CH	DE	DK	FR	EU
D _{v,50} (µm)	13	14.3	9.8	7.2	-
BET spec. surf. (m ² /g)	1.15	0.98	0.93	1.8	-
Specific gravity (g/cm ³)	3.1	3.3	3.2	2.86	2.31
Oxide composition					
SiO ₂	20.45	19.08	24.40	0.11	0
Al ₂ O ₃	4.39	5.31	2.16	0	0
Fe ₂ O ₃	3.01	3.77	0.32	0.04	0
CaO	64.48	64.45	68.12	54.96	32.57
MgO	1.66	1.66	0.56	0.15	0
SO ₃	2.83	3.12	1.94	0.03	46.51
Na ₂ O	0.24	0.28	0.05	0.06	0
K ₂ O	0.89	1.24	0.06	0.01	0
TiO ₂	0.34	0.27	-	0.01	0
P ₂ O ₅	0.28	0.28	-	0.00	0
Mn ₂ O ₃	0.05	0.06	-	0.00	0
LOI	1.3	0.75	0.91	42.50	20.93

2.1. Raw materials

Table 2.2 – Summary of the main physical and chemical properties of the calcined clays. The code for the region of origin is: North America (N-Am), South America (S-Am), South Asia (S-As), South-East Asia (SE-As) and Europe (Eu)

Physical properties							
Origin	N-Am	S-Am	SE-As	S-As	S-Am	Eu	Quartz
Calcined kaolinite content (by mass)	95%	60%	50%	45%	25%	15%	0%
$D_{v,50}$ (μm)	5.10	7.72	10.90	5.03	6.12	25.10	11.20
BET (m^2/g)	9.60	46.9	45.70	9.19	14.1	4.70	1.20
Specific gravity (g/cm^3)	2.2	2.5	2.5	2.5	2.5	2.5	2.65
Oxide composition							
SiO_2	52.00	48.13	44.90	49.74	63.66	63.65	99.80
Al_2O_3	43.80	35.08	32.30	41.78	24.16	15.71	-
Fe_2O_3	0.30	9.44	15.40	0.20	4.05	4.53	-
CaO	-	0.81	1.30	0.11	0.13	7.72	-
MgO	-	0.52	0.80	2.32	0.49	2.64	-
SO_3	0.10	0.02	0.10	0.26	1.31	0.58	-
Na_2O	0.30	0.20	0.40	0.09	0.61	0.37	-
K_2O	0.10	0.08	0.20	3.42	2.51	2.64	0.10
TiO_2	1.50	2.27	2.40	0.04	0.72	0.63	-
P_2O_5	0.20	0.34	0.40	0.09	0.40	0.22	-
Mn_2O_3	-	-	0.10	0.02	-	0.02	-
Other	0.10	0.01	0.20	0.05	0.02	0.16	-
LOI	1.50	2.98	1.70	1.85	1.75	1.04	0.10

Table 2.2 concentrates data from the various clays. The main difference among the clays is their calcined kaolinite content, ranging from about 15% to 95%. As explained in the previous chapter, this sole parameter is a very reliable indicator of the performance a calcined clay. Powder fineness and density have a major role in mix design of cementitious mixes, as they heavily influence workability and water to solid ratio. Phase assemblage of the cement powders from XRD-Rietveld quantification is presented on Table 2.3. All three cement used show a similar alite content.

Table 2.3 – Phase assemblage from XRD-Rietveld for the used cements, in %wt. The value for C_3A is the sum of orthogonal cubic varieties.

Phase	Holcim Normo 4	Heidelberg LabCement	Aalborg White
Alite C_3S (M3)	69.0	68.6	68.8
Belite $\beta\text{-C}_2\text{S}$	8.3	6.2	23.9
C_3A (o+c)	6.7	8.1	3.3
C_4AF	8.2	10.6	0.0

2.1.2 Mix designs

The LC³ family of binders offers a wide variety of mix designs to suit the performance, material quality or cost constraints of most situations. In this study, the main mix design used was the LC³-50 2:1, containing about 50% clinker, 30% calcined clay, 15% limestone and 5% gypsum. The number following "LC³" denotes to amount of clinker in the mix and the following pair of numbers represents the calcined clay to limestone ratio. No prefix is added to the mix design code when using Heidelberg LabCement. The prefixes *N4* or *W* are used when the mixes are prepared with Normo 4 or Aalborg white, respectively. On some measurements sets, a lower clinker replacement factor was used: about 65% clinker in the LC³-65 mixes. In addition, the 2:1 ratio between calcined clay and limestone was changed to 1:1 on some mixes. This can be also considered as a 2:1 mix, but blending down the clay using limestone. For some specific runs, model clays were prepared, using a mixture of 95% pure metakaolin from North America and quartz powder. The purpose of these designs is to get rid of the secondary phases present in the natural clays. All the mix designs are summarized in the Tables 2.4, 2.5 and 2.6. The rheology of all the pastes was adjusted using PCE-based superplasticizer from *Mapei* to obtain a binder that was easily cast into the various moulds. The usual W/B used was 0.4, with some supplementary mixes with a different water content to adjust the W/S.

Table 2.4 regroups the mixes based on the LC³-50 design and using only clays from natural origin. Table 2.5 contains the mixes based on the LC³-65 design and Table 2.6 summarizes all the mixes model clays. Plain cement references are present with the series using natural clays. Two kinds of references were used: with a similar water to binder ratio by mass or by volume. Traditionally, blended cements are compared to plain cement using the same W/B by mass. Most of time, the specific gravity of the SCM is less than that of clinker, resulting in a different volume ratio between solid and liquid when comparing mixes prepared by mass. This effect is even more emphasized with high replacement fractions, such as in LC³-50.

Table 2.4 – Detailed mix designs for the plain cement LC³-50. The main variable is the calcined kaolinite content of the clay.

Label	Cement	CC	MK in CC	Total MK content	CC:LS	W/B	W/S	Initial porosity
PC 0.4	100%	0%	-	-	-	0.4	1.32	56.7%
PC 0.37	100%	0%	-	-	-	0.37	1.22	54.8%
PC 0.357	100%	0%	-	-	-	0.357	1.18	53.9%
15%	54%	30%	15%	4.5%	2:1	0.4	1.18	53.9%
25%	54%	30%	25%	7.5%	2:1	0.4	1.18	53.9%
45% 2:1	54%	30%	45%	13.5%	2:1	0.4	1.18	53.9%
45% 1:1	54%	22%	45%	9.9%	1:1	0.4	1.19	54.2%
45% 0.45	54%	30%	45%	13.5%	2:1	0.45	1.32	57.1%
50%	54%	30%	50%	15.0%	2:1	0.4	1.18	53.9%
60%	54%	30%	60%	18.0%	2:1	0.4	1.18	53.9%

2.2. Microstructure characterization

Table 2.5 – Detailed mix designs for the LC³-65 group.

Label	Cement	CC	MK in CC	Total MK content	CC:LS	W/B	W/S	Initial porosity
LC3-65 2:1	70%	19%	45%	8.6%	2:1	0.4	1.22	54.9%
LC3-65 1:1	70%	15%	45%	6.8%	1:1	0.4	1.23	55.1%

Table 2.6 – Detailed mix designs for the model clays group, based on a LC³-50 design and using a mixture of metakaolin (MK) and quartz (QZ) to emulate calcined clays.

Label	Cement	MK	QZ	CC:LS	W/B	W/S	Initial porosity
MQ40	54%	12%	17%	2:1	0.4	1.17	53.7%
MQ45	54%	14%	15%	2:1	0.4	1.16	53.6%
MQ60	54%	19%	11%	2:1	0.4	1.15	53.3%
MQ80	54%	25%	5%	2:1	0.4	1.14	52.9%
MQ95	54%	29%	0%	2:1	0.4	1.13	52.7%

2.2 Microstructure characterization

Both creep and shrinkage are heavily related to the microstructure, through phase assemblage (*i.e.* the volume amount of each phase) and physical parameters, such as the saturation degree of the porosity. Most of these values are not directly accessible through a single experimental technique and need a combination of many.

2.2.1 Scanning electron microscopy and energy dispersive spectroscopy

A necessary step to obtain an accurate phase assemblage of the binders is to get the average atomic ratios in the C–S–H. This is obtained through a EDS multipoint analysis of a polished section of cement paste. Hardened paste samples were cut at a given age into slices of about 3 mm in thickness and put into a large amount of isopropanol to stop the hydration through solvent exchange [9]. The alcohol is changed once after 24h to 48h. A week later, the sample is placed in a desiccator for at least a couple of days, before being embedded into epoxy resin (*Epo-tek 301*). After hardening of the resin, the surface close to the sample is gently polished using fine sand paper (1200 grade) and isopropanol or deodorised petrol to slightly uncover the boundary of the sample. Further polishing is carried out with an automatic polishing machine, using petrol and diamond particle spray (*EP-spray*) of 9 μm , 3 μm and 1 μm , during 30 min, 2h and 3h respectively, with a force around 20-25 N. Finally, a 15 nm carbon coating is applied to avoid charging under the microscope. Three pieces of cement paste per mix were generally prepared at each time step.

The EDS analysis is carried out using a FEI Quanta 200 SEM, with an accelerating voltage of 15 kV, a working distance of 12.5 mm, and a spot size adjusted to get a current of

Chapter 2. Materials and methods

approximately 0.8 nA. The EDS analyser was a AXS Microanalysis XFlash 4030 SDD detector. Acquisition was followed by a quantification using *Esprit Quantax* software and PhiRhoZ matrix correction. EDS analysis points were either manually placed on the inner C-S-H (or inner product) in at least 20 zones of the sample at high magnification or using a grid of points at lower magnification. In both cases, average C-S-H composition was determined using a graphical method (Al/Ca *vs.* Si/Ca plot, see Figure 2.1) based on the intersection of the intermixes lines. Any EDS point is very likely to be a mixture of C-S-H and other hydrated or anhydrous phases, as the interaction volume of an EDS point is of the order of microns [8]. Pure mineral phases appear as fixed points on the atomic ratios plot, therefore, many EDS points will lie between some known phases and the investigated C-S-H. The mean C-S-H composition should then be the one that can produce all the measured intermixes. The presence of SCM adds some more fixed points, that can appear as asymptotes (typically metakaolin and limestone), depending on the choice of the atomic ratios. Due to the data spread when using this method on blended cements, the relative error associated to the final ratios is about 10% for Si/Ca and about 25% for Al/Ca, especially for low values. Note that, as C-S-H is generally aluminium-rich in the presence of calcined clay, it should be called C-A-S-H. Table 2.7 summarizes the C-A-S-H compositions using SEM-EDS quantification, as well as the degree of reaction of metakaolin, a mass balance output requiring the C-A-S-H composition (see next subsection). As observed in [1], there is a tendency for the Al/Ca ratio to increase with the initial metakaolin content of the mix. On the other hand, the Si/Ca ratio appears to be higher in LC³-50 than in PC — an expected result from the pozzolanic reaction with Si-rich metakaolin — but without any clear trend regarding clay purity.

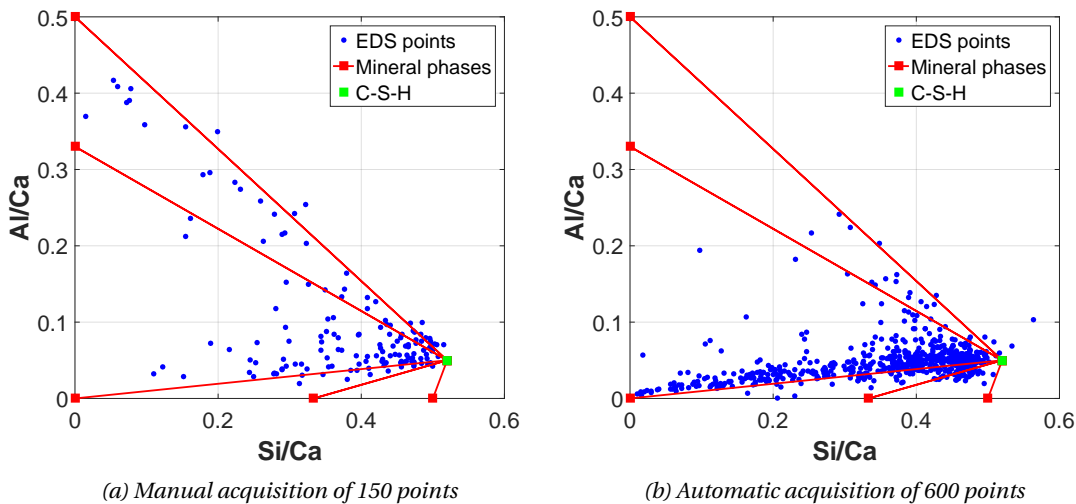


Figure 2.1 – Blue dots represent the individual EDS points and the red squares show the positions of the known mineral phases. From top left to bottom right: *Ett*, *Ms*, portlandite, alite and belite. The estimated C-A-S-H composition is the green square at Si/Ca = 0.52 and Al/Ca = 0.05.

2.2. Microstructure characterization

Table 2.7 – Average C–S–H composition of paste samples after 28 days of hydration, obtained by SEM-EDS analysis.

Label	Si/Ca	Al/Ca	MK DoH
PC 0.4	0.53	0.03	-
PC 0.37	0.52	0.03	-
PC 0.357	0.54	0.03	-
15%	0.65	0.11	100%
25%	0.63	0.10	93%
45% 2:1	0.65	0.13	64%
45% 1:1	0.66	0.10	82%
45% 0.5	0.67	0.13	66%
50%	0.67	0.13	60%
60%	0.67	0.14	50%
LC3-65 2:1	0.63	0.12	88%
LC3-65 1:1	0.62	0.09	92%
MQ45	0.65	0.13	57%
MQ95	0.70	0.21	45%
W-PC 0.4	0.54	0.04	-
W-PC 0.357	0.52	0.05	-
W-MQ40	0.68	0.12	79%
W-MQ60	0.68	0.17	62%
W-MQ80	0.71	0.21	54%

2.2.2 X-Ray diffraction, Rietveld quantification and mass balance

X-Ray diffraction or XRD is a routinely used technique in cement research and industry to assess the quality and constancy of a clinker over time. It is also a very useful method to monitor the degree of hydration of a paste and get the phase assemblage. Slices of paste were cut from hydrating samples and scanned using an X'Pert PANalytical diffractometer. The machine is configured on Bragg-Brentano mode, using Cu-K α radiation operated at 45 kV and 20 mA. Samples were scanned from 5 to 70 $^{\circ}2\theta$ in 15 min with a X'Celerator detector. External calibration using a rutile standard was carried out periodically. At each analysed epoch, two slices were cut from the sample and scanned consecutively. A Rietveld quantification method is used to quantify all the crystalline phases, followed by a mass balance calculation to obtain the amount of C-S-H and unreacted metakaolin.

A calculation method was developed by Avet [1] to get a reasonable estimation of both the C-A-S-H amount and the degree of reaction of metakaolin in LC³ binders. It is based on the mass balance calculation methods from the *Cement Chemistry* hand book [11] and uses the average C-S-H composition from SEM-EDS analysis as an extra constraint to the mass balance calculation. In short, C-S-H composition being now known, the amount of reacted metakaolin has to be adjusted so that the available ions from its dissolution, plus those from clinker yield the correct amount of hydrates, matching the XRD data. It is necessary to make a number of hypotheses to carry out the mass balance calculation: a) all gypsum is assumed to react, b) sulfate not present in ettringite (by XRD) is assumed to form monosulfoaluminate, c) when limestone is present (such as in LC³), mono- and hemicarboaluminates are formed instead of monosulfoaluminate, d) C-S-H has a constant ratio H₂O/(Si+Ca) of 4 (this includes gel water). This method requires both XRD-Rietveld and SEM-EDS data to characterize a system at given age. This can be a lengthy process, but the C-S-H composition can be interpolated if not available at some intermediate time steps. The global error of the XRD-Rietveld method is of the order of 5 to 10% per phase. That combined to the SEM-EDS accuracy yields about 10% of relative error for each phase out of the mass balance and the degrees of reaction. Mass balance is eventually converted to volume balance using the density of each phase, from [3] or GEMs database.

Table 2.8 contains the volume balance for all studied mixes at 28 days. The main features to notice are the increasing amount of carboaluminates when increasing the grade of the clay (as reported in [1]) and the smaller amount of C-S-H present in LC³ binders compared to plain cements. Figure 2.2 shows a graphical representation of volume balance over time for a LC³-50 binder.

2.2. Microstructure characterization

Table 2.8 – Summary the results of the mass balance calculation, converted into absolute volume in mL for an initial 100 g of binder. This is the main input of the finite element modelling (see Chapter 3).

Label	C ₃ S	C ₂ S	C ₃ A	C ₄ AF	MK	LS	Clay	SiO ₂	
PC 0.4	3.75	1.31	0.79	1.75	0.00	0.00	0.00	0.00	
PC 0.37	3.85	1.86	0.78	1.78	0.00	0.00	0.00	0.00	
PC 0.357	4.23	1.84	0.81	1.84	0.00	0.00	0.00	0.00	
15%	0.83	0.43	0.29	0.65	1.20	5.42	6.54	3.27	
25%	1.40	0.98	0.49	0.83	0.45	5.28	4.62	3.98	
45% 2:1	1.50	0.91	0.38	0.82	2.10	5.09	5.55	0.87	
45% 1:1	1.08	0.47	0.46	0.68	0.73	6.51	4.15	0.68	
45% 0.45	0.52	0.63	0.51	0.50	2.11	5.03	4.56	1.39	
50%	1.59	0.80	0.49	1.03	2.57	4.59	5.63	0.23	
60%	1.35	0.91	0.37	0.83	4.87	5.02	3.53	0.00	
LC3-65 2:1	1.90	1.30	0.52	1.03	0.20	3.37	4.22	0.00	
LC3-65 1:1	1.89	1.06	0.56	1.03	0.06	5.47	3.21	0.00	
MQ45	1.75	0.72	0.55	0.90	2.56	5.60	0.00	6.35	
MQ95	2.17	0.84	0.35	1.07	7.02	5.13	0.56	0.00	
W-PC 0.4	0.76	5.53	0.08	0.00	0.00	0.00	0.00	0.00	
W-PC 0.357	1.42	6.03	0.08	0.00	0.00	0.00	0.00	0.00	
W-MQ40	0.51	3.69	0.10	0.00	0.78	5.47	0.00	6.82	
W-MQ60	0.68	3.83	0.11	0.00	2.39	5.50	0.00	4.49	
W-MQ80	0.82	3.84	0.13	0.00	4.12	5.69	0.00	1.92	
Label	CH	Ett	Ms	Mc	Hc	Ht	Hg	C-A-S-H	Water
PC 0.4	9.86	6.40	3.80	0.00	0.00	0.44	1.26	30.64	7.00
PC 0.37	9.61	6.87	3.18	0.00	0.00	0.43	1.23	29.48	5.06
PC 0.357	9.96	7.08	2.90	0.00	0.00	0.42	1.16	28.41	4.01
15%	5.19	6.30	0.00	2.36	1.04	0.64	1.47	19.18	14.73
25%	2.16	6.06	0.00	3.16	1.74	0.37	0.81	22.93	14.04
45% 2:1	1.99	6.28	0.00	3.70	2.18	0.25	0.82	24.86	11.70
45% 1:1	2.83	6.76	0.00	3.26	2.06	0.27	0.99	27.14	9.87
45% 0.45	2.51	6.97	0.00	3.17	3.66	0.85	1.18	27.16	17.73
50%	1.75	6.69	0.00	3.03	2.23	0.36	0.58	25.09	11.73
60%	1.57	6.49	0.00	3.37	2.43	0.37	0.80	25.38	11.21
LC3-65 2:1	4.10	6.00	0.00	3.80	4.17	0.32	1.11	29.76	6.85
LC3-65 1:1	4.80	6.03	0.00	4.66	5.11	0.33	1.11	28.43	8.10
MQ45	2.08	6.81	0.00	2.02	2.07	0.65	0.73	24.53	12.63
MQ95	1.28	7.52	0.00	1.00	2.19	0.53	0.55	26.90	11.21
W-PC 0.4	11.46	6.00	0.00	0.00	0.00	0.70	0.00	39.10	4.26
W-PC 0.357	10.35	6.00	0.00	0.00	0.00	0.66	0.00	37.73	1.85
W-MQ40	1.68	6.09	0.00	2.64	1.97	0.35	0.00	28.50	10.69
W-MQ60	1.02	5.80	0.00	2.26	1.83	0.34	0.00	30.68	10.12
W-MQ80	0.71	6.12	0.00	1.96	1.74	0.34	0.00	32.15	8.93

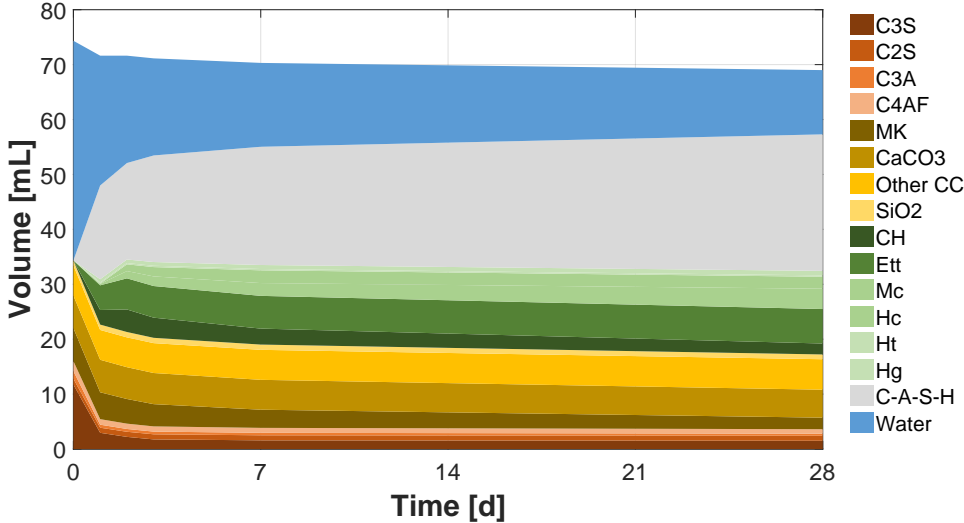


Figure 2.2 – This figure represents the result of the mass balance calculation, converted into volume, starting with 100 g of binder and 40 g of water. The fluctuations during the first days reflect the overall uncertainty of the calculation. Data points were taken at 1, 2, 3, 7, and 28 days of hydration.

2.2.3 Mercury intrusion porosimetry

Mercury intrusion porosimetry is a widespread but controversial characterization technique for cementitious materials [4], [10]. Interpretation of the results depends heavily on the underlying hypotheses, such as wetting angle and pore shape, but was recently proven to be useful for both qualitative and quantitative outputs, when correctly interpreted [7]. Nevertheless, MIP can be used to monitor and compare total porosity and the overall refinement of the pore network among different samples over time. In this study, the porosimeters used were a Pascal 140 and a Pascal 440 from *Porotec*. Interpretation was made using the Washburn model for cylindrical pores, with a contact angle of 120° . Hydration of the samples was stopped using solvent exchange (see 2.2.1). Prior to porosity measurement, samples were cut into small parts and 6 to 10 pieces, weighing 1 to 1.5 g in total, were placed in the porosimeter. Figure 2.3 shows the porosimetry results for a set of pastes after 28 days of hydration. As observed in previous studies, the total amount of porosity is very similar between plain cement and LC^3 . This is expected, as LC^3 forms less hydrates because of the lower amount of reactive material, even if the initial W/S is lower. What varies though, is the size distribution of that porosity. This is represented by the pore radius at which the porosity sharply increases. This pore size is known as the *threshold radius* or the *critical pore entry radius*. One of the main effects of calcined clays and SCM in general is a decrease of this quantity. As reported in [1], given enough time, LC^3 blends show an important narrowing of the pore entry radius, even with low metakaolin content.

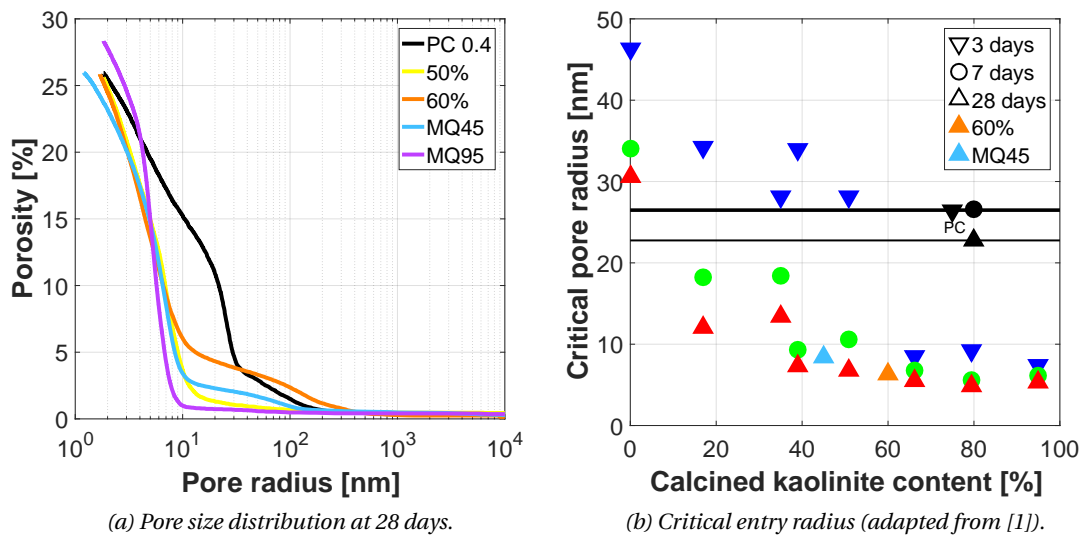


Figure 2.3 – a) Pore size distribution at 28 days for a plain cement and some LC^3 . Total porosity is less affected by the presence of SCM than the limit for pore refinement. b) Previous studies showed that the critical pore entry radius gets highly refined in LC^3 when using clays with at least 40% of calcined kaolinite. Black horizontal lines represent the values for PC.

2.2.4 Saturation degree of the porosity

Saturation degree is defined as the ratio of total evaporable water (down to the C–S–H interlayer water) to total pore volume. This quantity can be obtained through a combination of techniques, such as chemical shrinkage measurement, MIP and ¹H-NMR, or thanks to mass balance. The latter method was used in this research, as mass balance calculation was carried out on all systems. Total porosity from mass balance is in good agreement with the results from MIP and the quantity of hydrates are comparable to the output of thermodynamic modelling (*GEMs*, [6]), therefore this approach should provide a satisfactory estimation of the saturation level.

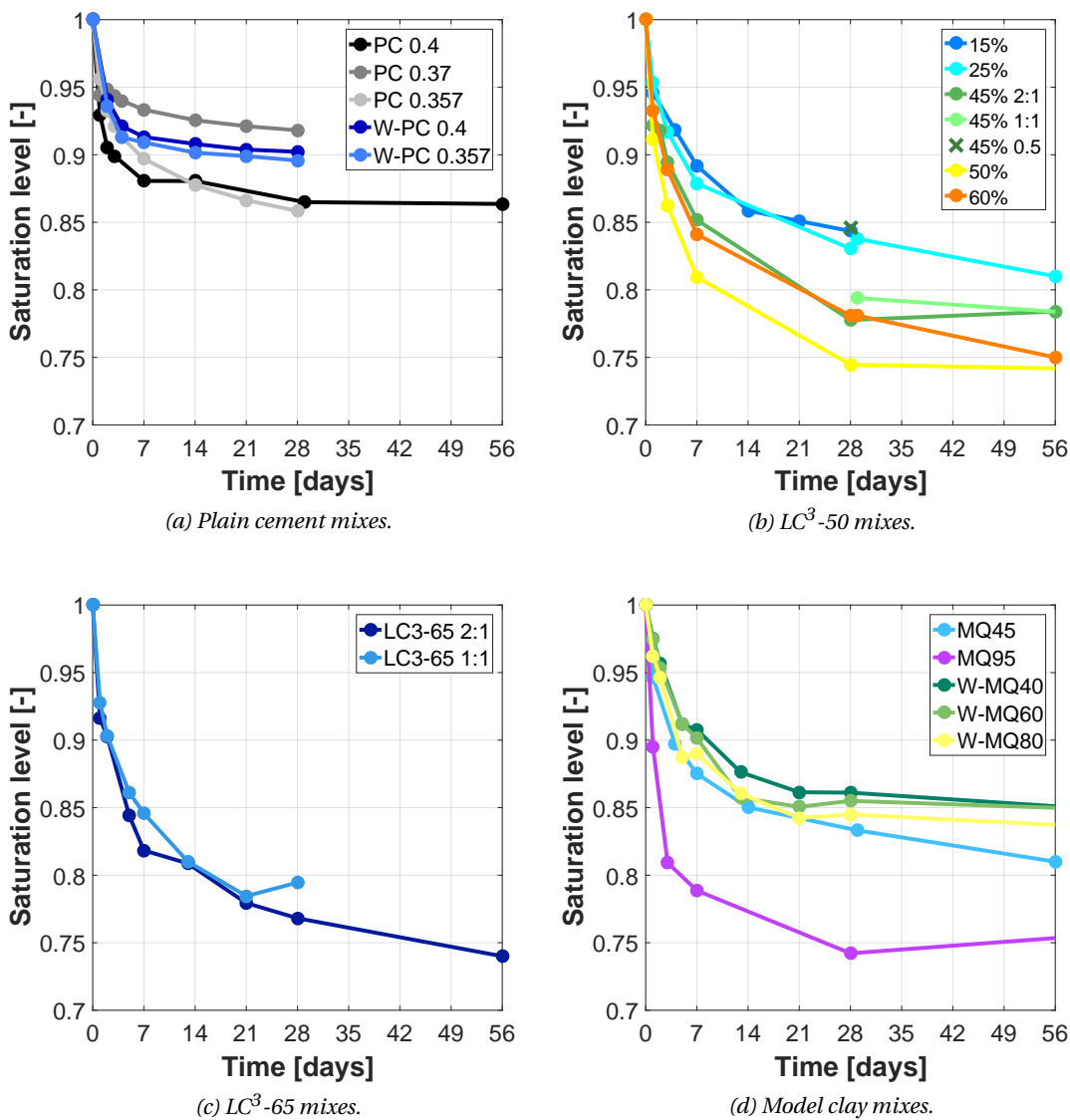


Figure 2.4 – Saturation level by mass balance calculation for the studied mixes.

2.2. Microstructure characterization

Capillary water and chemical shrinkage are direct outputs from mass balance, and gel and interlayer water have to be calculated from the C–S–H amount. The C–S–H gel, from the mass balance output, is considered to have a $H_2O/(Si+Ca)$ ratio fixed at 4 and this ratio is set at 1.8 for the structural water. The difference is the evaporable water from C–S–H. Figure 2.4 summarizes the saturation degree of the studied mixes. Results indicate that LC³ materials have a lower saturation level than plain cement mixes. This is explained by the higher amount of C–S–H in the cement mixes, containing larger amounts of evaporable water and contributing to a higher saturation.

2.3 Mechanical properties

Basic mechanical properties, such as compressive strength and Young's modulus are necessary data for the compressive creep set-up and for the interpretation of the modelling results.

2.3.1 Compressive strength

Compressive strength tests were carried out on paste samples prior to their loading on the creep frames after 28 days of sealed cure, see 2.9. The cubes were cut out from the prisms cast for the creep tests (more details in Chapter 3), ending with a side length of 25 mm. Loading speed is about 2.4 MPa/s. Each value is the average of 6 measurements.

Table 2.9 – This tables summarizes all the compressive strengths measurements carried out at 28 days

<i>Label</i>	<i>Strength [MPa]</i>	<i>St. dev. (S)</i>
PC 0.4	72.73	3.21
PC 0.37	78.79	3.70
PC 0.357	82.64	4.31
15%	52.19	1.35
25%	67.30	3.21
45%	71.53	2.88
45% 1:1	68.27	1.69
45% 0.5	48.46	3.69
50%	75.47	7.78
60%	78.56	4.61
LC3-65 2:1	71.49	4.55
MQ45	81.87	1.51
MQ95	76.91	3.76
N4-PC 0.4	68.04	4.11
N4-45%	76.77	4.89
N4-95%	73.90	6.37

2.3.2 Young's modulus

Young's modulus is used as an input for the shrinkage and creep models. Two main ways to measure this property were used in this study. The continuous method allows to monitor the evolution of Young's modulus minutes after casting, whereas the discrete methods require hardened samples.

Continuous method

The Elastic Modulus Measurement through Ambient Response Method (EMM-ARM) [2] was used to carry out the continuous measurements of Young's modulus. Paste was prepared and cast into 550 mm long PMMA tubes of 20 mm of outer diameter and 16 mm of inner diameter. The first end of the tube was previously sealed with a piece of rigid plastic sheet and glue. The second end was sealed after casting using tape. The tube is then placed in a horizontal position with a metal clamp, creating a cantilever system with a span of 450 mm. An accelerometer of known mass is then fixed at the far end of the cantilever. A pair of fans was placed next to the set-up to provide an external source of excitation as white noise. A computer then logs the outputs of the accelerometer and, knowing the rigidity of the polymer tube alone, is able to calculate the Young's modulus of the sample.

Discrete methods

Discrete methods refer to measurements of the strain of a sample under a known load, at a given point in time. This can be either done using a press, as in NF EN 12390-13, or when adding or removing load from the creep frames. A small series of mixes was tested using the standard method and all the samples undergoing creep tests had their Young's modulus systematically estimated at the beginning and the end of the test. In that case, the total load was placed and removed several times over a short period in order to get more readings, but also to ensure that the top and bottom aluminium coatings were correctly flattened. Figure 2.5 presents the evolution of Young's modulus for a series of samples. It shows that, as already stated in [5], all the methods give similar results. Table 2.10 summarizes all the elasticity measurements carried out at the beginning and the end of the creep tests. It can be noticed that most of the samples still gain about 10% rigidity during the second month of hydration.

Chapter 2. Materials and methods

Table 2.10 – This table summarizes the measurements of Young's modulus carried out before and after the creep tests. Each value is the average of 1 to 3 loading-unloading cycles.

Label	28 days		56 days	
	Young's modulus [GPa]	St. dev. (S)	Young's modulus [GPa]	St. dev. (S)
PC 0.4	16.5	0.5	20.1	0.3
PC 0.357	19.3	0.2	20.9	0.1
PC 0.37	18.1	0.3	20.6	0.2
15%	13.1	0.6	16.6	0.4
25%	15.4	0.9	17.7	0.3
45% 2:1	14.6	0.3	16.5	0.1
45% 1:1	14.9	0.1	17.1	0.0
45% 0.5	11.7	0.3	13.3	0.6
50%	13.9	0.1	16.9	0.0
60%	14.5	0.1	17.3	0.6
N4-45%	11.8	0.5	13.4	0.3
LC3-65	15.5	0.3	17.9	0.2
LC3-65 1:1	15.9	0.3	18.7	0.1
MQ45	15.1	0.7	18.4	0.3
MQ95	14.6	0.2	16.2	1.4
N4-PC 0.4	12.8	0.4	17.6	0.2
W-MQ95	11.1	1.2	13.8	0.6
W-PC 0.4	17.5	0.4	19.3	0.3
W-PC 0.357	18.3	0.3	21.4	0.1
W-MQ40	15.9	0.7	17.8	1.1
W-MQ60	15.4	2.1	21.5	2.0
W-MQ80	13.8	0.6	17.1	0.9

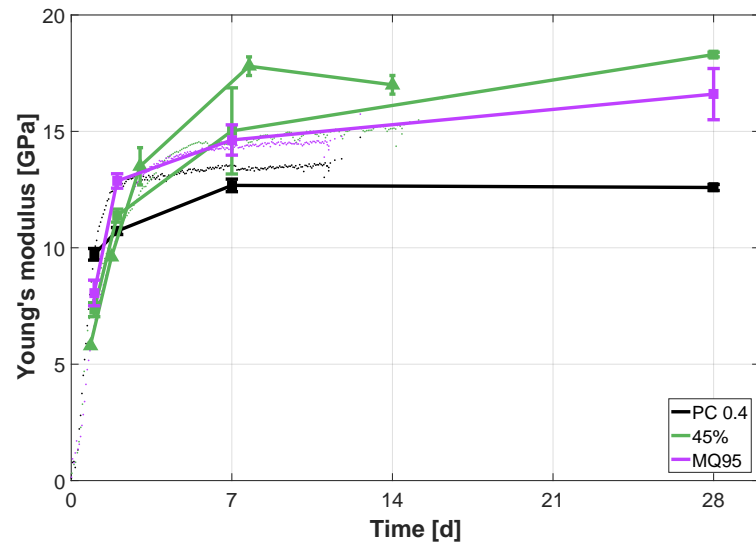


Figure 2.5 – Evolution of Young's modulus over the first month of hydration. The dots represent the results of the EMM-ARM set-up, the squares the quasi-static method from NF EN 12390-13 and the triangles are from loading-unloading creep samples.

2.4 References

- [1] François Henri Avet. “Investigation of the grade of calcined clays used as clinker substitute in Limestone Calcined Clay Cement (LC3)” (2017), p. 169.
- [2] Miguel Azenha et al. “Measurement of concrete E-modulus evolution since casting: A novel method based on ambient vibration”. *Cement and Concrete Research* 40.7 (July 2010), pp. 1096–1105.
- [3] M. Balonis and F. P. Glasser. “The density of cement phases”. *Cement and Concrete Research* 39.9 (Sept. 2009), pp. 733–739.
- [4] Sidney Diamond. “Mercury porosimetry: An inappropriate method for the measurement of pore size distributions in cement-based materials”. *Cement and Concrete Research* 30.10 (Oct. 2000), pp. 1517–1525.
- [5] Zhangli Hu. “Prediction of autogenous shrinkage in fly ash blended cement systems” (2017), p. 213.
- [6] Barbara Lothenbach and Frank Winnefeld. “Thermodynamic modelling of the hydration of Portland cement”. *Cement and Concrete Research* 36.2 (Feb. 2006), pp. 209–226.
- [7] A. C. A. Muller and K. L. Scrivener. “A reassessment of mercury intrusion porosimetry by comparison with ¹H NMR relaxometry”. *Cement and Concrete Research* 100 (Oct. 2017), pp. 350–360.
- [8] J. E. Rossen and K. L. Scrivener. “Optimization of SEM-EDS to determine the C–A–S–H composition in matured cement paste samples”. *Materials Characterization* 123 (Jan. 2017), pp. 294–306.
- [9] Karen Scrivener, Ruben Snellings, and Barbara Lothenbach. *A practical guide to microstructural analysis of cementitious materials*. Crc Press, 2016.
- [10] Dexiang Shi and Douglas N. Winslow. “Contact angle and damage during mercury intrusion into cement paste”. *Cement and Concrete Research* 15.4 (July 1985), pp. 645–654.
- [11] Harry FW Taylor. *Cement chemistry*. Thomas Telford, 1997.

3 Basic creep on mature paste samples

In this chapter, the theoretical background required to understand and interpret the experimental outputs will be presented. A description of the experimental set-up and obtained results will follow. The next part concerns result processing and links with the microstructure. Finally, a further interpretation of the results using two modelling approaches is presented.

Part of this Chapter was submitted to *Cement and Concrete Research* as *Intrinsic viscoelasticity of C-S-H assessed from basic creep of cement pastes*, by Z. Hu*, A. Hilaire, J. Ston, M. Wyrzykowski, P. Lura, K. Scrivener, and to

Theoretical and Applied Fracture Mechanics as *Basic creep of Limestone - Calcined Clay Cements: an experimental and numerical approach*, by J. Ston and K. Scrivener[†]

Corresponding author: *zhangli.hu@empa.ch, [†]karen.scrivener@epfl.ch

Contents

3.1 Literature review	29
3.1.1 Creep mechanisms in cement	29
3.1.2 The role of supplementary cementitious materials	32
3.1.3 Creep modelling	35
3.1.4 Basic creep and autogenous shrinkage	37
3.2 Experimental methods	38
3.2.1 Sample preparation	38
3.2.2 Compressive creep frames	38
3.2.3 Results processing	39
3.2.4 Basic creep kinetics	39
3.3 Experimental results	43
3.3.1 Influence of cement type	43
3.3.2 LC ³ with natural calcined clays	45

Chapter 3. Basic creep on mature paste samples

3.3.3	Influence of initial water content	48
3.3.4	Model clays	50
3.3.5	Fitting results	52
3.3.6	Creep rate and microstructure	54
3.3.7	Summary of the results	56
3.4	Modelling	57
3.4.1	Finite Elements Modelling	57
3.4.2	Rheological modelling	65
3.5	Conclusions	69
3.6	References	72

3.1 Literature review

Many classes of materials exhibit time-dependent strains when subjected to a constant load. Cement and concrete are no exception. Creep in concrete — and counterpart relaxation — can be a useful phenomenon for relieving stresses from restrained shrinkage, or a detrimental one when dealing with prestressed structures. Hence, some understanding of the visco-elastic behaviour of cement is necessary to correctly engineer large structures, such as bridges.

Basic creep is defined as the viscous deformation of a concrete specimen without any exchange of moisture with the environment or change in temperature. It is usually measured by applying a uniaxial load on a sealed sample and measuring its deformation over time along that axis. By definition, the measured strain is a combination of basic creep from the static load and autogenous shrinkage from the hydration of the binder. The usual way to obtain pure basic creep is to compare the strains of a loaded sample and an unloaded one [47].

The interest of studying basic creep in particular, besides the more controllable laboratory conditions, is that it is present in any structural part. Viscous strain rates in cementitious materials, be it in sealed or drying conditions, do not seem to stabilize over time. This implies that basic creep rate, albeit continuously decreasing, would never reach a halt. Within this study, the superposition principle was applied to process the results, subtracting the autogenous shrinkage strain to the total strain measured on the creep frames to obtain pure basic creep strain (more details in section 3.1.4).

3.1.1 Creep mechanisms in cement

Contrary to metals or polymers, no consensus has yet been reached in cement research to explain the exact creep mechanisms. Nevertheless, experimental evidence points out that among all the anhydrous or hydrated phases present in cementitious materials, C–S–H mainly shows a pronounced viscoelastic behaviour. In addition, water probably plays a role in viscoelasticity, possibly varying with its location (capillary, gel or interlayer water) and the bonding strength with the surrounding surfaces. Several theories exist, most of them being based on hypothetical concepts of C–S–H structure.

C–S–H is a multiscale organized material. At the atomic scale, C–S–H is a defective tobermorite-like structure. Tobermorite $\text{Ca}_{4.5}\text{Si}_6\text{O}_{16}(\text{OH}) \cdot 5\text{H}_2\text{O}$ is a layered mineral made of Ca–O layer with chains of SiO_4 tetrahedra on either side. These sandwich elements are separated one from another by a layer of water and Ca^+ ions. The SiO_4 tetrahedra are organised in chains of three units (called *dreiketten*), but in C–S–H, this silicate chain length can vary from 2 to 5. Moreover, OH groups can bind to the Si and Ca and vacancies can appear at the silicates bridging sites. In the presence of aluminium, AlO_4 tetrahedrons can act as bridging elements between silicate chains. These C–S–H sheets are separated by water pores of the order of 10 nm called gel pores. At the micron scale, C–S–H in cement is organised in needles

or foils when growing in the free space around cement grains (outer product) or in a more homogeneous gel in the inner product. The differences between the many representations of C-S-H are how the structures of varying size are arranged.

The role of water

Water in cement paste is generally separated into different populations, depending on its confinement and location in the microstructure. Water sometimes occupies the pores of the microstructure, so the nomenclature for water also suits pores. Ignoring air voids or entrained air, the largest family of pores is known as the capillary pores, hosting capillary water. Capillary water can transfer loads to the solid skeleton of the microstructure and diffuse to regions with lower pressure when stress is applied. Because of the very low flows involved, this is not believed to be a main contribution to creep strain [9], [65]. Moreover, experiments carried out on samples whose evaporable water was removed still exhibited significant creep [54]. In addition, movement of capillary water is not sufficient to explain the irreversible part of creep strain. The presence of capillary porosity *per se* could however have an effect on the macroscopic compliance of the specimen.

Gel water is the main actor in many theories trying to explain creep. Gel pores are nanometric cavities in-between regions of short-range ordered C-S-H, where surface effects dominate water thermodynamics. Their dimensions are quite specific and seem not to depend on the chemistry of C-S-H [3]. Gel water is not chemically bound to C-S-H, but contributes to its structural stability. It can evaporate with drying or be removed with solvent exchange [3]. The most notable theories involving gel water are the microprestress-solidification theory from Bažant, thermal activation energy theory from Wittmann and various structural rearrangement theories from Thomas, Jennings or Li. It is worth making a short summary of these points of view to get their common features.

The microprestress-solidification theory [8], [31] is an extension of the seepage theory [44], proposed by Powers and based on the Powers-Brownyard representation of C-S-H [52], see Figure 3.1. It states that the time dependent deformation comes from the gradual diffusion of water molecules from high stress regions to lower stress ones. The highly stressed zones are likely to be the regions of hindered adsorption, where solid surfaces are close enough so that fewer layers of adsorbed water molecules can be present compared to what thermodynamic equilibrium would allow. This theory explains the irreversible part of creep by the bonding of the aforementioned solid surfaces when water is pushed out. Thermal activation energy theory [63], similarly to viscous shear theory [48], considers gel water as a lubricator for the sliding of C-S-H solid particles towards a more stable configuration. Contrarily to the microprestress-solidification theory, water molecules do not migrate in the microstructure, even though both theories are based on the same microstructural model.

Following the elaboration of their colloidal models (CM-I and CM-II) representing C-S-H, Jennings and his co-workers proposed creep theories based on the rearrangement of C-S-H

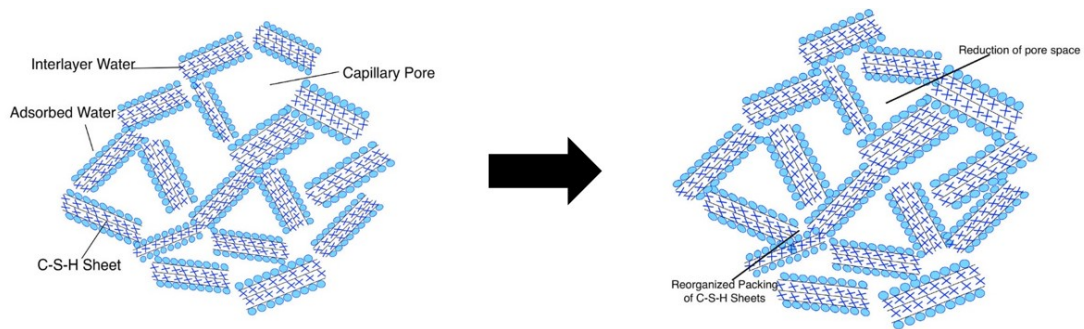


Figure 3.1 – This figure adapted from [65] depicts the C–S–H model from Power and Brownyard (P-B model). C–S–H consists of ordered solid particles. Movement of water away from confined regions causes a rearrangement of the solid particles. The left part of the figure show a pristine region of C–S–H, whereas the right part has undergone some creep.

globules — the "building blocks" of their model [55], see Figure 3.2. Although their theories lack a precise explanation of the rearrangement mechanisms of the globules (in CM-I) or the tobermorite-like layered sheets (in CM-II), or a precise description of the role of the water at different levels, their ideas are claimed to be supported by nano-indentation measurement on C–S–H [57]. It appears that the results from that study agree with a rearrangement of packed particles, bearing many similarities with soil mechanics. For instance, Vandamme and co-workers reported a similar behaviour between creep of C–S–H at the micrometer scale and clayey soils at different packing densities [58]. To conclude, a study from Pachon-Rodriguez and his team [41] indicated that a rearrangement of globules could be carried out through dissolution, diffusion and reprecipitation of the load bearing regions of the solids.

Lastly, interlayer water, which refers to the strongly (physically) bound water in-between the C–S–H layer, is also at the centre of a couple of theories. It is worth mentioning the crystallisation theory, based on the Feldman-Sereda representation of C–S–H [21], which states that creep results first from a movement of gel water to the interlayer space. This is

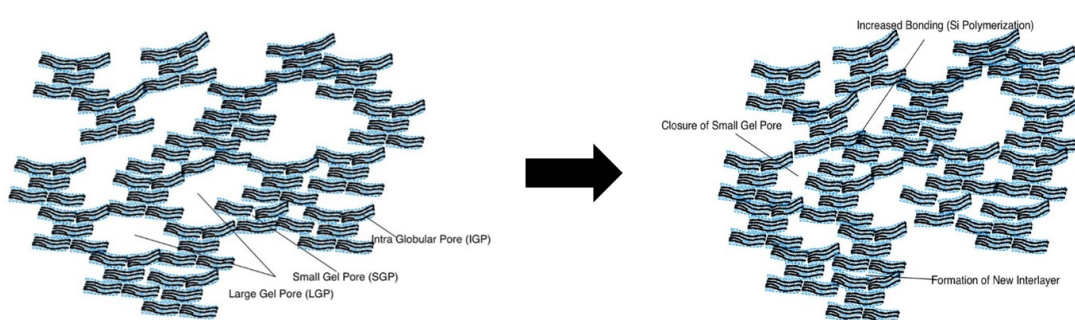


Figure 3.2 – This figure adapted from [65] depicts the CM-II model of C–S–H. The main difference with CM-I is that the globules are composed of tobermorite-like particles. The left part of the figure shows a pristine region of C–S–H, whereas the right part has undergone some creep.

Chapter 3. Basic creep on mature paste samples

followed by a crystallisation or reorganisation of the poorly arranged C–S–H layers thanks to gel water bridging to interlayer sites.

In summary, there exist many models to represent the micro- or nanostructure of C–S–H, along with theories to explain basic creep, matching the features of one model or the other. The main point where all theories agree is the necessity to explain the irreversible part of creep thanks to hardening mechanisms, for instance breaking and reformation of bonds or dissolution and reprecipitation. On the other hand, most theories fail to predict any easily measurable observables, and cannot so far be formally proven nor invalidated. Nevertheless, it appears that creep happens within a scale ranging from the alumino-silicate chains, up to nanometre-scaled regions composing the microscale of C–S–H.

3.1.2 The role of supplementary cementitious materials

There have been a few investigations on the impact of metakaolin and limestone on creep, but they yielded only some specific results. As presented in the introductory chapter, metakaolin is a very efficient, yet expensive, pozzolan. Its influence on creep of cementitious binders has only been slightly investigated. The work from Brooks and Johari [16] offers a good review of the knowledge concerning metakaolin substitution in concrete. In summary, a modest replacement of clinker with metakaolin (5 to 10%) increases compressive strength at the expense of workability, if mix design remains unchanged. Concerning delayed strains, the use of metakaolin was found to reduce both autogenous and drying shrinkage of concrete and lowers compressive creep compliance. This study did not give any precise mechanisms leading to the change in viscoelastic behaviour, but proposed a list of potential reasons, such as a refinement of the pore structure [40] or better interface between cement and aggregates, both thanks to the extra hydrates from the pozzolanic reaction and the filler effect of metakaolin.

From a chemical point of view, MK is an important source of aluminium ions. This supplementary aluminium will enrich C–S–H into C–A–S–H, while consuming portlandite. Aluminium-rich strätlingite (C_2ASH_8) will also precipitate if MK is the only replacement

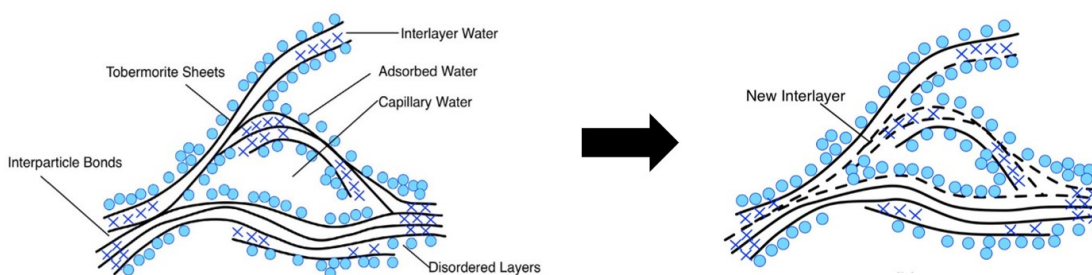


Figure 3.3 – This figure adapted from [65] depicts the C–S–H model from Feldman and Sereda or F-S model. External loads could push some of the weakly bound water, leading to a reorganization of the sheets. The left part of the figure show a pristine region of C–S–H, whereas the right part has undergone some creep.

material. Many studies reported a decrease in creep compliance when using metakaolin [16], or other SCMs, such as slag, fly ashes or glass powder [34], [23]. SCMs in general will affect the chemical composition of C–S–H [35], but none of the cited works reported a direct link between C–S–H composition and creep compliance, as the incorporation of SCMs has other very important effects on the microstructure that affect creep. According to a study carried out on mixtures of white cement and metakaolin [18], incorporation of metakaolin in the mix increases both the average alumino-silicate chain length and the Al/Si of C–S–H (see Figure 3.4). Unfortunately, they did not compare mechanical properties against the evolution of C–S–H morphology and composition. If creep happens at the scale of the alumino-silicates chains of C–S–H, this could have a potential impact on the viscous properties.

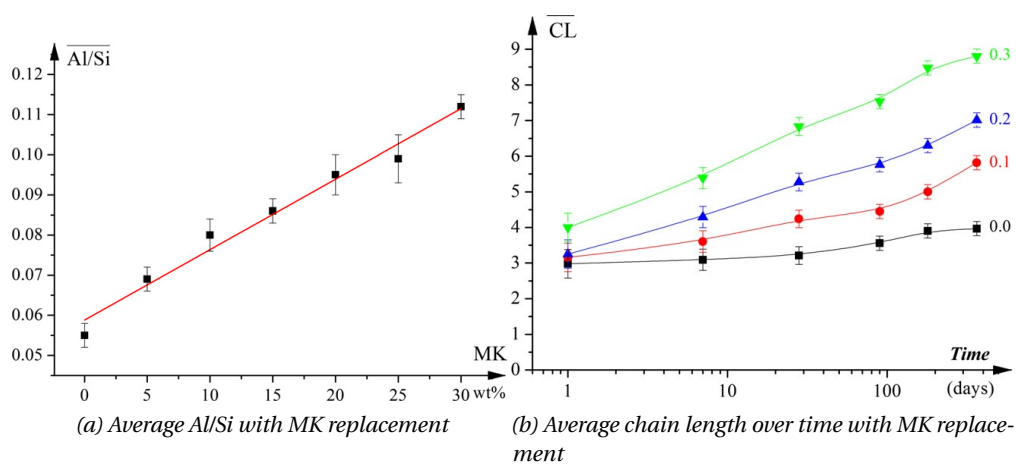


Figure 3.4 – a) Average Al/Si ratio of C–S–H in white cement blended with increasing amounts of metakaolin. b) Average alumino-silicate chain length in C–S–H for white cement blended with 0% to 30% MK. Both plots adapted from [18], where ^{29}Si and ^{27}Al MAS NMR were used as the main experimental techniques to determine the composition of C–S–H.

Limestone is mostly considered on its own as an inexpensive filler. In a binary mix, it provides extra surface for hydrate nucleation and even shows some reactivity with the aluminium present in the cement [42], [37], [36]. Little knowledge is available on the effect of limestone filler on the creep properties of concrete or cement. Wang [61] reported a decrease of the compressive creep compliance in drying conditions when replacing cement with limestone in concrete. Unfortunately, they did not examine the microstructure of the different samples, nor did run any basic creep tests. Below [13] attributed the decrease in creep compliance to a denser microstructure in his short communication about concrete using limestone powder replacement. Finally, He [24] reported a lower basic creep compliance in concrete using metakaolin and limestone as replacement materials (a mix design equivalent to LC³-70 95% 1:2 in the present thesis), see Figure 3.5.

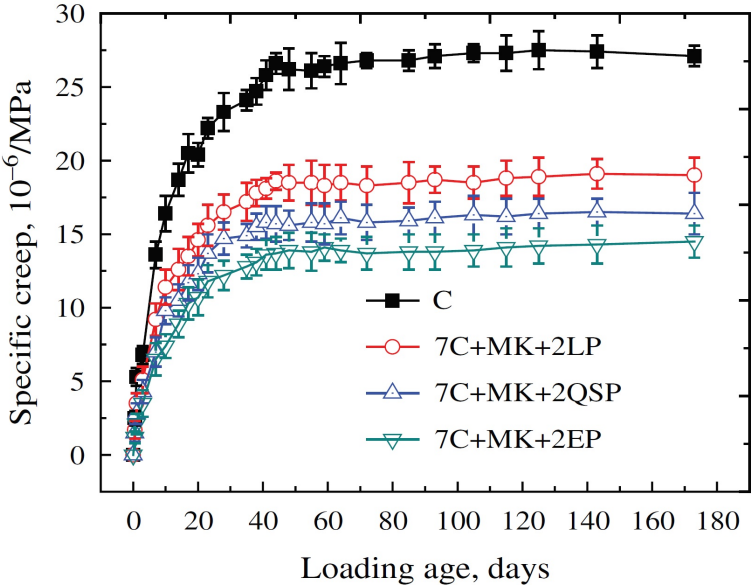


Figure 3.5 – This figure shows the results from He and co-workers [24] concerning compressive creep of concrete containing metakaolin and other SCMs. The red curve with circles corresponds to a LC^3 design.

3.1.3 Creep modelling

Modelling is a very useful tool for understanding different phenomena. In the case of creep of cement paste, two modelling scales can be identified, each with different purposes: a phenomenological approach to grasp the behaviour of the material at a macroscopic scale, and a more fundamental approach to model the mechanisms at the microstructure scale. The modelling in the present study fits the first category, but it is worth summarizing what has been achieved lately in both fields to help the interpretation of the results.

Phenomenological modelling

Phenomenological modelling is the most widespread and accessible way to model basic creep of cement or concrete structures. It approaches creep compliance thanks to a mathematical function with a limited number of parameters or using rheological models with a modest amount of units. This approach has the advantage of being able to simply calculate the predicted strain over considerable time scales. This is the reason why such approaches are used in structural codes to estimate the life expectancy of concrete structures subject to creep [39]. However, the selection of the function to fit the experimental data has evolved through time, and as more and more long term results become available.

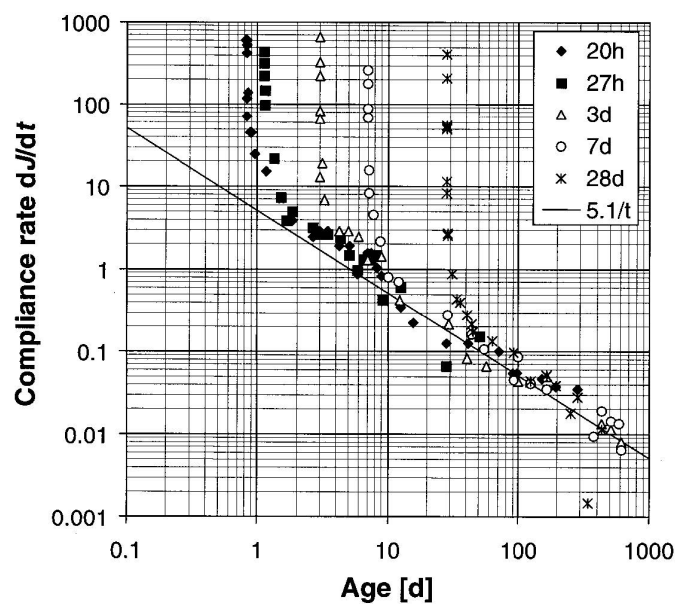


Figure 3.6 – On this plot, the compliance rate over time is reported for different loading ages on the same mix design. It appears that the long-term rate is solely dependent on the material, from [1].

The work of Bažant indicated early on that basic creep compliance could be well approximated with a power law, or a combination of such [10]. Processing longer term data led him to notice later that a logarithmic function was better adapted to model the very long-term behaviour of basic creep in concrete. In particular, if the loading period was much longer than the curing time before loading, creep compliance rate would reach a similar value for a given

mix, as depicted in Figure 3.6. Interestingly, this logarithmic trend appeared independently of the age of loading (or, more precisely, the degree of hydration of the system). This means that the final creep rate tends to a given value for a given mix, regardless of the amount of autogenous shrinkage the sample has undergone before the compressive creep load. Further improvements refined the mathematical model, notably adding more parameters to the function fitting the first time derivative of creep compliance. The motivations to do so were a better fit of the experimental data both for the short and long term, and better extrapolation, at the expense of more coefficients to be adjusted.

Other researchers reached similar conclusions [66], [56], [33], [19]: creep compliance is well approximated with a power law during the initial period, followed by a logarithmic trend for the long term. This transition period seems to be related to the scale of the experiment. It can take years or decades to reach a logarithmic regime for concrete samples, but merely seconds for cement paste under a micro/nano-indenter [57], [29].

The second way to simulate the viscoelastic response of a concrete — or many other materials for that matter — is to use rheological models. Most of these approaches use Kelvin-Voigt, Maxwell or Burgers model, alone or chained. Elaborated models link these elements and their properties to time or degree of hydration to take into account the ageing of the materials. Such viscoelastic models are able to fit and predict many experimental results, at a low computational cost. Similarly to the mathematical fitting described above, the fitting parameters do not possess a physical meaning, as the primary objective is to describe the macroscopic behaviour of the material. However, it is worth noticing that some investigation was done to find parallels between the properties of the components of the rheological models and characteristics of the microstructure or potential creep mechanisms. Notably in [50] and [51], the authors propose to match the properties of the springs and dashpots of a Kelvin-Voigt rheological model to actual micromechanical features of the microstructure, such as interface viscosity or stiffness of the composite matrix.

Microstructural modelling

The bottom-up approach concerning creep generally consists in using a homogenization scheme to go from the nano/micro-structure up to the sub-millimetre (for cement paste) or sub-centimetre scale (for mortars) as shown on Figure 3.7. Notably, Königsberger and his colleagues [32], applied a back-calculation scheme to Irfan-ul-Hassan's minute-long creep test results [29] down to the hydrates scale to show that short-term creep could be modelled using a single power law. As another example, this is also the solution proposed by Shahidi *et al.* for implementing their rheological model to higher scales [50], [51]. Microstructural modelling is not the main simulation method used in this study, but it is worth noticing that similar tools can be used either to model the macroscopic behaviour of a structure or the microscopic behaviour of the hydrated phases supposedly at the origin of creep in cementitious materials.

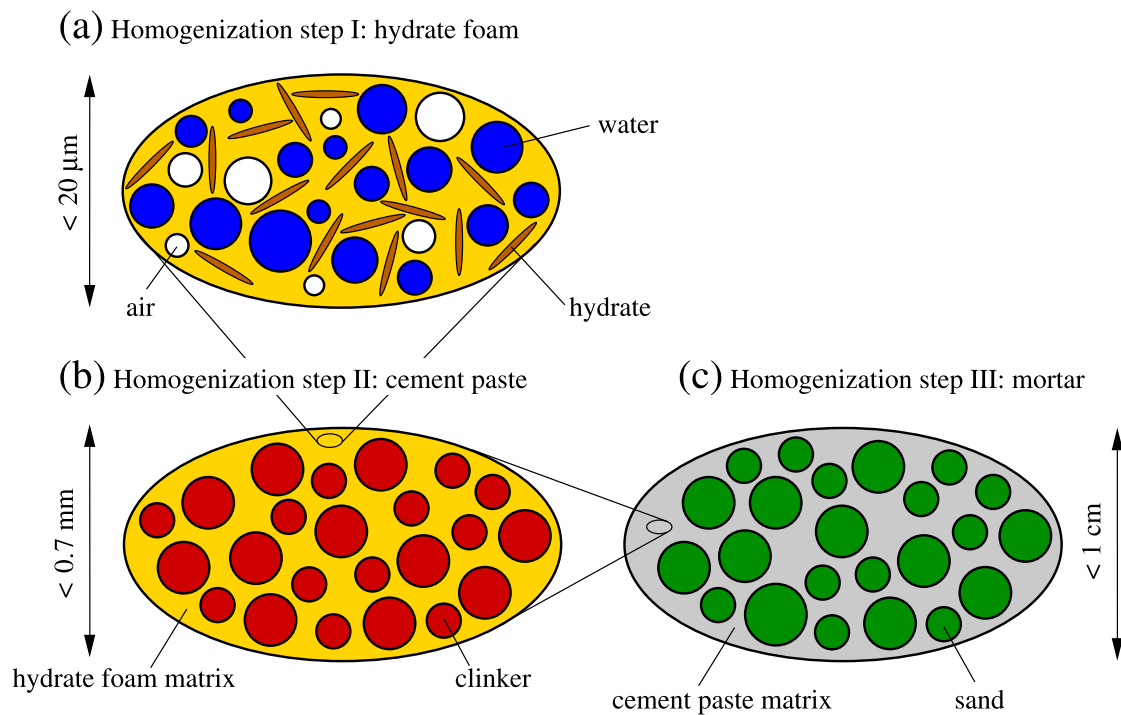


Figure 3.7 – This figure from [32] illustrates the pathway from nanoscale to macroscale mechanical modelling thanks to several homogenization steps.

3.1.4 Basic creep and autogenous shrinkage

Supposing the independence of basic creep and autogenous shrinkage is a convenient hypothesis for processing the data, as a simple subtraction allows to separate them. This hypothesis has not been formally proven so far, and its validity could be questioned, especially on creep tests starting at an early age, with hydration progressing at a considerable rate. It is based on the principle of superposition of strains in viscoelastic materials, firstly proposed by Boltzmann [15] and later applied to ageing materials by Volterra [60]. It is widely used with cementitious materials. Studies and models on large amounts of data, with some creep tests starting as early as 20h after casting and others lasting up to decades, illustrated that the stress superposition principle was valid for basic creep under up to 0.4 of the strength of the material [12], [7], [11], [20], [6], [5], [10]. This high threshold value implies that the superposition principle could also be applied for separating autogenous shrinkage and basic creep, although the former comes from a volumetric stress and the latter usually from a linear one.

3.2 Experimental methods

The purpose of the creep campaign carried out in this chapter is to obtain data to answer the following questions:

- Is C–S–H the only phase capable of creep in the LC³ binders, or are the clayey mineral bringing viscosity to the material?
- Is the different chemistry of LC³ affecting creep properties?

As mentioned in the first chapter, experiments were only carried out on paste samples, to avoid the effect of aggregates and to be able to run numerous samples. Microstructural data from the previous chapter and modelling are used to interpret the data.

3.2.1 Sample preparation

After weighing, powders and water were mixed in a vacuum mixer for 2 minutes at 450 rpm. Paste was then cast into eight 25 x 25 x 80 mm moulds. The samples were cured for 24h in a moist environment. Right after demoulding, the paste prisms were wrapped in a polyethylene film and two layers of adhesive aluminium sheet, to ensure autogenous conditions. The top and bottom square faces were covered only with a single layer of aluminium, in order to have as little material as possible between the sample and the loading plates. The samples were then left to cure at 20°C, until they reached their loading age, usually 28 days for this study. Sealed prisms were weighed right after wrapping, at the end of the cure and after the creep test. The weight loss was always very low, between 0% and 0.2%. Between 6h and 24h before the beginning of creep loading, two prisms were unwrapped and each cut down to three cubes of 25 mm and tested for compressive strength. The creep test load was then adjusted so that the stress on the sample corresponded to 10% to 15% of its strength at loading age, with a maximum of 50 kg (without considering the amplification from the lever arm). The environment was kept at 20°C and 70% RH in the testing rooms.

3.2.2 Compressive creep frames

The creep frames consisted of a class 2 lever, designed with a mechanical advantage of 10. The sample are placed between two steel loading plates, connected to the frame by steel balls to ensure a good load transfer and a correction of the alignment. Strain was monitored using 3 LVDTs placed between anchor points on the steel plates, see illustration on Figure 3.8. The sampling frequency was adapted over time. During the loading/unloading parts, sampling rate was set to 0.25 or 2 Hz. Rate was decrease to a reading every 20 seconds for the first hours after a load change, and further decreased to a reading every 20 minutes until the end of the test.

Cast iron weights were manually attached and hung at the far end of the lever arm. Rapid loading/unloading cycles were done at time of loading, in order to get a value for the Young's modulus of the specimen. These cycles simply consisted in fully loading the sample for some seconds to get some readings and then unloading it immediately. After a recovery period of a few minutes, another cycle would start. At the third loading, the masses were left in place for the proper creep test. As mentioned, these cycles allowed to obtain a measurement of the Young's modulus, but also allowed to settle the specimen in place, including a possible flattening of the top and bottom aluminium wrapping.

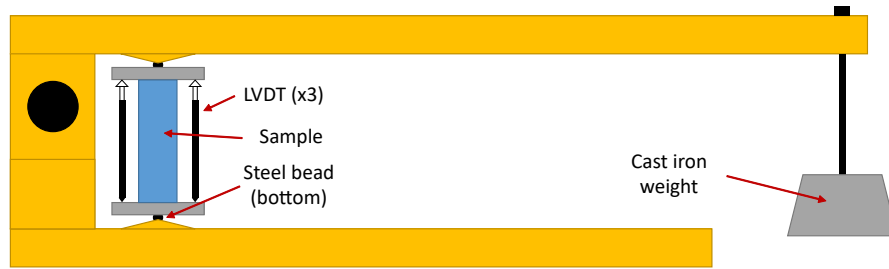


Figure 3.8 – Scheme of the compressive creep set-up. Bottom part and lever of the frame should ideally be kept horizontal during the test. Scale is approximate.

3.2.3 Results processing

Raw data went through some processing before being plotted (see Appendix A). Autogenous shrinkage (data in Chapter 4) is subtracted from the total measured strain to obtain creep strain, as creep and shrinkage strains are assumed to be independent in the frame of this study. Instantaneous, elastic strain from initial loading is removed from the plots, see Figure 3.9. Data is then presented as creep compliance J over loading time $t - t_0$, compliance being defined as creep strain divided by applied stress, see Eq. 3.1. This is a valid normalisation to compare specimens undergoing stage II creep, where strain is supposed to be linearly dependent to stress [43].

$$J(t - t_0) = \frac{\varepsilon_{tot}(t) - \varepsilon_{elas}(t_0) - \varepsilon_{auto}(t)}{\sigma(t_0)} \quad (3.1)$$

3.2.4 Basic creep kinetics

As discussed earlier, the macroscopic creep behaviour of cementitious materials can be approached by a power law or a logarithmic function. A straightforward fitting of compliance may not give sensible results. A better approach would be to fit the first time derivative of the dataset and integrate it back to approach the raw data. When using a power law to fit the compliance, this means the first derivative can be approximated with Eq. 3.2, or Eq. 3.3 when the problem is solved in the logarithmic domain. Note that Eq. 3.3 appears as a straight line in

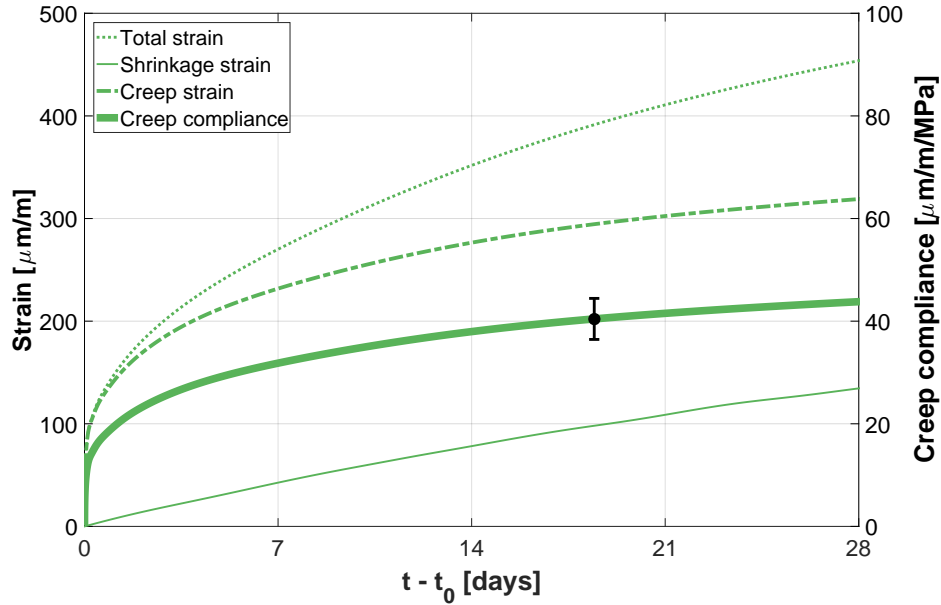


Figure 3.9 – This figure shows the intermediate steps to obtain creep compliance. Autogenous shrinkage strain is subtracted from the total strain measured by the creep set-up to obtain creep strain. This quantity is then divided by the applied stress to obtain the creep compliance. The error bar is representative for all the curves presented later. Most of the error comes from the total strain measurement.

a log-log plot.

$$\dot{j}(t - t_0) = e^k \cdot (t - t_0)^B \quad (3.2)$$

$$\ln(\dot{j}(t - t_0)) = B \cdot \ln(t - t_0) + k \quad (3.3)$$

When integrated over time, Eq 3.2 gives the indefinite integral

$$J(t - t_0) = A \cdot \frac{(t - t_0)^{B+1}}{B + 1} \quad (3.4)$$

where $A = e^k$ [mm/m/MPa · days^{B-1}] can be considered as an amplitude factor and B [-] is the slope of the creep rate.

The best way to fit experimental results with a log function is also to initially fit the first time derivative rather than the data directly. In that case, the time derivative is a rational function of the form

$$\dot{j}(t - t_0) = \frac{1}{C \cdot ((t - t_0) + \tau)} \quad (3.5)$$

whose primitive is

$$J(t - t_0) = \frac{1}{C} \cdot \log\left(\frac{(t - t_0)}{\tau} + 1\right) \quad (3.6)$$

where τ [days] is the characteristic time and C [mm/m-MPa] an amplitude factor corresponding to the slope of the compliance on a semi-log plot. As described in the appendix, 10-fold Tikhonov regularization was used here to obtain both the first derivative of the experimental data and a smoothed output. After processing the data, the first time derivative was fit with Eq. 3.3 or Eq. 3.5 using the least squares method. To determine whether the tested samples reached a logarithmic creep regime or still were in a state best described with a power law, the fitting was done using an expanding time window. The principle is to run the fitting repeatedly, adding more data points at the end of the set at each iteration. Doing so allows one to observe whether the fitting coefficients are stable over time and if the root-mean-square error is decreasing or stable. Unstable coefficients mean that the fitting function has to be re-adapted at each addition of data points, indicating that this function type is not well suited to describe the data (see Figure 3.10).

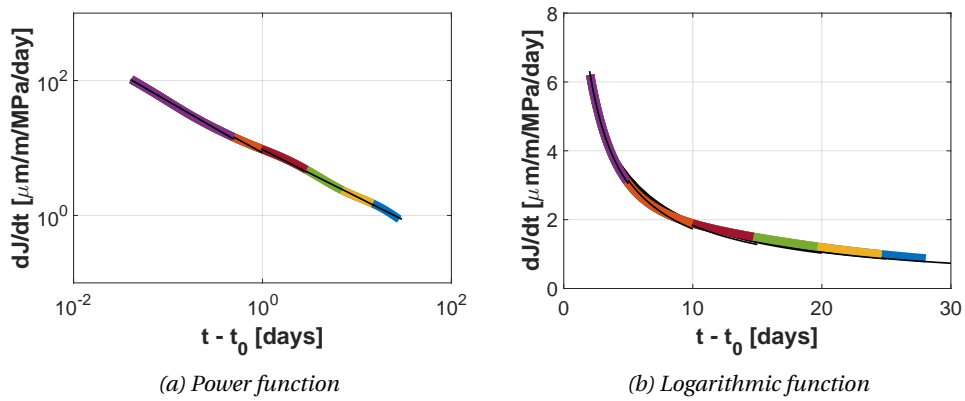


Figure 3.10 – In this example, creep compliance is back-calculated after fitting the first derivative either with Eq. 3.3 (a) or Eq. 3.5 (b). Fitting is done over an forward-expanding time window, represented by the segments of the thick curve from the experimental results. Both methods show a convergence of the fit towards the experimental data, indicating a stabilisation of the fitting coefficients.

This investigation showed that a power law could efficiently fit most of the datasets from 0.04 day on (1 h), whereas a logarithmic function was adequate only from 2 days on. Under these conditions, both approaches showed stable coefficients and stable or increasing RMSE. This seems to indicate that a power law is well suited to capture the initial kinetics of the data, while still performing quite well to fit the data up to the end of the test. A logarithmic function fits the late part of the datasets very well, but the increasing RMSE indicates that as more and more data points are considered, the fit loses quality. To check the fit further, the equations for the first derivative were integrated once and shifted so that the value at 30 days matches the experimental value (example on Figure 3.11). The error of this back-calculation was also estimated. Both methods gave good results, with an average RMSE of 1.1 for the power function and 0.6 for the logarithmic one. As a conclusion, we can suppose that the studied samples are still in a transition regime from power to logarithm. The presence of a transition time is in agreement with the early work of Bažant [10] and more recent studies as well [56], [33]. Nevertheless, both fitting methods need only a couple of coefficients to

Chapter 3. Basic creep on mature paste samples

be adapted. Comparing these coefficients can bring some hints regarding the similarities or differences among the studied mixes.

As mentioned in the Appendix A, the use of these simple models is only valid in the frame of this work to compare the different samples and probably not suited to long-term modelling of these materials. Indeed, the two proposed functions will inevitably diverge in the long term; the logarithmic function growing slower than any other type of function over long periods of time.

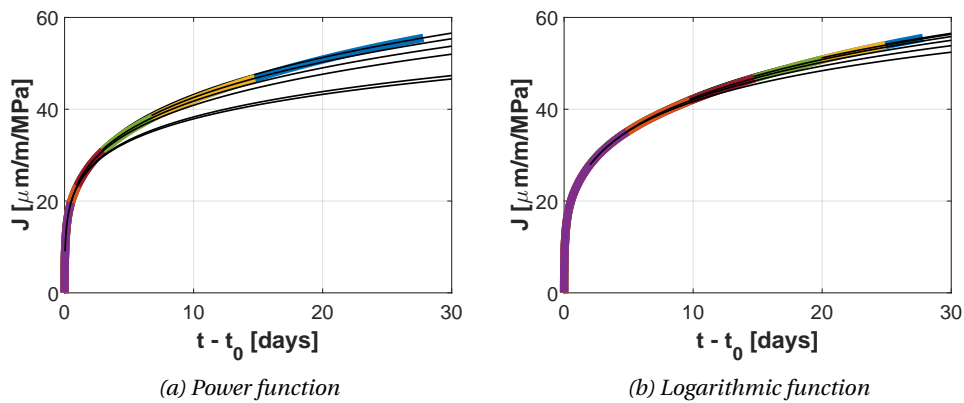


Figure 3.11 – In this example, creep compliance is back-calculated after fitting the first derivative either with Eq. 3.3 (a) or Eq. 3.5 (b) and integration. Fitting is done over an forward-expanding time window, represented by the segments of the thick curve from the experimental results. Both methods show a convergence of the fit towards the experimental data, indicating a stabilisation of the fitting coefficients.

3.3 Experimental results

3.3.1 Influence of cement type

Figure 3.12 summarizes the results for the plain cement systems, with varying cements and identical water content by mass. PC 0.4 and N4-PC 0.4 samples have a very similar creep behaviour, although the kinetics of the N4 sample could be slightly faster. The white cement from Aalborg shows a lower creep amplitude. Different mineralogy could be the reason for the difference.

Figure 3.13 shows the creep compliance for plain cement and LC³-50 mixes using different cements. The slightly lower compliance measured on the Normo 4 cement compared to the Heidelberg LabCement is not kept in the LC³, where the situation is opposed. LC³-50 mixes using pure metakaolin as SCM have a very similar and low compliance with both cements. Figure 3.14 compares the compliance relative to the plain cement samples at 7 and 28 days and the creep amplitude factor with the calcined kaolinite content of the LC³ samples. The relative compliance of LC³ is slightly decreasing over time.

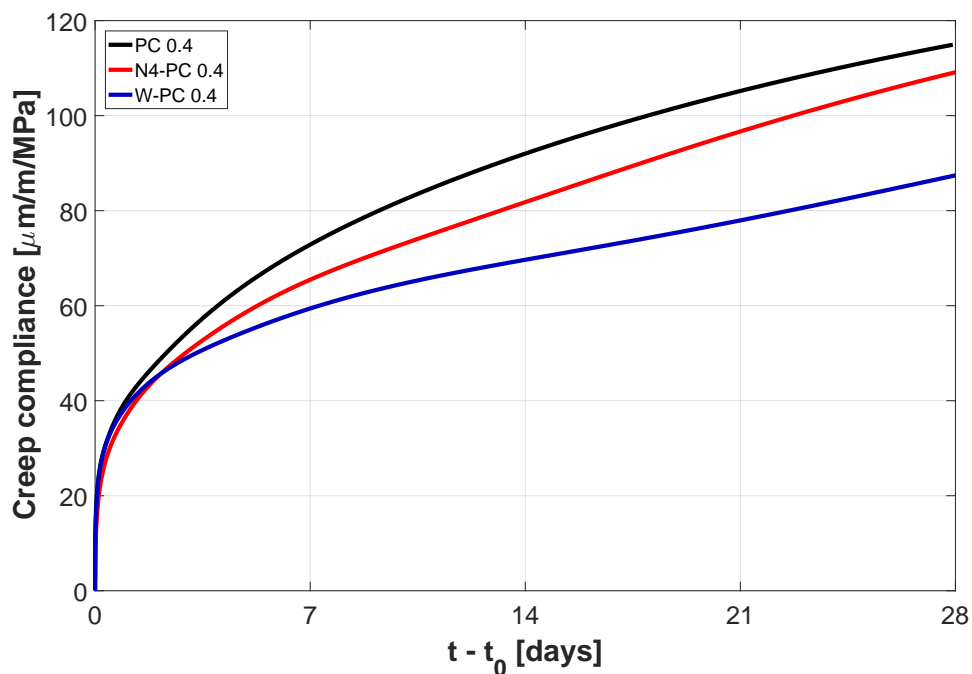


Figure 3.12 – Compressive creep compliance of the plain cement paste mixes (Heidelberg LabCement, LafargeHolcim Normo 4 and Aalborg white), starting 28 days after casting, for a duration of 28 days.

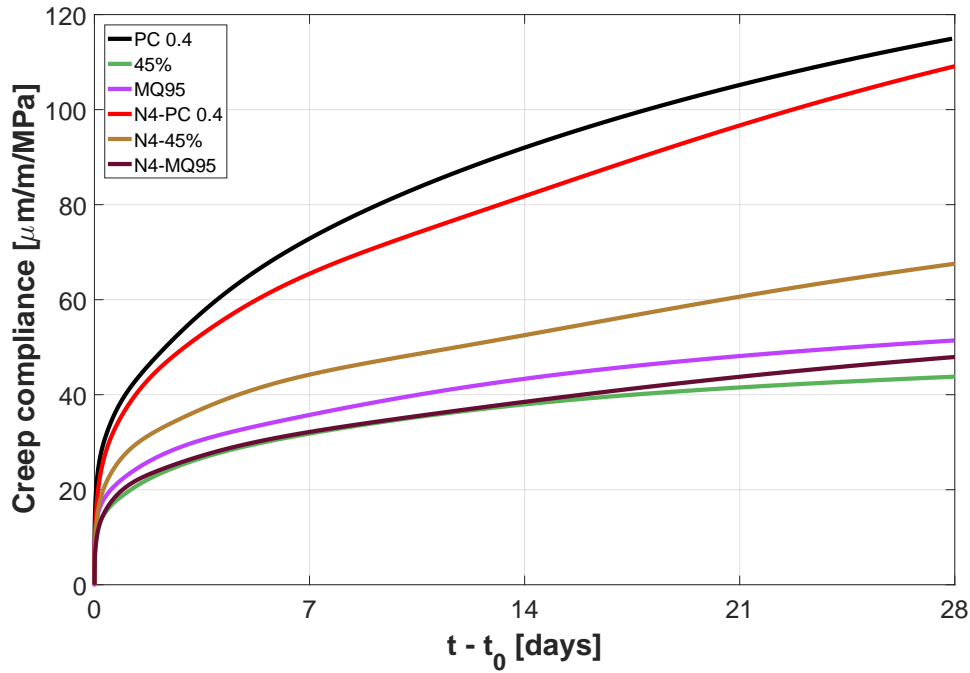


Figure 3.13 – Compressive creep compliance of plain cement and LC³-50 2:1 samples cast with different cements. A natural clay containing 45% of calcined kaolinite and a model clay with 95% pure metakaolin are used as replacement materials. All samples have a W/B of 0.4.

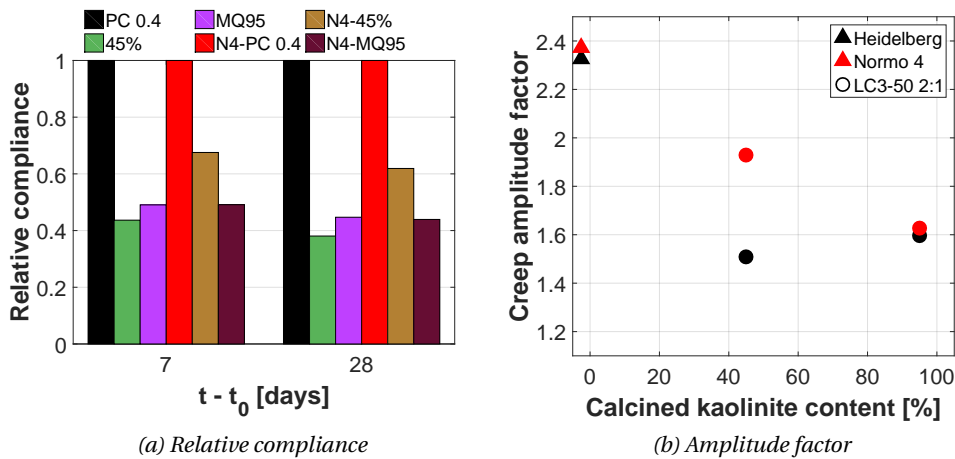


Figure 3.14 – a) The amplitude of creep compliance at 7 and 28 days is compared to the plain cement samples. b) The amplitude factor from the power law fit is compared to the calcined clay content of the clay. Plain cement mixes are shown off limits.

3.3.2 LC³ with natural calcined clays

Figure 3.15 shows the evolution of compressive creep compliance for mature LC³-50 samples, using various calcined clays of natural origin as replacement material. All of the ternary blends exhibit a lower compliance than the plain cement reference. One of the most striking features is the apparent independence of the grade of the clay on the resulting compliance of the mix. For a clay grade from 45% to 60%, the effect on compliance is quite similar. This could indicate that a threshold value exists for the initial metakaolin content to have a significant effect on the creep compliance. Nevertheless, these results indicate that even clays with only 25% of calcined kaolinite cause a reduction of basic creep compliance of mature paste. Figure 3.16a shows the evolution of compliance relative to the sample PC 0.4. LC³ with clays containing 45% to 60% of calcined kaolinite show about half the compliance of plain cement. The possible presence of a threshold is also visible on Figure 3.16b, where the fitted amplitude is similar for LC³ mixes with 45% grade clay or above.

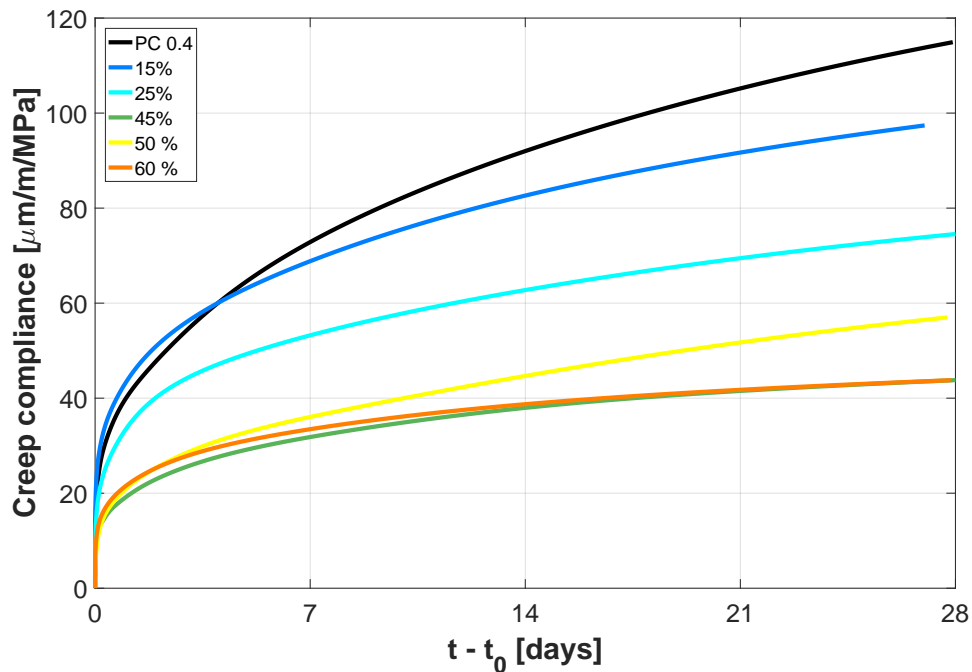


Figure 3.15 – Basic compressive creep compliance of the LC³-50 mixes with natural calcined clays of varying grade. All mixes are cast at a W/B of 0.4, creep tests started 28 days after casting.

Chapter 3. Basic creep on mature paste samples

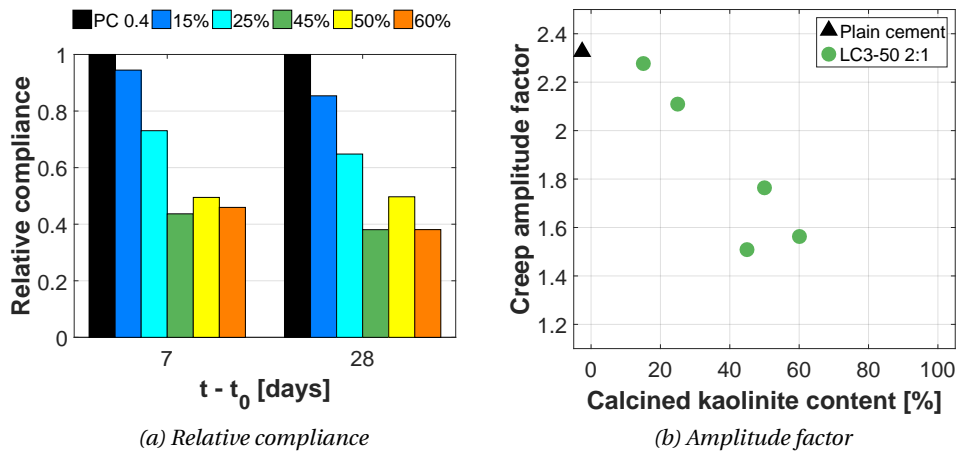


Figure 3.16 – a) The amplitude of creep compliance at 7 and 28 days is compared the PC 0.4 sample. b) The amplitude factor from the power law fit is compared to the calcined clay content of the clay. Plain cement is shown off limits.

Figure 3.17 presents the results for the LC³-50 and LC³-65 series with the same calcined clay but different calcined clay to limestone ratios. For the LC³-50, the change in calcined clay to limestone ratio did not affect compliance significantly. This is in line with the previous observations, as changing this ratio is equivalent to using a lower grade clay. The metakaolin content of this mixture is still sufficient to affect compliance. This is not the situation in LC³-65, where further blending of the clay limits the compliance reduction, but still being lower than the plain cement. Figure 3.18b plot the creep amplitude factor versus the initial metakaolin content of the mix. A clear trend is visible here, indicating that a minimal amount of metakaolin is required for a significant effect on compliance.

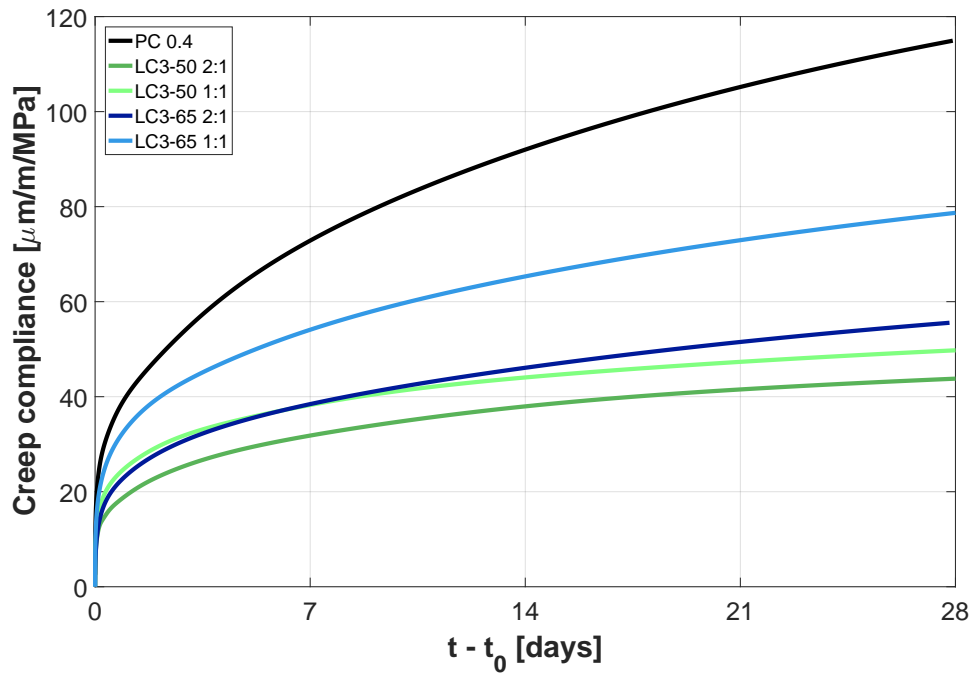


Figure 3.17 – Basic compressive creep compliance of the LC³-50 and LC³-65 mixes with varying calcined clay to limestone ratio. Samples cast at a WB of 0.4 and loaded after 28 days.

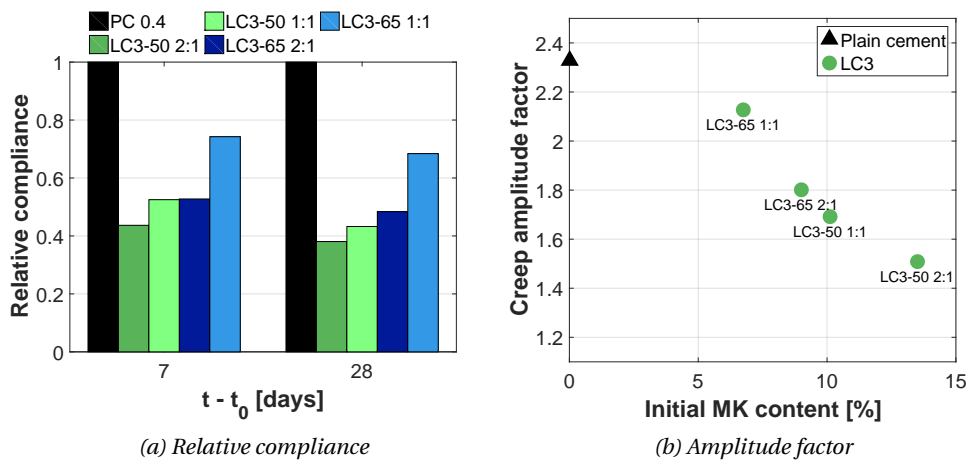


Figure 3.18 – a) The amplitude of creep compliance at 7 and 28 days is compared the PC 0.4 sample. b) The amplitude factor from the power law fit is compared to the initial metakaolin content of the binder.

3.3.3 Influence of initial water content

Figure 3.19 summarizes the results for mixes using binders at different W/B. Concerning the pure cement mixes (Heideberg LabCement and Aalborg white cement), it appears that the variation in W/C has a very limited effect on the compressive creep compliance of mature samples. However, increasing the initial water content of the LC³-50 45% mix dramatically affected its creep compliance. It is worth noticing that, starting at a similar W/S (PC 0.4 *vs.* LC³-50 45% 0.5, or PC 0.357 *vs.* LC³-50 45% 0.4), LC³ always shows a lower compliance than a plain cement paste. This feature is also illustrated on Figure 3.20b, where the fitted amplitude factor is compared to the initial water content of the mixes.

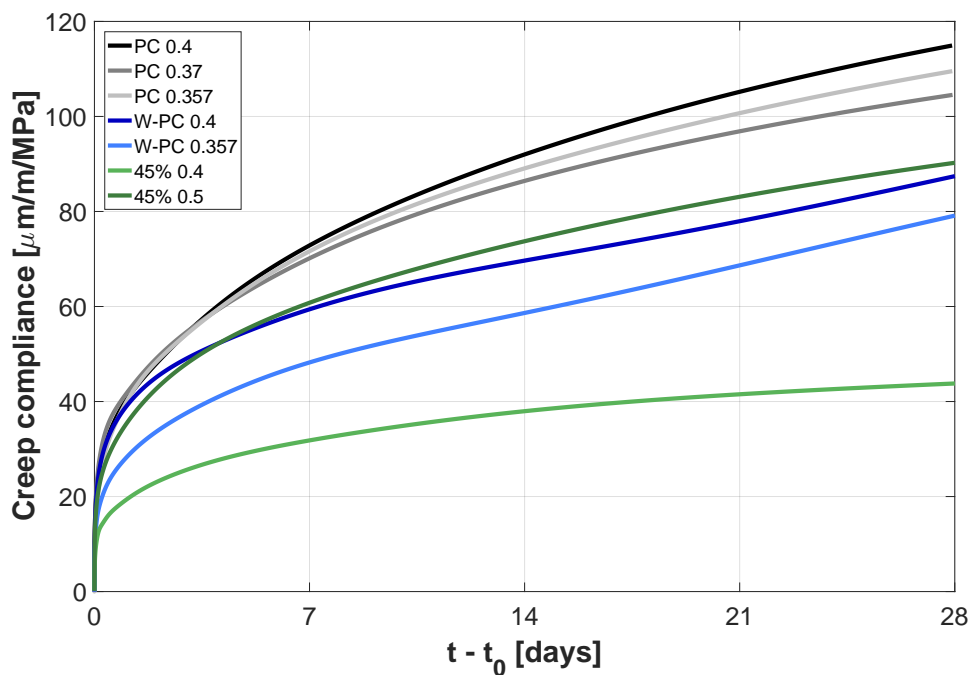


Figure 3.19 – Basic compressive creep compliance of mixes with varying W/B. The sample PC 0.357 has a similar W/S as the LC³-50 45% 0.4 sample, and the LC³-50 45% 0.5 has a similar W/S as the PC 0.4.

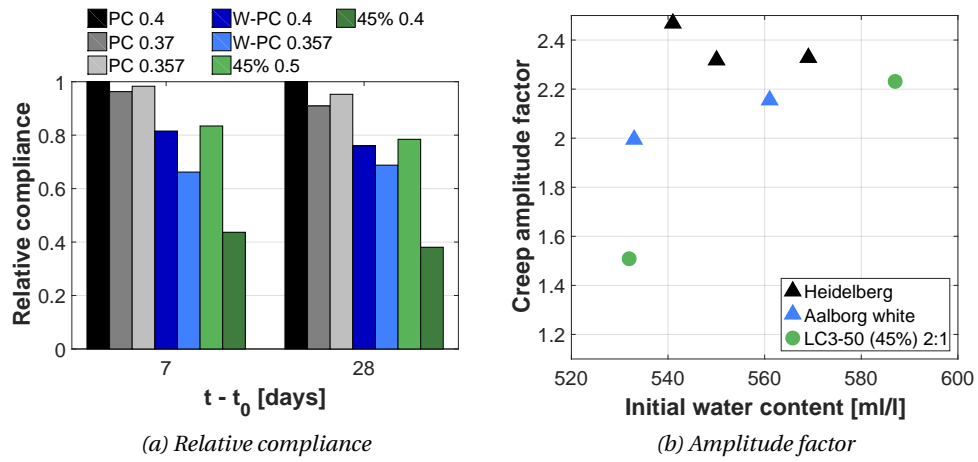


Figure 3.20 – a) The amplitude of creep compliance at 7 and 28 days is compared the PC 0.4 sample. b) The amplitude factor from the power law fit is compared to the initial water content.

3.3.4 Model clays

Figure 3.21 presents compliance over loading time for all the mixes using pure metakaolin and quartz powder to model calcined clay, as well as their plain cement counterpart. In accordance with what was observed with natural clays, the reduction of compressive creep compliance is comparable when using model clays containing 40% to 95% of metakaolin. The initial trend from plain cement seems to hold when using the same cement in a LC³. For instance, LC³ mixes using Aalborg white cement (W- series) have a slightly lower compressive creep compliance when compared to other LC³-50 mixes, and such is the case for the plain cement samples. Figure 3.22b confirms that the creep reduction is comparable with all model clays.

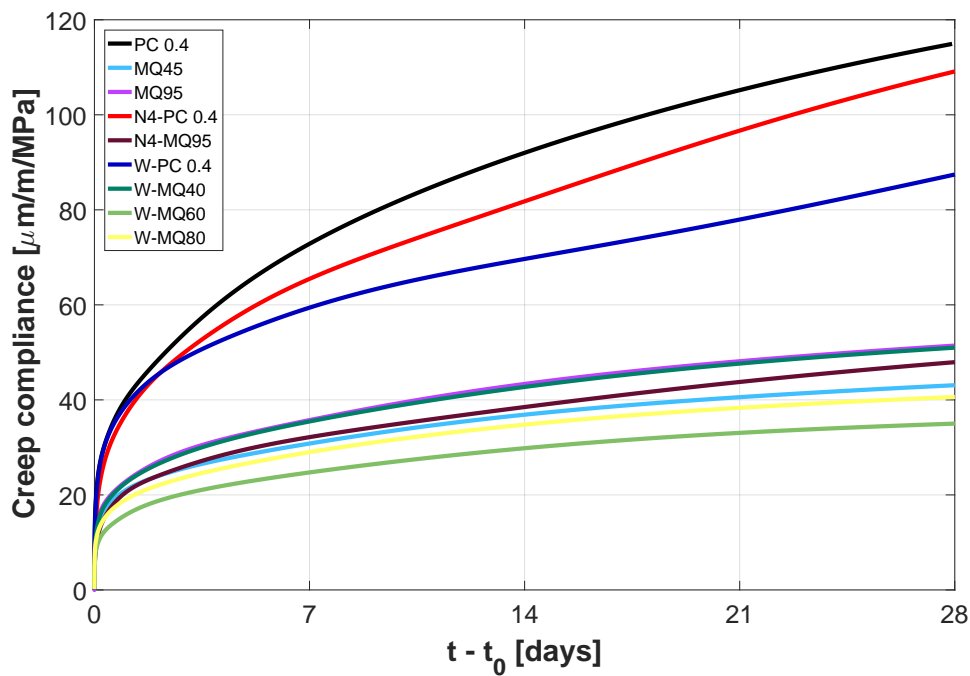


Figure 3.21 – Basic compressive creep compliance of the LC³-50 mixes using model clays.

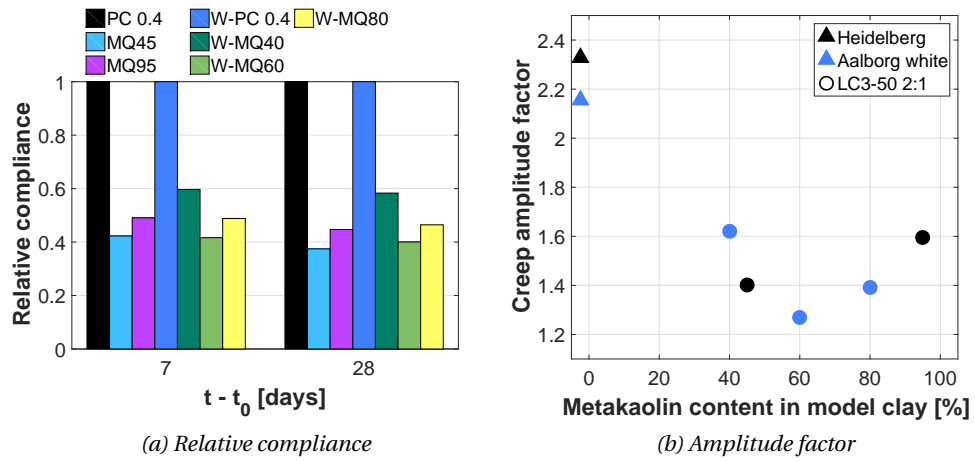


Figure 3.22 – a) The amplitude of creep compliance at 7 and 28 days is compared the plain cement samples. b) The amplitude factor from the power law fit is compared to the metakaolin content of the model clay. Plain cement mixes are shown off limits.

3.3.5 Fitting results

The fitting coefficients are summarized in Table 3.1, along with the RMSE of the integrated fit. The exponent B is consistent with the results from other researchers [54], [53], [46], [56], [29]. A quick statistical analysis of the coefficients using the Student's t-test, after grouping the samples by cement type (plain cement and LC³-50 mixes), showed that the coefficient B from the power law did not differ significantly among the groups ($p > 0.05$). This indicates that the slopes of the first derivatives on a log-log plot are similar for all mixes and that, after integration, the power laws all have a similar exponent. Differences between samples are explained by the amplitude factor A , which is statistically different between PC and LC³-50 ($p < 0.02$). A similar situation occurs when analysing the statistics of the logarithmic coefficients. Characteristic time τ does not vary significantly between plain cement mixes and LC³-50 ($p > 0.5$). Similarly to the power law, the amplitude factor $1/C$ of the logarithmic function is

Table 3.1 – This table summarizes the coefficients that best fit the experimental data when using a power law (Eq. 3.4) or a logarithmic function (Eq. 3.6). The first derivative of the data is fit using the derivative of the fitting function and integrated back. The RMSE between the integrated fit and the raw data is then computed.

Label	Power			Logarithm		
	A	B	RMSE _{int}	1/C	τ	RMSE _{int}
PC 0.4	11.7	-0.66	1.81	37.9	3.34	0.31
PC 0.37	11.2	-0.73	2.05	30.0	2.78	0.11
PC 0.357	12.5	-0.72	1.44	33.6	2.97	0.19
15%	9.9	-0.72	0.28	24.8	2.57	0.37
25%	8.2	-0.77	0.34	16.6	1.94	0.98
45% 2:1	4.8	-0.77	0.44	9.4	1.12	0.21
45% 1:1	5.4	-0.82	0.27	8.8	0.78	0.09
45% 0.5	9.6	-0.70	0.37	23.6	2.11	1.18
N4-45%	7.4	-0.74	2.13	22.3	5.05	1.58
50%	6.3	-0.72	1.39	19.4	4.51	0.92
60%	4.7	-0.81	0.35	7.8	0.67	0.09
LC3-65 2:1	6.4	-0.77	0.63	13.9	2.23	0.61
LC3-65 1:1	8.6	-0.75	0.64	21.3	2.92	0.34
MQ45	4.4	-0.78	0.70	11.1	3.47	0.22
MQ95	5.3	-0.74	0.51	13.4	2.91	0.22
N4-PC 0.4	11.7	-0.68	3.93	46.7	6.94	1.90
N4-MQ95	5.4	-0.76	1.06	14.6	4.32	0.70
W-PC 0.4	9.3	-0.78	1.67	23.2	3.71	1.43
W-PC 0.357	7.9	-0.68	1.93	28.1	5.26	1.47
W-MQ40	5.4	-0.76	0.65	13.2	2.77	0.22
W-MQ60	3.7	-0.75	0.20	8.9	2.76	0.14
W-MQ80	4.1	-0.75	0.29	10.4	2.90	0.17

higher for cement mix than for LC³-50 ($p < 0.01$). This is an expected result, as coefficient C is dependent on the material, whereas τ depends on the degree of hydration at loading [33]. It is worth pointing out that the amount of measurements is very limited — especially for the mixes with white cement — and that the fitting coefficients are likely to change if considering more data points. Figure 3.23 contains all the plots of the compliance rates over loading time.

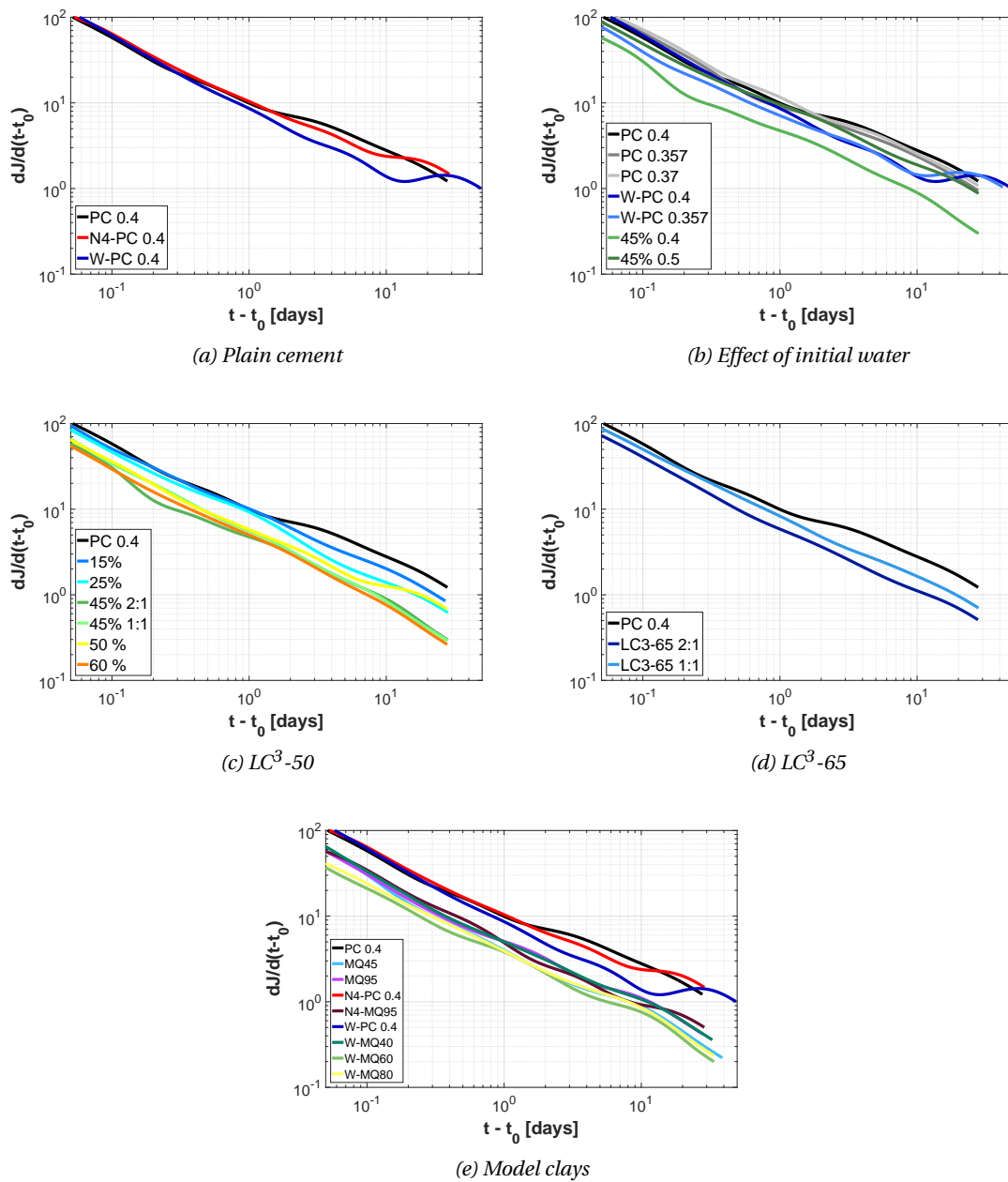


Figure 3.23 – Creep rate of all the studied mixes separated into different groups on log-log plots.

3.3.6 Creep rate and microstructure

The following part is a first attempt to draw some links between the creep coefficients from the different fits and characteristics of the microstructure. As discussed earlier, C–S–H is believed to be the main phase responsible for creep in cementitious materials. Moreover, most theories trying to explain it locate the load transfer phenomena at the nanoscale. Figures 3.24 and 3.25 show the amplitude parameters from the power law and the logarithmic fit versus the volume fraction of C–S–H obtained by mass balance at the age of loading. In both cases, the plain cement mixes are located in the top-right region of the plot and most of the LC³ mixes in the bottom-left part. This seems to indicate that a higher C–S–H content is likely to cause more creep, although it might not be the only factor affecting compliance, as the scatter is considerable. As presented in Chapter 2 on Table 2.7, the average C–S–H chemical composition can widely vary from plain cement mixes to LC³-50 using pure metakaolin, such as the MQ95 mix. As illustrated on Figure 3.26, this chemical variation is correlated to a change in creep amplitude, but the data does not allow to identify a causal link between these quantities. All the observations set the basis for further investigation, attempting better to explain the decrease in compliance due to the presence of limestone and calcined clays, thanks to numerical models.

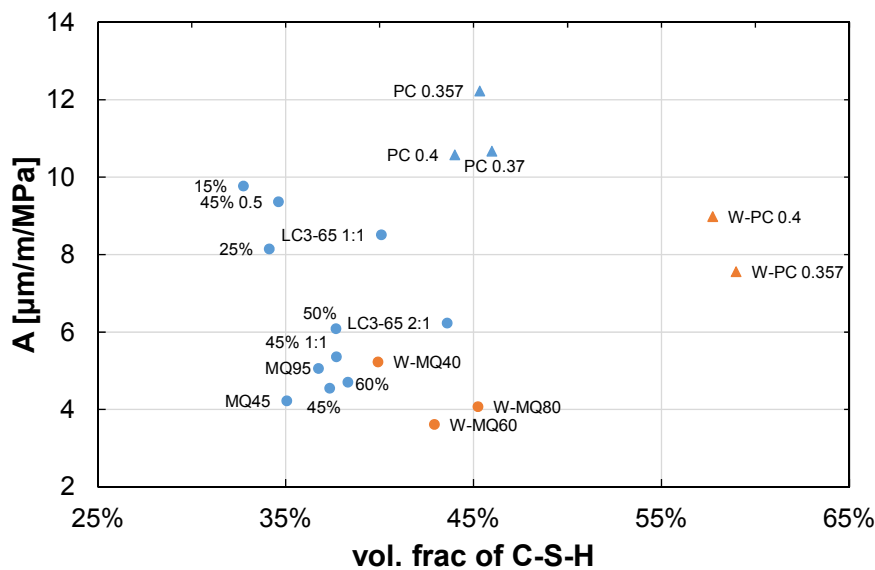


Figure 3.24 – This plot compares the creep amplitude from the power law fit to the C–S–H content at the time of loading. Data are grouped according to the cement used. It appears that the amount of C–S–H is correlated to the creep amplitude, but is not enough to explain all the effects.

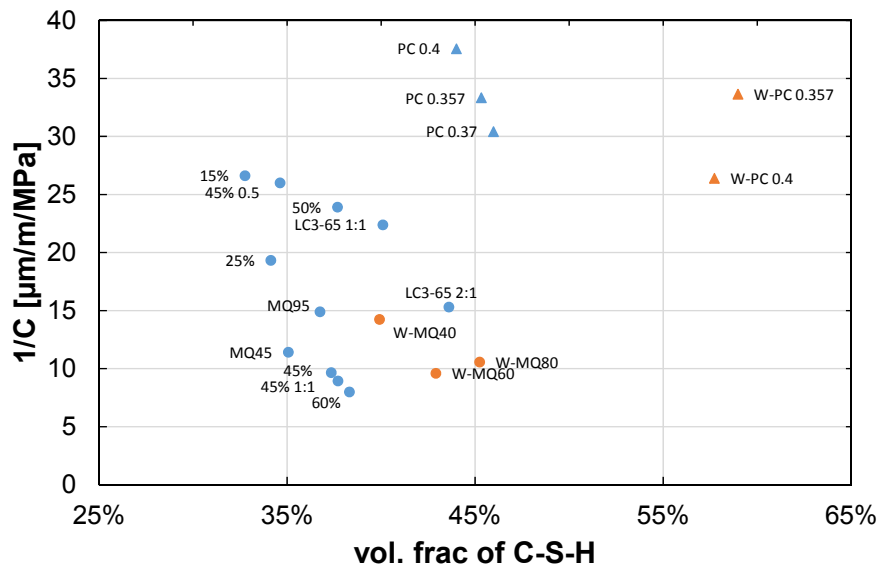


Figure 3.25 – This plot compares the amplitude factor from the logarithmic fit to the C–S–H content at the time of loading. Data are grouped according to the cement used. It appears that the amount of C–S–H is correlated to the creep amplitude, but is not enough to explain all the effects.

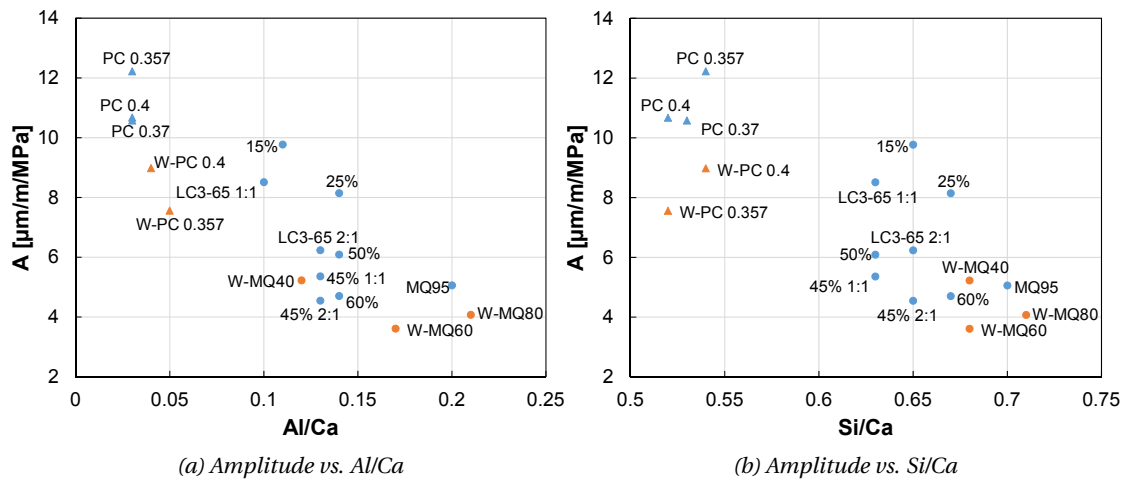


Figure 3.26 – These plot compare the creep amplitude from the power law fit to the average C–S–H composition from SEM-EDS. The inclusion or aluminium or silicon is associated with a decrease in creep amplitude.

3.3.7 Summary of the results

This set of experimental results allowed the following observations:

- The replacement of a fraction of the cement with limestone and calcined clay causes a decrease of the basic creep compliance of samples cured for 28 days before testing.
- In the LC³-50 2:1 design, a reduction of compliance is observed already when using a clay containing as little as 25% of calcined kaolinite. Figure 3.27 shows the evolution of the creep amplitude factor from the power law fit with initial metakaolin content for mix designs with a W/B of 0.4. There is a limit around 12% of initial metakaolin above which the decrease in compliance is not significant. This limit actually corresponds to the minimal amount of metakaolin required to consume all the available portlandite from clinker hydration.
- When comparing LC³ to plain cement, either at equivalent W/B or W/S, LC³ always shows lower compliance. However the relative effect of increasing the initial water content had more impact on LC³.

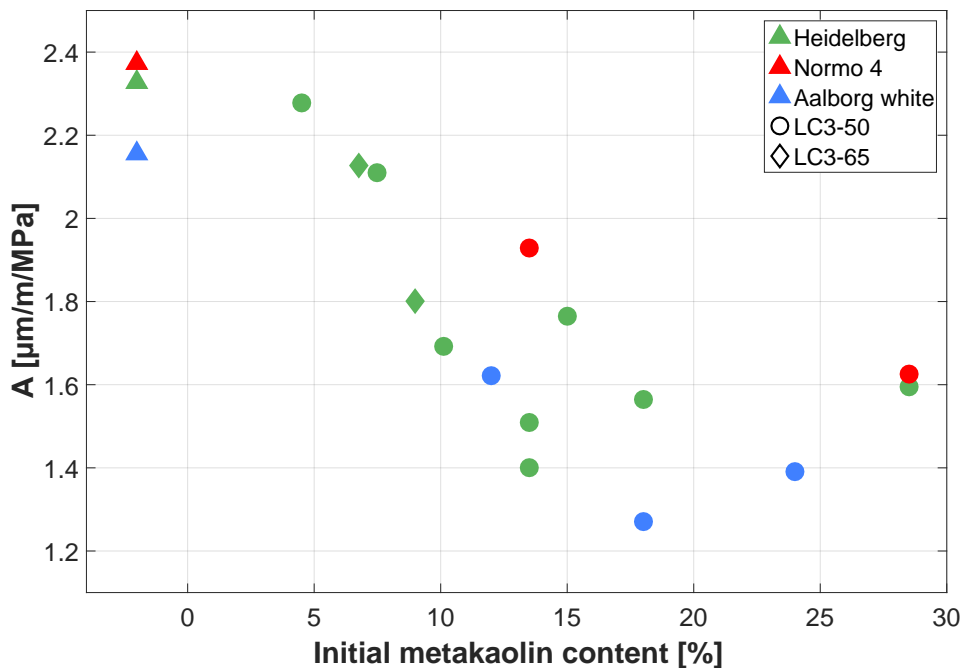


Figure 3.27 – This graph shows the evolution of the fitted creep amplitude factor from the power law fit with initial metakaolin content for mixes with a W/B of 0.4. The amplitude factor is not decreasing significantly after a threshold value of about 12% of initial metakaolin content.

3.4 Modelling

In order to shed some light on the question whether creep behaviour of LC³ is different from that of PC because of a different C–S–H or because of a different microstructure, a multi-scale modelling approach through finite elements was used. The purpose of the simulation is to try to back-calculate the intrinsic visco-elastic properties of the C–S–H gel, starting from known phase assemblage and macroscopic mechanical properties. To this end, a finite element model was used to simulate the material at the sub-millimetre scale, then a statistical model was used to compute the properties of bulk C–S–H gel. This model will help to estimate the contribution of C–S–H amount and capillary porosity to the visco-elastic behaviour of the materials. A phenomenological model was also used to provide necessary inputs for autogenous shrinkage simulation. This second model consists of an ageing Kelvin-Voigt chain.

3.4.1 Finite Elements Modelling

A two-dimensional finite element model using the framework AMIE, similar to that described in [22] was adopted for this study. It consists of a 100 by 100 μm 2D mesh describing a square section of composite material undergoing uniaxial load (see Figure 3.28). Round inclusions representing crystalline anhydrous or hydrated phases are embedded in a matrix of C–S–H. The inclusions only possess elastic properties and are defined by their Young's modulus, Poisson's ratio, abundance and particle size distribution. Phases were regrouped by similar mechanical properties, summing their amount. In total, five elastic phases were used to represent the different families of minerals present in cement or LC³ mixes. Their mechanical properties are summarized in Table 3.2. The inclusions were spread in the domain and their diameters varied from 15 nm to 2 μm , according to a normal distribution. All the phase amounts come from the volume balance calculation. The amount of matrix corresponds to the space not occupied by the crystalline inclusions, that is to say, C–S–H gel, capillary water and air voids from chemical shrinkage. Space was tessellated with about 50'000 triangles.

Table 3.2 – Mechanical properties of the elastic phases used in the finite element model.

Phases	Young's modulus [GPa]	Poisson's ratio	Source
C ₃ S, C ₂ S, C ₃ A, C ₄ AF	130	0.3	[59]
CH, Mc	38	0.305	[17], [38]
Ett, MK, Clay	22.4	0.255	[17], [38], [4]
Ms, Hc, Ht, Hg	42.3	0.324	[17], [38]
SiO ₂ , LS	80	0.25	

The first step of the simulation is to assign a Young's modulus to the C–S–H matrix, in order to obtain a total strain of the material similar to that obtained during the load/unloading cycles on the creep frames. To that end, the matrix so far only has elastic properties, so that all strains are independent in time. In this case, a single time step has to be modelled, as all the materials are purely elastic. For moderate variations in stiffness, a linear relation between the

Chapter 3. Basic creep on mature paste samples

Young's modulus of the C–S–H matrix and that of the whole microstructure can be assumed. Hence, only a couple of attempts are necessary before being able to make a reasonable guess at the right properties. Once the elastic properties are fixed, the viscous properties have to be adapted to match the experimental data. In that case, as the C–S–H matrix is supposed to be the only viscous phase, its behaviour is qualitatively based on that of the macroscopic sample. A Kelvin-Voigt chain composed of 6 elements was used to model the rheological behaviour. The chain had characteristic times of 0.002, 0.02, 0.2, 2, 20 and 200 days and the rigidity of the springs was adapted to minimize the difference with the experimental data. The choice of the characteristic times is purely arbitrary, as this chain is there to model the phenomenon and not the actual physical processes. The time steps of the visco-elastic simulation were adapted to the characteristic times of the dashpots: the initial time step was set to $5 \cdot 10^{-4}$ days (below 1/3 or the fastest damper) and multiplied by 1.25 at the end of each iteration. Eventually, the proper visco-elastic behaviour of the C–S–H matrix required to fit the experimental results was obtained by trial and error, scaling the rheology model to the right amplitude.

As mentioned earlier, the C–S–H matrix is composed of C–S–H gel, capillary water and air voids. The computational power and knowledge of the microstructure at the C–S–H gel level is insufficient yet to model the C–S–H nanostructure explicitly using finite elements. Therefore, the C–S–H matrix is simply considered as a porous medium, and an analytical approach is adopted to estimate the properties of the solid material. It is possible to calculate what the properties of bulk C–S–H gel would be, knowing the amount of porosity and making some assumptions about its shape. The relation between porosity, properties of the porous material and properties of the bulk material comes from the work of Roberts and Garboczi [45]. In their study, the authors compared computationally the strains of bulk and porous

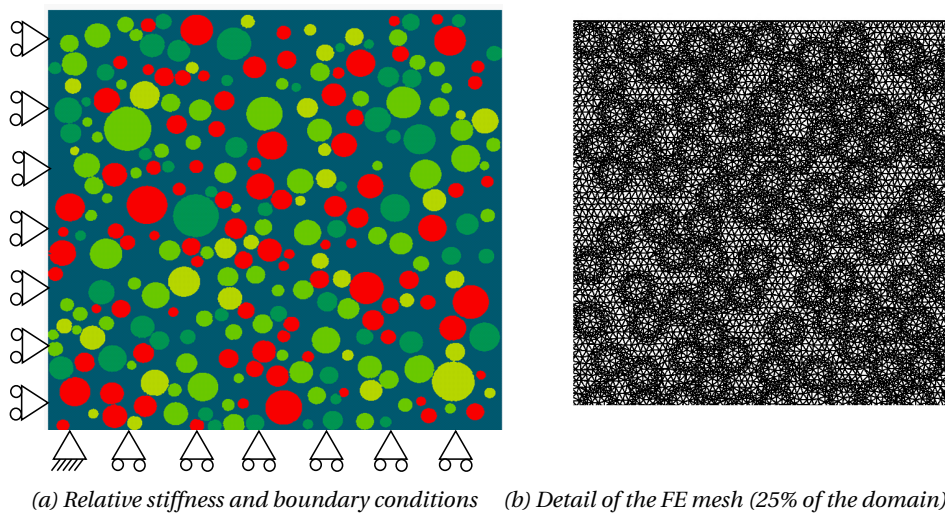


Figure 3.28 – a) This scheme represents a microstructure generated from the input of the mass balance. Each colour corresponds to a stiffness and a family of phases. Boundary conditions are also represented. b) The typical mesh size is visible on this schematic.

materials. According to their results, there exists a scale factor f linking the stiffness (or strain) of the porous medium to that of the same bulk medium, depending on the amount of porosity and its geometry. They tested many shapes and distributions of porosities: growing solid spheres, spherical or oblate pores growing in a solid and a series of Gaussian random fields (GRF, example on Figure 3.29). These latter are the most interesting when modelling the porosity of a heterogeneous medium such as cementitious materials.

In the studied systems, porosity of the C–S–H matrix is defined as the ratio between the volume of capillary water and air voids, and the total volume of capillary water, air voids and C–S–H gel. All these data come from the volume balance calculation. Published studies on C–S–H properties evaluate its Young's modulus ranging from about 20 GPa for so-called "low density C–S–H" to 30 GPa for "high density C–S–H" [57], [38], [26]. No distinction is made here between different types of C–S–H — be it in the mass balance or the modelling — so we must assume the Young's modulus of an average C–S–H to be within the range from 22 GPa to 28 GPa. Taking this into account and considering the range of porosity of the C–S–H matrix, the model giving a reasonable estimate of the C–S–H gel stiffness is the two-cut GRF (see Eq. 3.7).

$$f(p) = \left(\frac{p - p_0}{1 - p_0} \right)^m \quad (3.7)$$

with p the solid fraction of the medium, $p_0 = -0.064$ and $m = 2.09$. After setting the elastic properties of the C–S–H matrix, it is then possible to use this analytical method to estimate

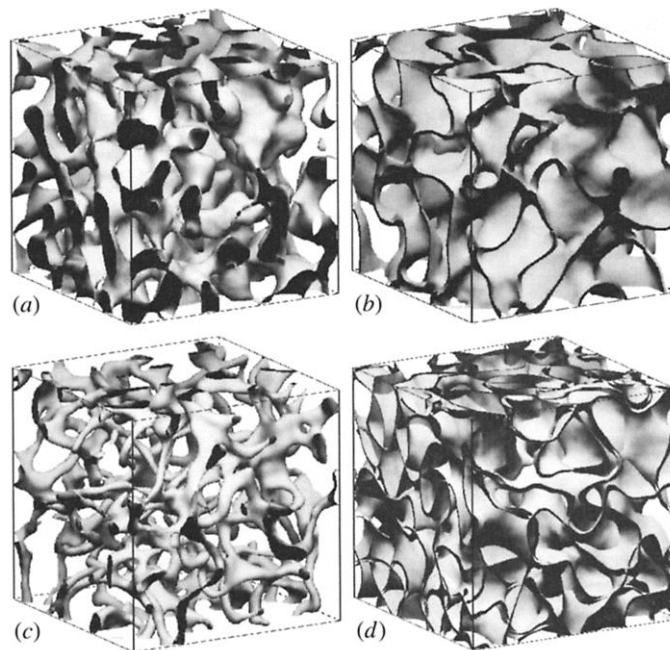


Figure 3.29 – This figure from [45] shows visualisations of four different types of 3D Gaussian random field: a) Single-cut. b) Two-cut. c) Open-cell d) Closed-cell. The two-cut model was selected in the present study.

Chapter 3. Basic creep on mature paste samples

the Young's modulus of C–S–H gel. The analysis was pushed a bit further, including the gel pores of C–S–H as part of the porosity of the matrix as an attempt to estimate of bulk C–S–H. The volume of the gel pores was estimating considering that 4 (total water in C–S–H) - 1.8 (interlayer water) = 2.2 molecules of water were occupying the gel pores per mole of C–S–H, considering an average molar volume of 240 ml/mol. A summary of the solid fractions, corresponding scale factor, and Young moduli of C–S–H matrix and gel is presented on Table 3.3.

Table 3.3 – This table summarizes the properties of the C–S–H matrix and gel resulting from the finite element modelling, along with the solid fraction in the matrix and the corresponding scale factor from the two-cut GRF

Label	C–S–H _{matrix} (GPa)	Solid fraction	Scale factor	C–S–H _{gel} (GPa)	C–S–H _{bulk} (GPa)
PC 0.4	11.6	0.70	0.50	23.0	67.9
PC 0.37	11.3	0.72	0.53	21.3	64.9
PC 0.357	13.4	0.75	0.58	23.2	73.8
W-PC 0.4	12.5	0.78	0.61	20.3	67.5
W-PC 0.357	12.6	0.81	0.66	19.1	64.4
15%	6.9	0.49	0.26	26.7	90.5
25%	8.9	0.57	0.33	26.6	76.0
45% 2:1	10.3	0.65	0.43	23.9	69.2
45% 1:1	9.1	0.64	0.42	21.9	62.1
45% 0.5	7.0	0.55	0.31	22.3	63.2
50%	8.3	0.62	0.39	21.1	63.7
60%	8.8	0.63	0.41	21.4	64.1
LC3-65 2:1	9.6	0.68	0.47	20.2	61.7
LC3-65 1:1	9.5	0.64	0.42	22.5	67.7
MQ45	8.5	0.58	0.35	24.0	69.0
MQ95	8.9	0.60	0.38	23.5	65.2
W-MQ40	9.0	0.62	0.39	23.0	71.2
W-MQ60	9.6	0.65	0.44	22.0	65.8
W-MQ80	10.0	0.68	0.47	21.3	64.3

A noticeable result from the elasticity modelling is the narrow range of stiffness found for the C–S–H gel. The Young's modulus of C–S–H gel back-calculated using the analytical approach is estimated to be in the range of 20 to 25 GPa for most mixes. In spite of the fact that the stiffness of the C–S–H matrix can double between the softest and the hardest one, the varying solid fraction of this porous matrix and the adopted model suggest that the solid forming said matrix has similar mechanical properties in all situations. In addition, this property is almost constant throughout samples with chemically different C–(A)–S–H.

This observation is also valid for the calculated elastic properties of bulk C–S–H. In this case, most of the values of Young's moduli fall within a narrow range from about 60 to

75 GPa. As a matter of fact, this is only slightly lower than the value reported by Jia *et al.* [30] for tobermorite, modelled using DFT. As the validity of the poro-mechanical approach is not guaranteed for such a range of pore sizes, the rest of the interpretation is carried out at the C–S–H gel scale only, including gel pores in the medium.

Modelling of the visco-elastic behaviour of bulk C–S–H is carried out using the same analytical tools as for elasticity. It was supposed that the visco-elastic response was affected in the same way as the elastic one. Therefore, the same scale factor f could be used to determine the viscous response of the C–S–H gel from the behaviour of the matrix. Results from the finite element model reached a good agreement with the experimental data for all simulated systems. As shown in the example of Figure 3.30, it is then possible to obtain the compliance of the C–S–H matrix and the compliance of the C–S–H gel out of the simulation results. The compliance of the different simulated microstructures is shown on Figures 3.31 to 3.34.

A remarkable result from these simulations is the prediction of a different C–S–H compliance between plain cement samples and LC³, combined with a very consistent prediction within the plain cement or the LC³ groups of samples. Notably, the samples of LC³-50 15%, 25% and 45% 0.5 — previously showing higher creep strains at the macroscopic level than the other LC³-50 mixes (see Figures 3.15 and 3.19) — can be modelled using C–S–H gel with similar visco-elastic properties as the other LC³. It appears that the changes in abundance *and* porosity of the matrix are enough to explain most of the variations among samples. The model also indicates that C–S–H gel present in plain cement could be less viscous than that of LC³. As the simulation is not carried out at the nanometric scale, the difference in viscous behaviour cannot be attributed to specific mechanisms without further investigation. As suggested in [58], a different packing of C–S–H particles could be an explanation for the macroscopic behaviour.

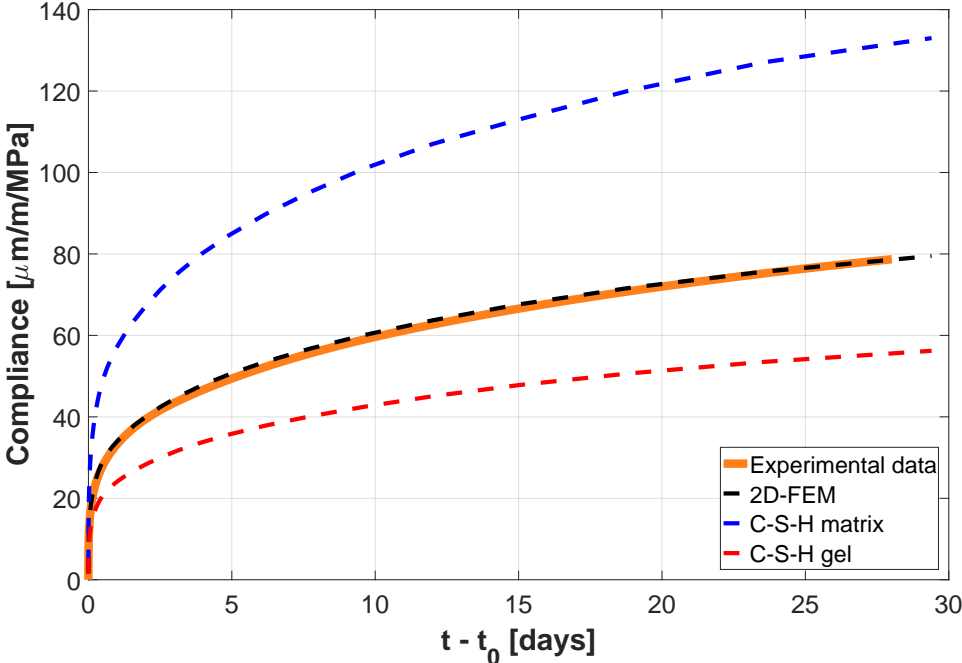


Figure 3.30 – This example shows how the FE model (dashed black) can approach the experimental results (solid orange). The dashed blue curve then show the viscous behaviour of the C–S–H matrix. The analytical model can them be used to estimate the behaviour of the solid C–S–H gel (dashed red) forming the porous C–S–H matrix.

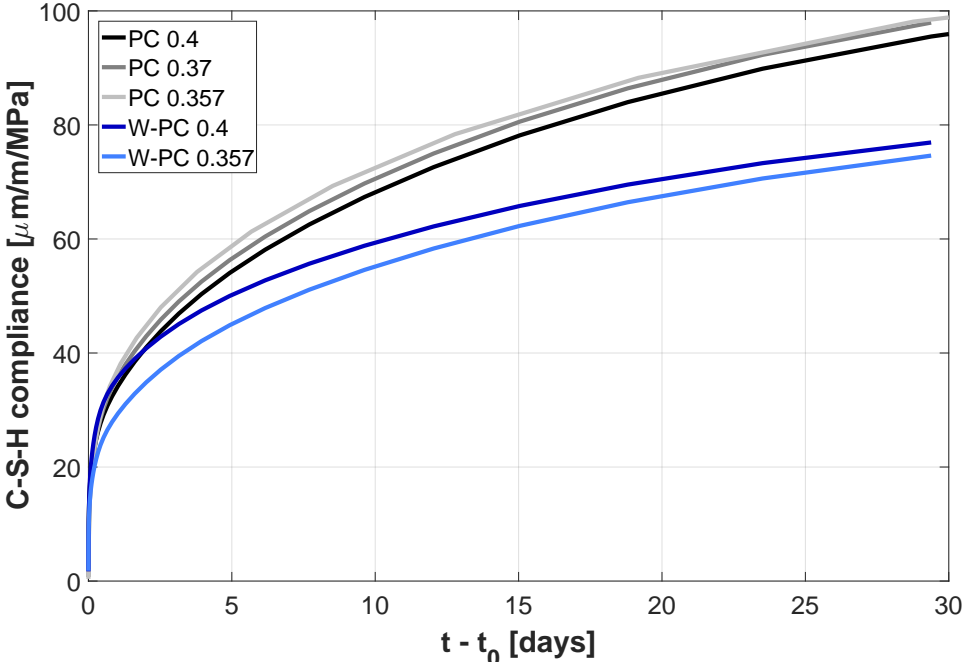


Figure 3.31 – C–S–H gel compliance calculated from the statistical model for the cement paste mixes.

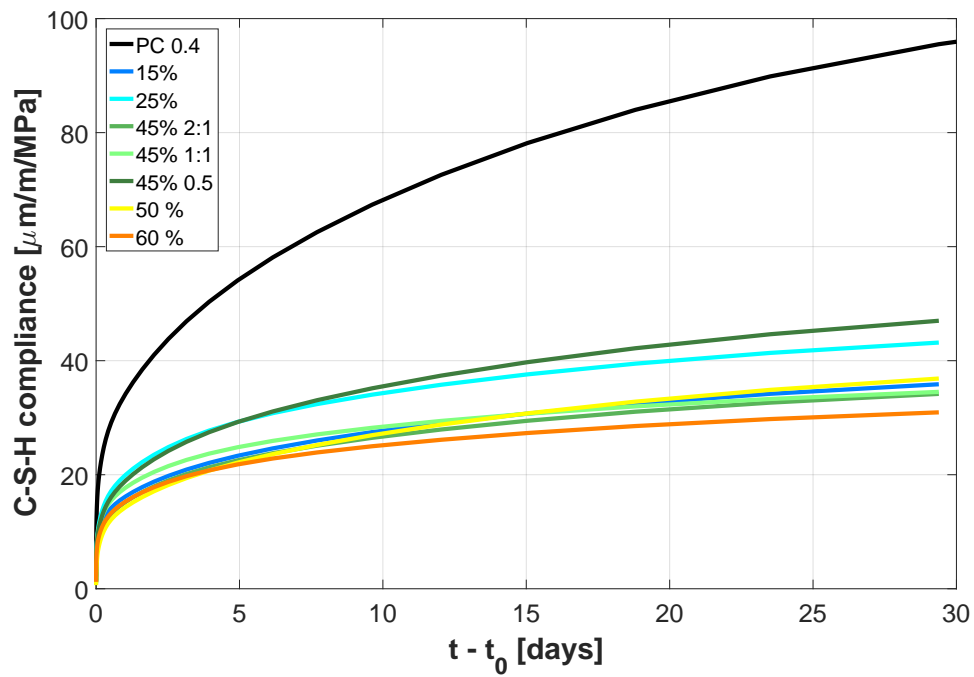


Figure 3.32 – C–S–H gel compliance calculated from the statistical model for the LC³-50 mixes using natural clays.

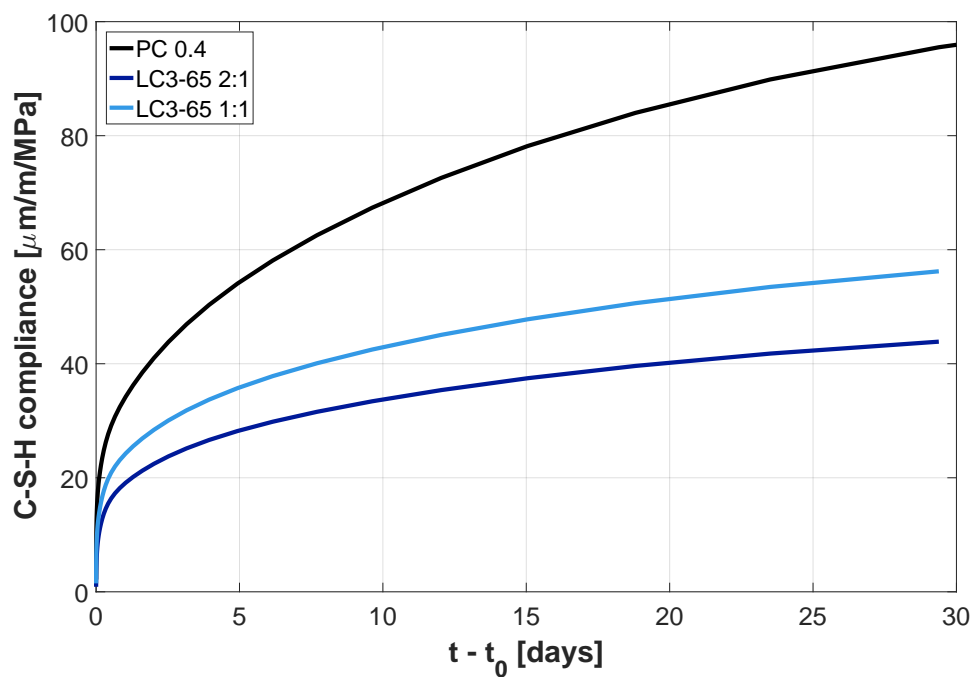


Figure 3.33 – C–S–H gel compliance calculated from the statistical model for the LC³-65 mixes.

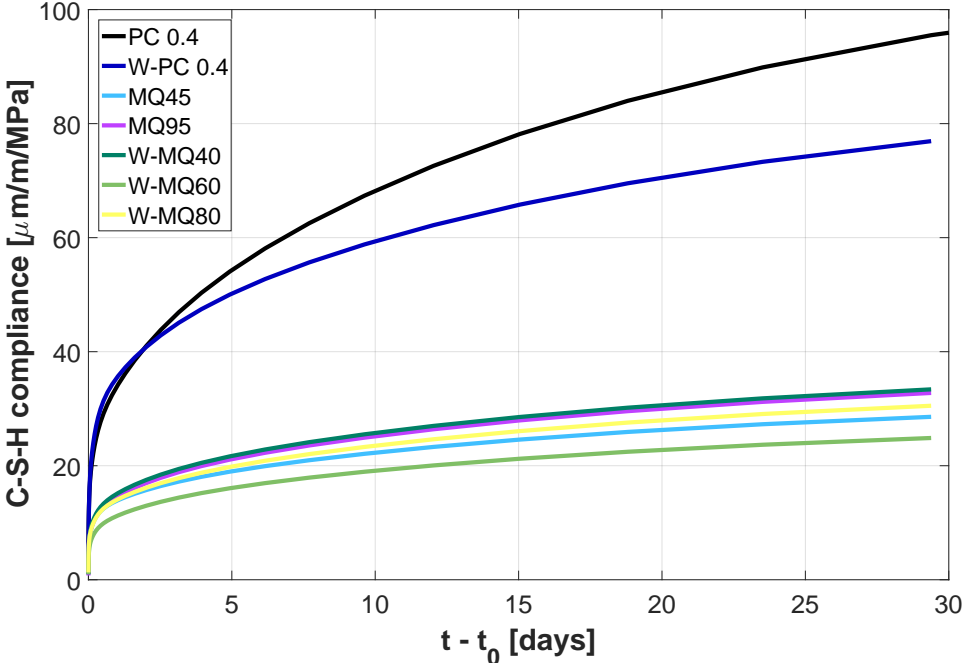


Figure 3.34 – C-S-H gel compliance calculated from the statistical model for the LC³-50 mixes using model clays.

3.4.2 Rheological modelling

A series of samples from the PC 0.4 and LC³-50 45% mix were tested at different loading ages in order to be fit using an ageing Kelvin-Voigt rheological model. The purpose is to apply a similar methodology to the one described in Chapter 5 of Hu's thesis [27] to a material with a different creep behaviour. In short, compliance of samples loaded at various maturity is fitted using the same Kelvin-Voigt chain with ageing springs. The results will then be used in an autogenous shrinkage model, in an attempt to test the superposition principle on LC³ materials in next Chapter.

Experimental procedure

Two sets of samples were cast using the protocol described in 3.2.1. The first set of samples was used to determine the strength at loading age. Samples were loaded after 20h, 42h, 3d, 14d and 28d of hydration at 15% of their strength. Load duration was 48h, 6d, 19d, 28d and 28d, respectively. Data was processed as described earlier, then fit with the ageing rheological model. Processed compliance is plot on Figure 3.35. The odd behaviour of the samples loaded at early age can be explained with the two following reasons. The strength of the material at loading age was quite low, as the pozzolanic reaction of metakaolin need about 3 days to start. Hence the creep load was quite moderate at the beginning of the test. The material getting stronger quickly over a short time, the initial load is not causing a very important creep strain. If we then add to this situation the important autogenous shrinkage occurring between 3 and 5 days of hydration (see Chapter 4), the calculated creep strain could reach a temporary plateau, or even an "expansion" because of the data processing.

Numerical method

A Kelvin-Voigt (K-V) rheological unit is composed of a spring and a dashpot or damper and is adapted to model visco-elastic, reversible materials. In such a unit both elements undergo the same strain, but not the same stress. Only two parameters are required to define a K-V unit: stiffness E [MPa] of the spring and viscosity η [Pa.s] of the dashpot. Both quantities are related through the characteristic time τ of the dashpot:

$$\tau = \frac{E}{\eta} \quad (3.8)$$

The following constitutive equations govern the unit:

$$\varepsilon_{tot} = \varepsilon_S = \varepsilon_D \quad (3.9)$$

$$\sigma_{tot} = \sigma_S + \sigma_D \quad (3.10)$$

$$\sigma_{tot}(t) = E\varepsilon(t) + \eta \frac{d\varepsilon(t)}{dt} \quad (3.11)$$

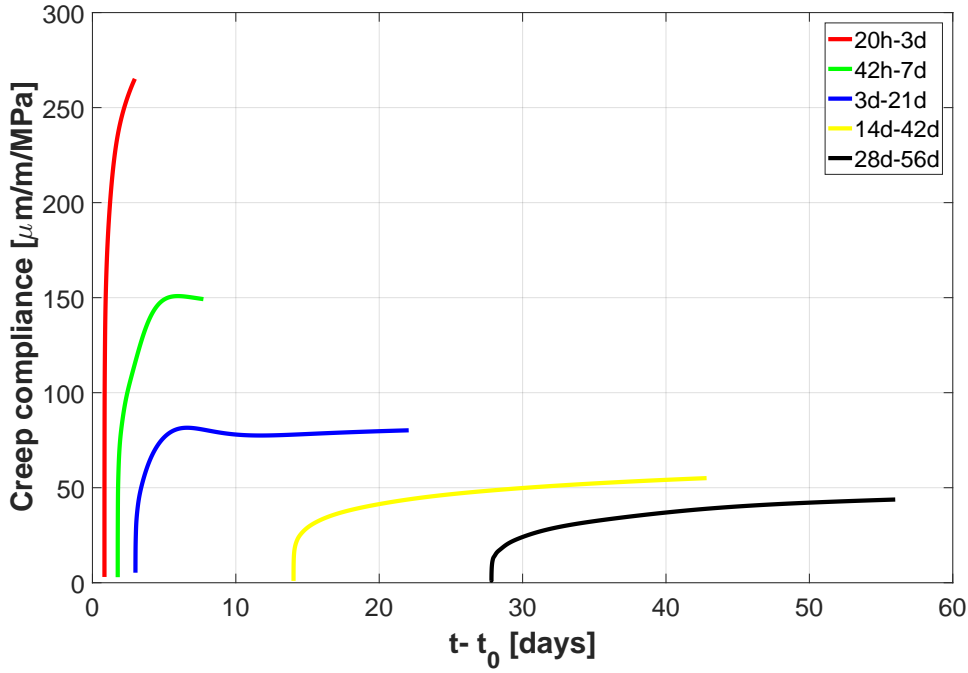


Figure 3.35 – This plot summarizes the compressive creep compliance of the LC³-50 45% mix at different loading ages. Curvature changes appear when the shrinkage rate is faster than the creep rate.

with subscript *S* to indicate the spring and *D* the damper.

The deformation rate is then defined by the following set of equations, using dot notation to denote the time derivative:

$$\dot{\epsilon} = \frac{\dot{\sigma}_{tot} - \dot{\sigma}_D}{E} \quad (3.12)$$

$$\dot{\epsilon} = \frac{\sigma_D}{\eta} \quad (3.13)$$

In our case and unlike [27], four of these units instead of three were concatenated to form a generalized Kelvin-Voigt model, without the additional dashpot, as represented in Figure 3.36. For the time window being considered in this study, experience showed that using a fourth Kelvin-Voigt unit instead of an extra, non-ageing dashpot provided a better fit of the results, at the expense of more adjustment of the coefficients. This model being phenomenological, the stiffness and characteristic time of the unit are not linked to microstructural features, although no correlation were investigated in this research. To take ageing into account, stiffness of the springs — and therefore viscosity of the dashpots — depends on the degree of hydration of the material. The problem is discretized over time and equations 3.12 and 3.13 can be rearranged to obtain the following second-order differential equation, for each of the Kelvin-Voigt units *i*

of the chain:

$$\frac{\dot{\sigma}_i}{E_i(t)} = \tau_i \cdot \ddot{\epsilon}_i + \left(1 + \frac{\dot{E}_i(t)}{E_i(t)} \cdot \tau_i\right) \cdot \dot{\epsilon}_i \quad (3.14)$$

which is solved according to the method presented in [25] and [27].

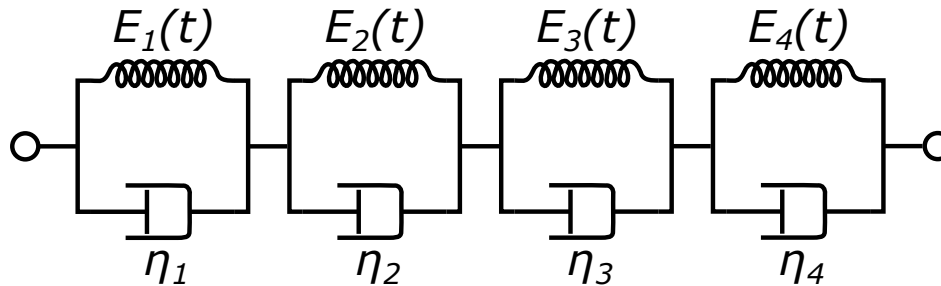


Figure 3.36 – A four-unit Kelvin-Voigt rheological model with ageing springs was used to model ageing creep.

The characteristic times of the dashpots were set to 0.01, 0.2, 3 and 30 days. The rule of thumb used to fix these times was to have the shortest time similar to the sampling interval and the longest time on the order of the total duration of the experiment. An order of magnitude separates the duration of each characteristic time. The ageing function for the springs stiffness was a power function of the degree of hydration. The stiffness of the springs was considered to be constant after 28 days and therefore adjusted to fit the data from the last test correctly. Coefficients of the power function were selected to minimize the difference between the model and the experimental data at different loading ages. Figure 3.37 shows the evolution over time of the springs' stiffness and sums up the properties of the K-V units. Figure 3.38 shows the results of the fitting for the various loading ages. The results are satisfactory. A better fit could probably be achieved using different functions for ageing, but could require more arbitrary parameters to be adjusted. This result will serve as a base for the autogenous shrinkage modelling in the next chapter.

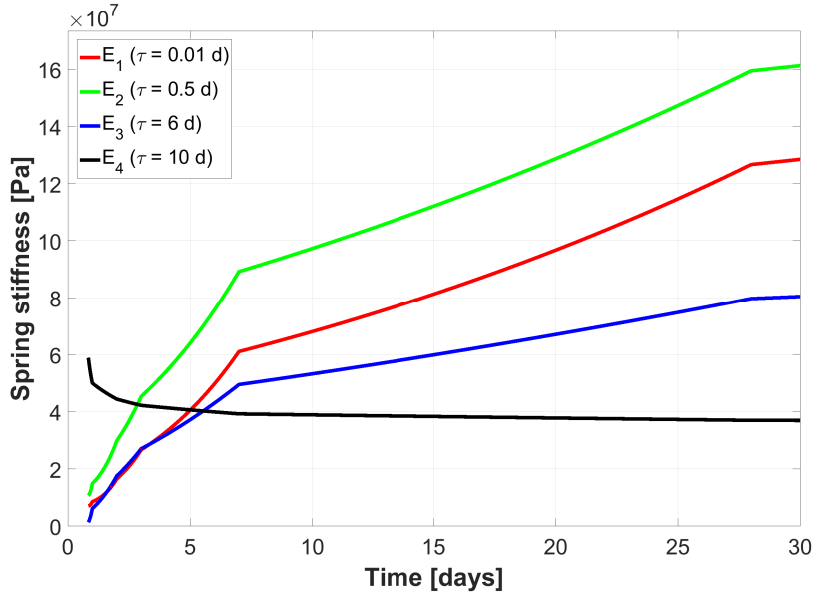


Figure 3.37 – This plot shows the evolution over time of the stiffness of the springs from each K-V unit. Time is actually related to degree of hydration. The characteristic time associated to each K-V unit is also shown on the plot. In this model, the units having the shortest times harden faster.

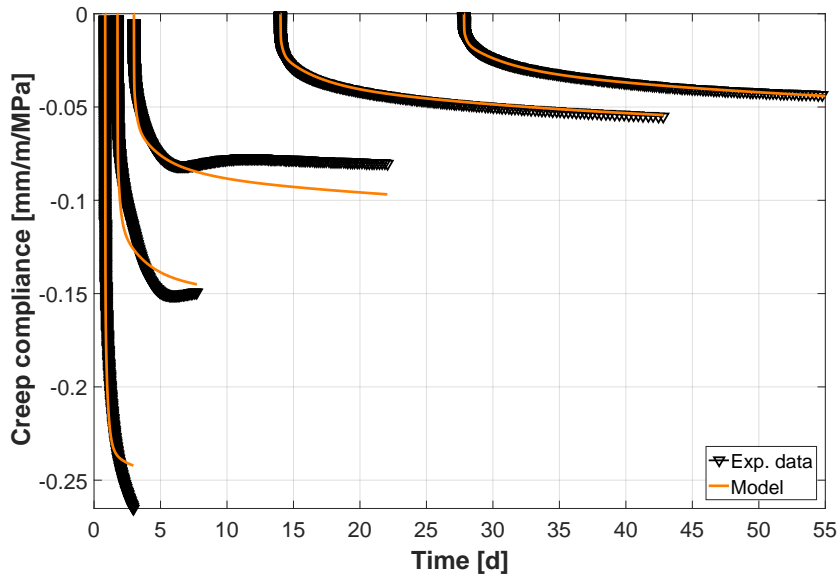


Figure 3.38 – This figure shows the output of the rheological model, fitting the same material with an ageing generalized Kelvin-Voigt model composed of four units.

3.5 Conclusions

This chapter deals with the experimental results of basic creep on mature paste samples of plain cement and LC³. The slight evolution of Young's modulus over the creep test period, coupled with the slow changes in saturation level and metakaolin reaction degree (see section 2.3 and next Chapter) indicate that the microstructure was not completely mature at the moment of loading (28 days after mixing). Nevertheless, fitting the kinetics with non-ageing power or logarithmic functions produced good results over the test period, as well as using a rheological model independent from the degree of hydration in the 2D-FEM approach. A first qualitative assessment of the data indicated a lower compliance for the ternary blends. The extent of this reduction is not dependent on the calcined kaolinite content of the clay if it is above about 40%, and a noticeable compliance reduction in mature samples was observed with a clay containing only 25% of metakaolin.

A first comparison of the creep results and the microstructure indicated that the reduction of compliance could be linked to a lower C–S–H content in LC³. An investigation on the compliance kinetics was then carried out. The main conclusion was that all creep curves could be fitted with a power law with a similar exponent. This could indicate that similar mechanisms are at work in spite of the very heterogeneous microstructures. The results of the mass balance calculation (Chapter 2) indicated that after 28 days of hydration, LC³-50 mixes containing at least 10 to 12% of metakaolin would have a similar microstructure in terms of amount of anhydrous phases, portlandite and C–S–H. This threshold value corresponds to the amount of metakaolin required to consume the accessible portlandite produced by clinker hydration, which reaches a similar level in all LC³-50 samples at a W/B of 0.4. This is a clue indicating that all the clayey phases, including inert phases or unreacted metakaolin, and the carboaluminates typical of LC³ can be considered as elastic phases, as their proportions varied but the viscous response was similar among the samples. Specifically, their volume amount can double between the lowest or highest grade clays and the middle grade clays, which give rise to the highest amount of carboaluminates in the microstructure.

The studied LC³ mixes contained a higher amount of silicon and aluminium in their C–S–H thanks to the contribution of metakaolin. The Al/Ca ratio is dependent on the clay grade, as well as the Si/Ca to a lower extent, therefore a correlation exists between a threshold Al/Ca or Si/Ca ratio in the C–S–H and a lower compliance of the material. However, the present study does not permit us to prove any causation between these quantities. A recent study from Wilson *et al.* [62] pointed out a slight link between the aluminium content of the C–S–H matrix and the contact creep modulus obtained by nano-indentation, see Figure 3.39. Nevertheless, as the addition of SCMs generally lowers creep compliance, brings aluminium and silicon to the system and affects the microstructure at the same time, the available data does not allow to quantify the contribution of C–S–H chemistry on its viscous behaviour, if any.

To further investigate the dissimilarities, a 2D finite elements model was used to simulate creep *via* a two-scale model. The larger scale considered the C–S–H matrix containing

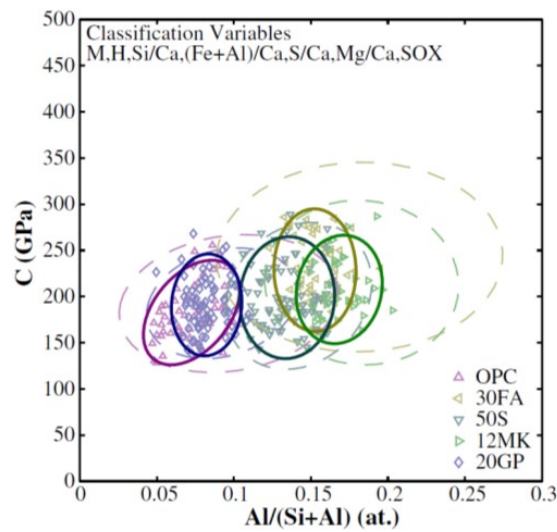


Figure 3.39 – This figure, adapted from 3.39, compares the contact creep modulus, back-calculated from a statistical analysis of nano-indentation and SEM-EDS data, to the aluminium content of the probes volume. The use of various SCM added aluminium to the matrix and slightly decreased the contact creep modulus.

solid inclusions of anhydrous and hydrated phases as a continuous medium. The visco-elastic properties of the matrix were adjusted so that the simulation results fell close to the experimental data. The second scale used an analytical, poro-mechanical approach to take the porosity of the matrix into account and estimate the mechanical properties of the C–S–H gel alone. The output of the simulations pointed towards a less compliant C–S–H in the LC³, with a similar viscous behaviour among all the samples containing limestone and calcined clay, including model clays or very low grade clays with coarser porosity (see Figure 2.3). The model also indicated that despite having more C–S–H in their microstructure and with a similar microscopic compliance, the white cements being studied had a similar macroscopic compliance because of the difference in porosity in the C–S–H matrix.

As the model considers C–S–H gel as a whole, it cannot explain the exact mechanisms at the origin of the decrease of compliance. In light of what was measured and modelled, some of the following causes could explain the observations:

- As reported in [35], aluminium present in the pore solution is likely to be taken up by C–S–H at the silicon bridging sites, increasing the amount of cross-linking in the nanostructure. A contribution of this polymerisation to the compliance reduction — be it through a reinforcement of C–S–H or a hindrance of movement of water — cannot be excluded. However, recent results from Hu *et al.* [28], using the same poro-mechanical approach as the present study, found no major difference in the compliance of C–S–H gel of a plain cement and a binary cement-fly ash mix. Although having a slow reaction rate, fly ashes bring aluminium and silicon to the pore solution, ultimately affecting the

C–S–H composition. This suggests that the chemistry of C–S–H has not a main role in its viscous properties.

- As observed by Avet [2], the proportion of outer to inner C–S–H product is higher in LC³ than plain cement, indicating that the C–S–H gel is likely to be more intermixed with dispersed filler particles and hydrates present in LC³. Specifically, thin clay platelets could physically limit the viscous flow of the material. This effect was observed in polymers reinforced with graphene [14], although creep mechanisms are different. The mere filler effect of limestone and clay could also provide more interfacial surface between the variety of hydrates formed in LC³ and a finer phase mixing. In their recent study, Wyrzykowski *et al.* [64] observed a very different creep behaviour between their real and equivalent systems. One of the microstructural disparities between these mixes is the proportion of outer and inner product. Their conclusions could not confirm or exclude a contribution of this factor.
- Vandamme and Ulm [57] reported a decrease of C–S–H compliance with better packing. A concept of packing is applicable in their reasoning because they adopted a colloidal representation of C–S–H gel. However, Avet reported a very similar average density between LC³-50 binders and plain cement. A denser C–S–H alone could not explain all the compliance variation.
- LC³ materials are reported to have a similar amount of porosity to equivalent W/B plain cement paste, but with a much finer pore structure [49]. The analytical approach used to obtain the C–S–H gel properties only considers capillary and air pores and is not adapted to a finely dispersed porosity. At any rate, the purpose of this approach was to evaluate the properties of the gel, which included its intrinsic porosity and the potential effect it can have on viscosity. Furthermore, in a recent publication from Avet *et al.* [2], it was demonstrated using ¹H-NMR that the gel to interlayer water ratio was similar in plain cement paste and LC³-50 prepared with the same cement, indicating a similar C–S–H structure between LC³ and plain cement. The change in gel compliance cannot be attributed to a different water repartition within the C–S–H structure.

Some further investigation will be required to estimate the potential occurrence and impact on compliance of the discussed phenomena. This discussion is carried out in the last chapter of this thesis.

3.6 References

- [1] Paul Acker and Franz-Josef Ulm. “Creep and shrinkage of concrete: physical origins and practical measurements”. *Nuclear Engineering and Design* 203.2 (Jan. 2001), pp. 143–158.
- [2] François Avet, Emmanuelle Boehm-Courjault, and Karen Scrivener. “Investigation of C-A-S-H composition, morphology and density in Limestone Calcined Clay Cement (LC3)”. *Cement and Concrete Research* 115 (Jan. 2019), pp. 70–79.
- [3] Véronique Baroghel-Bouny. “Caractérisation microstructurale et hydrique des pâtes de ciment et des bétons ordinaires et à très hautes performances”. PhD thesis. Laboratoire Central des Ponts et Chaussées, 1994.
- [4] Arpita Pal Bathija. “Elastic properties of clays”. en (), p. 129.
- [5] Bažant Zdeněk P. and Chern Jenn-Chuan. “Triple Power Law for Concrete Creep”. *Journal of Engineering Mechanics* 111.1 (Jan. 1985), pp. 63–83.
- [6] Z. P. Bažant. “Constitutive equation for concrete creep and shrinkage based on thermodynamics of multiphase systems”. en. *Matériaux et constructions* 3.1 (Jan. 1970), pp. 3–36.
- [7] Z. P. Bažant. “Theory of Creep and Shrinkage in Concrete Structures : A · Precis of Recent Developments”.
- [8] Z. P. Bažant. “Thermodynamics of interacting continua with surfaces and creep analysis of concrete structures”. *Nuclear Engineering and Design* 20.2 (July 1972), pp. 477–505.
- [9] Z. P. Bazant and J. C. Chern. “Concrete creep at variable humidity: constitutive law and mechanism”. en. *Materials and Structures* 18.1 (Jan. 1985), pp. 1–20.
- [10] Z. P. Bažant and E. Osman. “Double power law for basic creep of concrete”. en. *Matériaux et Construction* 9.1 (Jan. 1976), pp. 3–11.
- [11] Zdenek P Bazant and Jenn Chuan Chern. “Log Double Power Law for Concrete Creep”. English (US). *Journal of the American Concrete Institute* 82.5 (Sept. 1985), pp. 665–675.
- [12] Zdenek P Bazant and Folker H Wittmann. “Creep and shrinkage in concrete structures” (1982).
- [13] V. Belov and P. Kuliaev. “Limestone filler as one of the cheapest and best additive to concrete”. Vol. 365. 2018.
- [14] A. Bhattacharyya. “Graphene reinforced ultra high molecular weight polyethylene with improved tensile strength and creep resistance properties”. *Express Polymer Letters* 8.2 (Dec. 2013), pp. 74–84.
- [15] Ludwig Boltzmann. “Zur Theorie der elastischen Nachwirkung”. de. *Annalen der Physik* 241.11 (1878), pp. 430–432.
- [16] J. J Brooks and M. A Megat Johari. “Effect of metakaolin on creep and shrinkage of concrete”. *Cement and Concrete Composites*. Metakaolin and Calcined Clays 23.6 (Dec. 2001), pp. 495–502.

- [17] Georgios Constantinides and Franz-Josef Ulm. “The effect of two types of C-S-H on the elasticity of cement-based materials: Results from nanoindentation and micromechanical modeling”. *Cement and Concrete Research* 34.1 (Jan. 2004), pp. 67–80.
- [18] Zhuo Dai, Thuan T. Tran, and Jørgen Skibsted. “Aluminum Incorporation in the C–S–H Phase of White Portland Cement–Metakaolin Blends Studied by ^{27}Al and ^{29}Si MAS NMR Spectroscopy”. en. *Journal of the American Ceramic Society* 97.8 (Aug. 2014), pp. 2662–2671.
- [19] B. Delsaute, J. -M. Torrenti, and S. Staquet. “Modeling basic creep of concrete since setting time”. *Cement and Concrete Composites* 83 (Oct. 2017), pp. 239–250.
- [20] Brice Delsaute, Claude Boulay, and Stéphanie Staquet. “Creep testing of concrete since setting time by means of permanent and repeated minute-long loadings”. *Cement and Concrete Composites* 73 (Oct. 2016), pp. 75–88.
- [21] R. F. Feldman. “Mechanism of creep of hydrated portland cement paste”. *Cement and Concrete Research* 2.5 (Sept. 1972), pp. 521–540.
- [22] Alain Benjamin Giorla. “Modelling of Alkali-Silica Reaction under Multi-Axial Load”. en. PhD thesis.
- [23] Zhi-hai He et al. “Creep behavior of concrete containing glass powder”. *Composites Part B: Engineering* 166 (June 2019), pp. 13–20.
- [24] Zhihai He et al. “Creep analysis of concrete with different mineral admixtures”. en. *Materials Express* 6.4 (Aug. 2016), pp. 328–336.
- [25] Adrien Hilaire et al. “Modeling basic creep in concrete at early-age under compressive and tensile loading”. *Nuclear Engineering and Design*. Special Issue - The International Conference on Structural Mechanics in Reactor Technology (SMiRT21), New Delhi India, Nov 06-11, 2011 269 (Apr. 2014), pp. 222–230.
- [26] M Hlobil, V Šmilauer, and G Chanvillard. “Multiscale micromechanical damage model for compressive strength based on cement paste microstructure”. In: *CONCREEP 10*. 2015, pp. 1211–1218.
- [27] Zhangli Hu. “Prediction of autogenous shrinkage in fly ash blended cement systems” (2017), p. 213.
- [28] Zhangli Hu et al. “Intrinsic viscoelasticity of C-S-H assessed from basic creep of cement pastes”. *Cement and Concrete Research* 121 (July 2019), pp. 11–20.
- [29] M. Irfan-ul-Hassan et al. “Elastic and creep properties of young cement paste, as determined from hourly repeated minute-long quasi-static tests”. *Cement and Concrete Research* 82 (Apr. 2016), pp. 36–49.
- [30] Fu Jia et al. “Nano-scale modeling and elastic properties of a typical CSH (I) structure based on DFT and Molecular Dynamics Methods”. en (2015), p. 9.
- [31] M. Jirásek and P. Havlásek. “Microprestress–solidification theory of concrete creep: Reformulation and improvement”. *Cement and Concrete Research* 60 (June 2014), pp. 51–62.

- [32] Königsberger Markus et al. “Downscaling Based Identification of Nonaging Power-Law Creep of Cement Hydrates”. *Journal of Engineering Mechanics* 142.12 (Dec. 2016), p. 04016106.
- [33] R. Le Roy, F. Le Maou, and J. M. Torrenti. “Long term basic creep behavior of high performance concrete: data and modelling”. en. *Materials and Structures* 50.1 (Oct. 2016), p. 85.
- [34] Jianyong Li and Yan Yao. “A study on creep and drying shrinkage of high performance concrete”. *Cement and Concrete Research* 31.8 (Aug. 2001), pp. 1203–1206.
- [35] Barbara Lothenbach and André Nonat. “Calcium silicate hydrates: Solid and liquid phase composition”. *Cement and Concrete Research*. Keynote papers from 14th International Congress on the Chemistry of Cement (ICCC 2015) 78 (Dec. 2015), pp. 57–70.
- [36] Barbara Lothenbach et al. “Influence of limestone on the hydration of Portland cements”. *Cement and Concrete Research* 38.6 (2008), pp. 848–860.
- [37] Thomas Matschei, B Lothenbach, and Fredrik P Glasser. “The role of calcium carbonate in cement hydration”. *Cement and Concrete Research* 37.4 (2007), pp. 551–558.
- [38] J. Moon et al. “First-principles elasticity of monocarboaluminate hydrates”. en. *American Mineralogist* 99.7 (July 2014), pp. 1360–1368.
- [39] Harald S. Müller et al. “Concrete: treatment of types and properties in fib Model Code 2010”. en. *Structural Concrete* 14.4 (2013), pp. 320–334.
- [40] Adam M Neville. “Creep of plain and structural concrete” (1983).
- [41] Edgar Alejandro Pachon-Rodriguez et al. “Wet creep of hardened hydraulic cements — Example of gypsum plaster and implication for hydrated Portland cement”. *Cement and Concrete Research* 63 (Sept. 2014), pp. 67–74.
- [42] Jean Péra, Sophie Husson, and Bernard Guilhot. “Influence of finely ground limestone on cement hydration”. *Cement and Concrete Composites*. Portland Limestone Cements 21.2 (1999), pp. 99–105.
- [43] G. Pons and J.-M. Torrenti. “Retrait et fluage”. In: *La durabilité des bétons*. Presse des ponts, 2008.
- [44] T. C. Powers. “The thermodynamics of volume change and creep”. en. *Matériaux et Construction* 1.6 (Nov. 1968), pp. 487–507.
- [45] A. P. Roberts and E. J. Garboczi. “Computation of the Linear Elastic Properties of Random Porous Materials with a Wide Variety of Microstructure”. en. *Proceedings: Mathematical, Physical and Engineering Sciences* 458.202 (2002).
- [46] Pierre Rossi, JL Tailhan, and F Le Maou. “Creep strain versus residual strain of a concrete loaded under various levels of compressive stress”. *Cement and concrete research* 51 (2013), pp. 32–37.

-
- [47] Robert Le Roy. “Déformations instantanées et différées des bétons à hautes performances”. fr. PhD thesis. Ecole Nationale des Ponts et Chaussées, Sept. 1995.
- [48] Walter Ruetz. “A hypothesis for the creep of hardened cement paste and the influence of simultaneous shrinkage”. *Proceedings of the Structure of Concrete and its Behavior under Load* (1968), pp. 365–387.
- [49] Karen Scrivener et al. “Calcined clay limestone cements (LC3)”. *Cement and Concrete Research*. Report of UNEP SBCI WORKING GROUP ON LOW-CO2 ECO-EFFICIENT CEMENT-BASED MATERIALS 114 (Dec. 2018), pp. 49–56.
- [50] Shahidi M., Pichler B., and Hellmich Ch. “Interfacial Micromechanics Assessment of Classical Rheological Models. I: Single Interface Size and Viscosity”. *Journal of Engineering Mechanics* 142.3 (Mar. 2016), p. 04015092.
- [51] Shahidi M., Pichler B., and Hellmich Ch. “Interfacial Micromechanics Assessment of Classical Rheological Models. II: Multiple Interface Sizes and Viscosities”. *Journal of Engineering Mechanics* 142.3 (Mar. 2016), p. 04015093.
- [52] T. C. Powers and T. L. Brownnyard. “Studies of the Physical Properties of Hardened Portland Cement Paste”. *Journal Proceedings* 43.9 (Jan. 1946).
- [53] Basile T. Tamtsia, James J. Beaudoin, and Jacques Marchand. “The early age short-term creep of hardening cement paste: load-induced hydration effects”. *Cement and Concrete Composites*. Early Age Concrete - Properties and Performance 26.5 (July 2004), pp. 481–489.
- [54] Basile T Tamtsia and James J Beaudoin. “Basic creep of hardened cement paste A re-examination of the role of water”. *Cement and Concrete Research* 30.9 (Sept. 2000), pp. 1465–1475.
- [55] Jeffrey J. Thomas and Hamlin M. Jennings. “A colloidal interpretation of chemical aging of the C-S-H gel and its effects on the properties of cement paste”. *Cement and Concrete Research* 36.1 (Jan. 2006), pp. 30–38.
- [56] jean michel Torrenti and Robert Le Roy. “Analysis and Modelling of Basic Creep”. Sept. 2015.
- [57] M. Vandamme and F. -J. Ulm. “Nanoindentation investigation of creep properties of calcium silicate hydrates”. *Cement and Concrete Research* 52 (Oct. 2013), pp. 38–52.
- [58] M. Vandamme and F.-J. Ulm. “Nanogranular origin of concrete creep”. en. *Proceedings of the National Academy of Sciences* 106.26 (June 2009), pp. 10552–10557.
- [59] Karine Velez et al. “Determination by nanoindentation of elastic modulus and hardness of pure constituents of Portland cement clinker”. *Cement and Concrete Research* 31.4 (Apr. 2001), pp. 555–561.
- [60] Vito Volterra. *Theory of functionals and of integral and integro-differential equations*. 1930.

Chapter 3. Basic creep on mature paste samples

- [61] Y. H. Wang, Y. D. Xu, and Z. H. He. “Effect of limestone powder on creep of high-strength concrete”. *Materials Research Innovations* 19 (2015), pp. 220–223. eprint: <https://doi.org/10.1179/1432891715Z.0000000001969>.
- [62] William Wilson, Luca Sorelli, and Arezki Tagnit-Hamou. “Unveiling micro-chemo-mechanical properties of C-(A)-S-H and other phases in blended-cement pastes”. *Cement and Concrete Research* 107 (May 2018), pp. 317–336.
- [63] F. H. Wittmann. “Interaction of Hardened Cement Paste and Water”. en. *Journal of the American Ceramic Society* 56.8 (1973), pp. 409–415.
- [64] Mateusz Wyrzykowski, Karen Scrivener, and Pietro Lura. “Basic creep of cement paste at early age - the role of cement hydration”. *Cement and Concrete Research* 116 (Feb. 2019), pp. 191–201.
- [65] Hailong Ye. “Creep Mechanisms of Calcium–Silicate–Hydrate: An Overview of Recent Advances and Challenges”. en. *International Journal of Concrete Structures and Materials* 9.4 (Nov. 2015), pp. 453–462.
- [66] Qing Zhang et al. “Long-term creep properties of cementitious materials: Comparing microindentation testing with macroscopic uniaxial compressive testing”. *Cement and Concrete Research* 58 (Apr. 2014), pp. 89–98.

4 Autogenous shrinkage

This chapter first presents the theoretical background required to understand the phenomenon of autogenous shrinkage in cementitious materials and summarizes the experimental techniques available to measure this deformation and their limitations. Then the experimental results are presented for the materials being studied and interpreted thanks to complementary input data. Lastly, a poro-visco-elastic model is applied to an LC³ material as an attempt to model autogenous shrinkage as a combination of elastic and viscous strains.

Contents

4.1 Literature review	79
4.1.1 Shrinkage mechanisms	79
4.1.2 Measurement methods	82
4.1.3 Autogenous shrinkage modelling	84
4.2 Experimental methods	89
4.2.1 Autogenous shrinkage measurement	89
4.2.2 Relative humidity	90
4.3 Experimental results	91
4.3.1 Influence of cement type	91
4.3.2 Influence of initial water content	94
4.3.3 Natural calcined clays	96
4.3.4 Model clays	99
4.3.5 Average pore pressure	101
4.4 Shrinkage and microstructure evolution	102
4.5 Modelling	105
4.5.1 Numerical scheme	105
4.5.2 Inputs of the model	105
4.5.3 Model output and discussion	110
4.6 Conclusions	112

Chapter 4. Autogenous shrinkage

4.7 References 113

4.1 Literature review

The phenomenon of autogenous shrinkage of cement has been known for more than a century; a direct consequence of the chemical shrinkage observed by Le Chatelier. This strain can reach a considerable amplitude in mixes at low W/C, such as HPC. Contrary to drying shrinkage, autogenous shrinkage is induced only by the consumption of free water through hydration reactions, and not by water lost to the environment. Similar to basic creep, autogenous shrinkage will occur in all situations, as it is a direct consequence of the evolving microstructure during hydration. As mitigation techniques are limited and expensive for autogenous shrinkage, it is of great interest to characterize this phenomenon in order to adapt the mix design to the situation.

4.1.1 Shrinkage mechanisms

There are many theories which try to explain the mechanisms of autogenous shrinkage in cementitious materials. These have a common basis: self-desiccation through hydration. During hydration, the final volume of the products is lower than the initial volume of the anhydrous phases and free water. This simply comes from the fact that liquid water has a larger molar volume than water in hydrated compounds. This difference in volume is called *chemical shrinkage*. Before setting, the macroscopic shrinkage is similar to this chemical shrinkage as the system is not yet rigid enough to sustain any load. As soon as the cement sets (from the point where the solid phases percolate), the macroscopic shrinkage is restrained and chemical shrinkage will lead to the apparition of a gas phase (water vapour) in the liquid phase inside the capillary pores, to accommodate the volume change. As hydration goes on, these gas pockets grow larger and the RH in the gas phase decreases: *self-desiccation* happens. In the case of low W/C, relative humidity can reach values around of 80%, before the cement hydration becomes limited due to lack of moisture [35]. The interface between the gas, solid and liquid phases is where forces appear, causing macroscopic autogenous shrinkage. In the next section, the main theories explaining the origin of the shrinkage forces are discussed.

Surface tension

Any free solid or liquid surface possesses free energy and surface tension [27]. In solids, surface energy can be interpreted as the work required to create a new surface by division of the bulk material. Surface tension is the tangential stress that acts to bring the surface to a configuration that is more stable thermodynamically. It is either balanced by external forces or volume stresses in the material. As for liquids, it is expressed in force per unit length. Adsorption of liquid molecules on a solid surface lowers its surface tension and could therefore cause an expansion of the solid; removal of the adsorbed molecules should cause a shrinkage. Following their observations of charcoal swelling with water vapour and supposing surface tension was governing the phenomenon as in gels, Bangham and Fakhoury [5], [6] proposed a

Chapter 4. Autogenous shrinkage

simple equation linking changes in dimension to variations of surface tension:

$$\frac{\Delta l}{l} = \lambda \cdot \Delta\gamma \quad (4.1)$$

where l [m] is the length, Δl [m] the length change, $\Delta\gamma$ [N/m] the change in surface tension of the solid particles, and λ [s²/kg] a coefficient of proportionality. This initially empirical coefficient was later developed by Hiller [15], as depending on the internal surface Σ and elastic modulus E of the porous body and the density of the solid ρ_S :

$$\lambda = \frac{\Sigma \cdot \rho_S}{3 \cdot E} \quad (4.2)$$

with Σ in [m²/kg], ρ_S in [kg/m³] and E in [MPa].

This mechanism is not considered as the main actor in autogenous shrinkage for two main reasons. Firstly, as this force acts only on the solid particles, it cannot account for the whole deformation of the porous body [24] and secondly, the decrease in surface tension is important only for the two first adsorbed layers. It has been shown, thanks to BET isotherm measurements, that a monolayer of water molecules would be completed around 12% RH on a cementitious material and a double layer around 50% RH. Self-desiccation can only drive RH down to about 80% RH at most. After this point, hydration reactions stop and moisture is stable [35]. Hence the motive not to consider surface tension as the main shrinkage mechanism in autogenous conditions.

Disjoining pressure

Whenever two solid surfaces are very close to each other and liquid is adsorbed, the formation of a free adsorbed liquid layer pushes the surfaces apart. This force is called *disjoining pressure* and is regarded as a potential driver to autogenous shrinkage. Disjoining pressure acts in regions of hindered absorption, where solid surfaces are separated by a distance shorter than the thickness of a couple of adsorbed liquid layers. Experiments from Ferraris [12] and Beltzung [8], illustrated the presence of such a force by measuring the force acting between

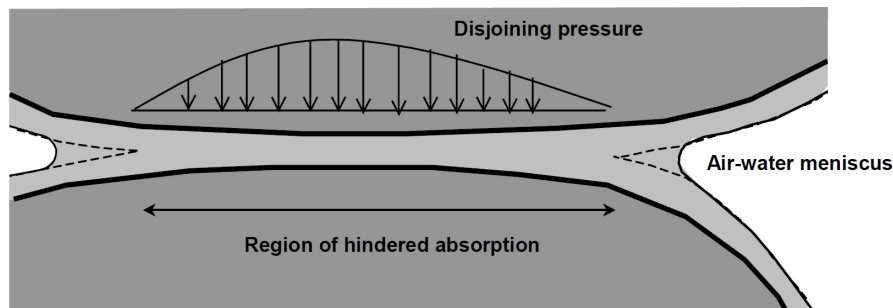


Figure 4.1 – This schematic from [28] represents the region of hindered adsorption in between two solid surfaces, where disjoining pressure is exerted.

two very close quartz surfaces and varying relative humidity. The set-up measured the appearance of a repulsive force above about 55% RH. They attributed this phenomenon to the disjoining pressure overcoming the attractive Van der Waals force between the solids. The main argument against disjoining pressure being the main reason for autogenous shrinkage is that, although varying sharply between 50% and 75% RH, it is constant above 80% RH, in the self-desiccation range. Disjoining pressure has a magnitude reported to be of some MPa in cementitious materials [8], and also to be dependent on the concentration of Ca⁺ ions. However, disjoining pressure could be regarded as one of the main driving force in drying shrinkage, as drying, even in natural conditions, can drive internal relative humidity of cement well below 70% RH.

Capillary pressure

The most accepted driving force for autogenous shrinkage is the capillary pressure. Whenever an interface between a solid, a liquid and a gas (or a second liquid immiscible with the first one) is created, the equilibrium geometry will be defined by their relative surface tensions. These quantities are related to each other by the Young equation, which also defines the contact angle at the gas-liquid interface. When confined between solid surfaces, such as in a capillary, the equilibrium shape of the interface is a meniscus. Menisci are accompanied with a pressure differential across the gas-liquid interface. Its amplitude and direction (tensile or compressive) are given by the Young-Laplace equation:

$$P_c = P_g - P_l = -\frac{2\gamma_l \cdot \cos(\theta)}{r} \quad (4.3)$$

where P_c [Pa] is the capillary pressure, P_l [Pa] the pressure in the gas phase, P_l [Pa] the pressure in the liquid phase, γ_l [N/m] and θ_l are the surface tension and contact angle of the liquid-gas interface, respectively, and r [m] is the curvature radius of the meniscus. The Kelvin equation describes the relation between the curvature of a liquid-gas interface and the relative vapour pressure:

$$\ln\left(\frac{p}{p_0}\right) = \ln(RH) = \frac{2\gamma V_m}{rRT} \quad (4.4)$$

where p [Pa] is the vapour pressure, p_0 [Pa] is the saturated vapour pressure, γ [N/m] is the surface tension, V_m [m³/mol] is the molar volume of the liquid, R is the universal gas constant (8.314 J · mol⁻¹ · K⁻¹), r [m] is the radius of the droplet, and T [K] is temperature. Eq. 4.3 and 4.4 can be combined into the Kelvin-Laplace equation to obtain the capillary pressure only knowing partial pressure and molar volume of the liquid. In the case of water, partial pressure is translated to relative humidity:

$$P_c = \frac{R \cdot T}{V_m} \cdot \ln(RH) \quad (4.5)$$

with $V_m = 18 \text{ cm}^3/\text{mol}$ for pure water at 20°C.

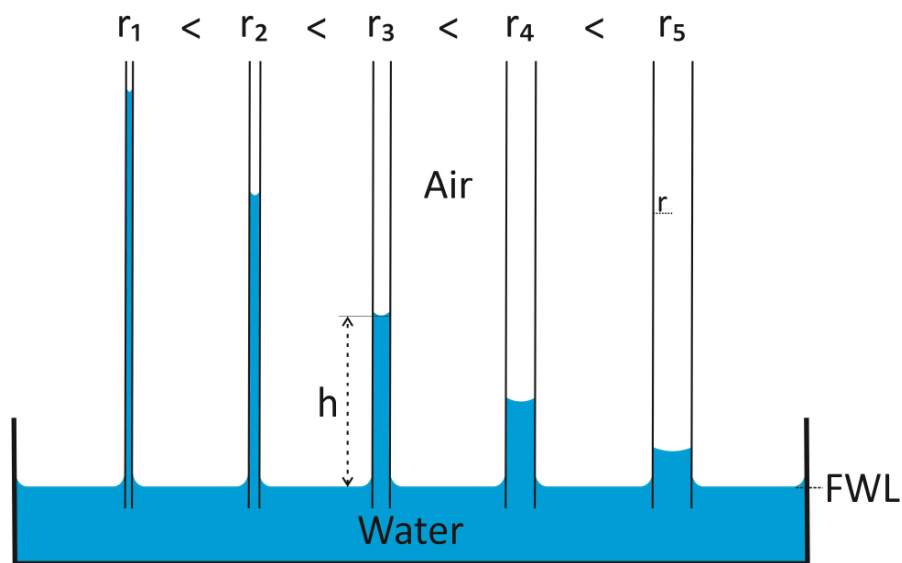


Figure 4.2 – This schematic from [22] illustrates the effect of increasing radius on the capillary pressure. For vertical capillaries, the equilibrium height of the liquid corresponds to the balance between capillary pressure and gravitational pull.

4.1.2 Measurement methods

There are several methods proposed to measure autogenous shrinkage of cement paste, mortar or concrete. They all involve having the sample sealed from ambient air and kept at constant temperature, to avoid drying shrinkage and thermal expansion. This section briefly summarizes the main techniques, separated into volumetric and linear methods, along with their advantages and limitations. A more detailed review is available in [26].

Volumetric methods

A widespread method based on measuring the volume change associated with autogenous shrinkage is the *membrane method*. It was first described by Yates [37]. It consists in pouring freshly mixed cement paste into a thin, flexible plastic membrane and immersing it into a controlled temperature water or oil bath. Underwater weight is then monitored with a set of scales, and the weight change over time can be linked to the volume of the sample thanks to Archimedes' principle. If it looks like a simple enough method in theory, many hurdles appear when applied. First, one has to make sure that the membrane is completely inert chemically (dissolution) and physically (permeation, swelling) to the surrounding liquid and the sample over extended periods of time. Any amount of liquid traversing the membrane would lead to a considerable reading error over the duration of the experiment. In addition, the accuracy of the balance, including all the potential sources of noise such as turbulences in the bath, may limit the resolution. Lastly, as each sample requires its own high-precision balance, it limits the possibilities of running many samples in parallel. Due to all these limitations, it was not used in this study.

Linear methods

There are several standardized methods for autogenous shrinkage based on linear measurements, effectively measuring the strain along a single axis of the specimen. The ASTM C157 [1] is the simplest method, as it only requires to measure strain along the longest dimension of a sample, using a LDVT or a similar device. This standard requires the specimen to be kept in a lime-saturated solution for the duration of the test. This is not exactly a sealed condition, as water can go from the solution to the samples, preventing the desaturation of a part of the porosity and allow extended hydration. A simple improvement of this method is to seal the samples in a plastic or aluminium wrapping to prevent drying, while keeping them at constant temperature. The main drawback of ASTM C157 is that the measurements can only be made on an hardened samples, 24h after casting. It possible to start the measurement earlier on younger samples, but there is a higher risk of damaging the sample, or drying it, during the demolding process. Moreover, as a considerable part of the shrinkage can happen during the first day of hydration, this method may miss a large part of the strain. A first improvement of this method was proposed by the *Japanese Concrete Institute* [30]. In essence, it consists of casting the sample in a mold lined with a polyester or Teflon film, together with gauge plugs to allow strain measurement. Shrinkage is then measured *via* LVDTs placed at the exterior of the mold, using two transducers for each sample. This allows many replicas with limited equipment. The polymer films should allow both sealing of the samples and low friction movement of the specimen inside the mold. In practice, these features are difficult to ensure for the whole duration of the experiment.

The corrugated tubes method, which is the main method used in this research, is described in ASTM C1698-09 [9] and can be seen as a further improvement over the JCI set-up. In that case, cement paste is cast into corrugated polyethylene tubes. The specific design of the tubes allows the specimen to shrink freely along the longitudinal axis. The original standard proposes to keep the samples in a room with controlled temperature and to carry out the length measurement manually on a specific bench. A single bench is required, even when having many experiments running in parallel — thus lowering the cost of the whole set-up — but every manipulation of the samples comes with a risk of damaging them. Some changes can be made to the standard to obtain more accurate results and limit the interactions between the operator and the samples. For instance, keeping the samples in a temperature controlled oil bath ensures a better diffusion of heat from hydration, minimizing thermal expansion during the first days of hydration [36]. Submersible LVDTs can be used to monitor the length of the tubes automatically without removing them from the bath. If one end of the tube is fixed, then a single transducer per tube is sufficient to monitor shrinkage. The special shape of the plastic molds creates very low friction between them and the steel parts of the bench, with very limited contact area and an oily medium for lubrication. As the tubes are sealed and placed on the bench right after filling, this modified set-up allows early strain measurements, as early as 30 min after mixing.

Time-zero

A critical point when it comes to interpreting readings from autogenous shrinkage is the question of reference time, or *time-zero*. This is the transition moment when the material is able to withstand the volume change from chemical shrinkage. It is generally agreed upon that a solid skeleton is necessary for the apparition of menisci in the pore network. Solid percolation does not necessarily correspond to the setting time, as percolation can occur quite early, but the material may still have a low rigidity. Shrinkage can be preceded by a period of expansion. In this study, the choice was made to use the local maximum of this expansion as time-zero. That way, mixes are compared based on their monotonous shrinkage behaviour. This choice has no impact for the creep processing results and makes comparison with the model simpler.

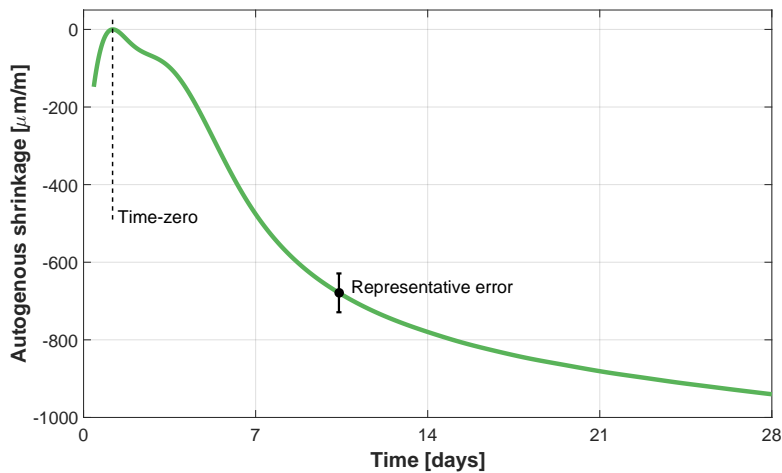


Figure 4.3 – This illustrative plot shows the position of the time-zero at the local maximum after starting the measurement. All studied samples show an amount of chemical shrinkage before the expansion, which was captured by the set-up but remove from the plots for better readability.

4.1.3 Autogenous shrinkage modelling

Modelling of autogenous shrinkage of hydrating cementitious material as been — and still is — a considerable challenge in the field. The main difficulty lies in modelling the physical properties and behaviour of a partially saturated porous material whose microstructure is evolving with time. Autogenous shrinkage models can be separated into two distinct categories, depending on how they tackle the problem. *Empirical models* use a statistical approach over many mix designs to create models tailored to specific situations, whereas *mechanistic models* try to predict the shrinkage forces and their consequence based on characteristics of the microstructure, such as mix design and degree of hydration.

Empirical approaches

The basic principle of the empirical approaches is to aggregate enough experimental data from distinct and well characterized mix designs in order to constrain a phenomenological model. These models are generally quite efficient at predicting the strain of mixtures close to those forming the database. For instance, Tazawa *et al.* [29] proposed a prediction model for cement paste based on the degree of reaction of the clinker mineral phases. Although being quite reliable within the intended composition domain, this model will lose its accuracy when the mix design is not close to the input data. Later on, many technical committees proposed alternative models to predict autogenous shrinkage based on inputs accessible on the work site [10], [31]. The B4 model [34] also uses an empirical approach to predict shrinkage over long periods of time. However, it requires six coefficients to be adjusted from experimental data.

Another category of phenomenological models are those derived from machine learning algorithms [21], [18], [25]. In essence, they are quite similar to statistical models, but thanks to an ever increasing computing power and large amount of data, such algorithms are able to analyse very large datasets. The main drawbacks of this approach are the amount of fitting parameters and their unclear links with mix design, and the limited capabilities of predicting situations outside the algorithm's training range.

Mechanistic approaches

The approach selected for this study is based on a mechanistic model. Such models generally start with estimating the driving force of shrinkage resulting from capillary pressure (in the case of autogenous shrinkage), then compute the strain associated to that force on the cementitious matrix. Two main approaches can be identified to estimate the pore fluid pressure: those based on relative humidity and the Kelvin-Laplace equation, and those based on the Kelvin radius and the Young-Laplace equation.

Assessing the internal relative humidity of the porosity is usually achieved by placing a humidity probe in a small, sealed cell containing cement paste [19]. The assumption is made that the air surrounding the sample quickly equilibrates with the internal humidity of the sample. The measured moisture is the combination of the RH drop caused by the menisci formation and the change in water activity due to dissolved ions. In cementitious materials, dissolved ions have a low but constant contribution to the measured relative humidity, and can be easily accounted for using Raoult's law. This approach was selected for this study, as it allows a continuous monitoring of the internal RH of hydrating samples. The conversion from capillary stress to macroscopic strain also needs a specific approach. A majority of the mechanistic models adopted equations from poromechanics, as a partially saturated media well describes hardened cement paste. Simple models only consider shrinkage as a poro-elastic strain and more complex ones also include a viscous term to account for creep caused by the shrinkage forces.

Porosity-elasticity

The equations of poromechanics, derived from Hooke's law, describe the linear deformation ε of an isotropic porous body subject to some pressure P [Pa] as follow:

$$\varepsilon_l = -\frac{1}{3} \cdot P \cdot \frac{b}{K} \quad (4.6)$$

where K [Pa] is the bulk modulus of the porous body and b the Biot coefficient, defined as $1 - K/K_s$, with K_s the bulk modulus of the solid material without porosity.

The value for capillary pressure is correct for a single cylindrical capillary, but in the case of a porous material, it depends on the pore distribution. Indeed, low RH implies high capillary pressure, but if only a small part of the pore population lies at the threshold radius, the effective stress on the material will be low. The ratio between the capillary pressure and the effective pore stress is called the *Bishop's parameter* χ . It represents the surface ratio on which pore pressure can apply. The difficulty of directly accessing this parameter means that it is often estimated from other accessible quantities. In many models, the saturation level of the porosity S is used to approach χ . The main motivation to do so is the ease of access to saturation degree and the equal value of S and χ at full and zero saturation. There is no proof that both quantities are linearly correlated and this point is questioned [13]. However, for the desaturation range attainable in self-desiccation conditions, both parameters will be considered equivalent in this study. The product of capillary pressure and saturation level is called the *average pore pressure* and is used as the driving force for shrinkage. This value combined to 4.6 gives the *Biot-Bishop equation*:

$$\varepsilon_l = -\frac{1}{3} \cdot (P_c \cdot S) \cdot \left(\frac{1}{K} - \frac{1}{K_s} \right) \quad (4.7)$$

Bulk modulus K can be obtained from Young's modulus and Poisson's ratio:

$$K = \frac{E}{3 \cdot (1 - 2\nu)} \quad (4.8)$$

The aforementioned saturation level or degree S is conventionally defined as the ratio of evaporable water over the total pore volume. Evaporable water is comprised of capillary water, gel water and interlayer water; total pore volume include air voids from chemical shrinkage on top of that. The total amount of evaporable water can be obtained through destructive methods such as TGA or desorption (for mature samples) or with a mass balance calculation. The latter method is used in this study.

It is worth mentioning that the Biot-Bishop approach on strain of partially saturated porous media is not the only one that was proposed. For instance, Coussy suggested an alternative definition of the driving force, including the gas-liquid-solid interface energy in the calculation [11]. Later, Vlahinić introduced a dependency of the solid bulk modulus on the saturation level to account for the softening of the bulk properties when converting clinker

to hydrates [33]. Neither of these alternative approaches give significantly differing results in the range of relative humidity and saturation level reached in sealed conditions [16], but they would be meaningful in drying conditions. Therefore the Biot-Bishop method was adopted in this research.

Poro-visco-elasticity

Most studies indicate that considering autogenous only as a poro-elastic phenomenon systematically underestimated the calculated strain after some days of hydration [19]. It is suggested that this discrepancy is due to viscous flow caused by creep under the sustained shrinkage stresses. Considering the still limited understanding of creep mechanisms, most shrinkage models including creep express it in an empirical way. Autogenous shrinkage happens over a range of degree of hydration where visco-elastic properties of the material are expected to change substantially. To take this ageing into account, some authors used power or logarithmic laws with time or degree of hydration dependent coefficients [17], or rheological models with ageing components. Certain FE models take ageing of C-S-H into account [23]. Considering the relatively short time scale studied here, an approach similar to Biot-Bishop equation was adopted. Calculation of the equivalent "viscous bulk modulus" is carried out using creep compliance and a viscous Poisson's ratio. As both compliance and average pore pressure depend on time, the total viscous strain has to be integrated over a time interval.

$$\varepsilon_v(t) = \int_{t_0}^t \left\{ (1 - 2 \cdot \nu_v(t)) \cdot \frac{\partial J(t, \tau)}{\partial t} dt - \frac{1}{3K_s} \right\} \cdot \frac{d\sigma}{d\tau} d\tau \quad (4.9)$$

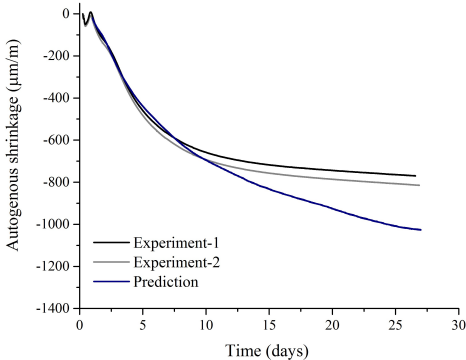
Considering that $\sigma = P_c \cdot S$, Eq. 4.9 becomes

$$\varepsilon_v(t) = \int_{t_0}^t \left\{ (1 - 2 \cdot \nu_v(t)) \cdot \frac{\partial J(t, \tau)}{\partial t} dt - \frac{1}{3K_s} \right\} \cdot \left(\frac{dP}{d\tau} \cdot S + P \cdot \frac{dS}{d\tau} \right) d\tau \quad (4.10)$$

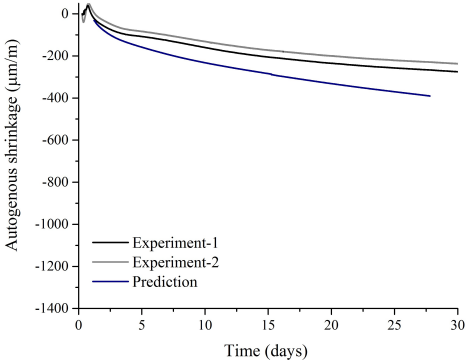
with ν_v [-] the viscous Poisson's ratio, $J(t, \tau)$ [Pa^{-1}] the uniaxial basic creep compliance function of the material, depending on the current time t [d] and the loading age τ . The analogy with the Biot-Bishop equation can be seen in the left part of the term in the curly brackets as being the viscous bulk modulus of the macroscopic porous material.

This approach was used in Hu's thesis, which is the basis used in this work. Her results, summarized on Figure 4.4 showed that this method gave a reasonable estimation of the autogenous shrinkage, based on the aforementioned hypothesis. The particular viscous behaviour of LC^3 binders offers the occasion to test this approach on materials with a different rheology.

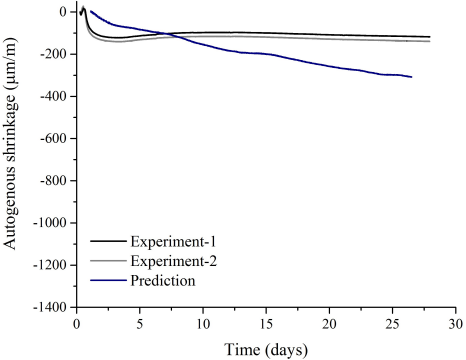
Chapter 4. Autogenous shrinkage



(a) PC-0.35



(b) CFA40-0.35



(c) CQZ40-0.35

Figure 4.4 – These plots from [16] show the output of the poro-visco-elastic model versus the experimental data, for a) plain cement, b) cement with 40% fly ash and c) cement with 40% quartz. All mixes were prepared at a W/B of 0.35.

4.2 Experimental methods

4.2.1 Autogenous shrinkage measurement

Autogenous shrinkage measurements were carried out according to ASTM C1698-09, using a silicon oil bath for controlling temperature and submersible LVDTs for continuous monitoring. Before each run of experiments, a part of the sealing plugs was prepared to be the fixed end of the sample: a hole was drilled halfway through the plug, from the external side, then threaded at M5. A prepared plug was placed at the end of the tube and sealed with instant glue. A volume of about 700 mL was then prepared using a vacuum mixer at a mixing speed of 450 rpm for 2 min. The mix was then carefully poured into a tube held in a vertical position with a steel tube or a specifically designed plastic holder. The operation is carried out on a vibrating table to ensure proper flow of the paste. The tube is then sealed with a pristine plug, weighted and placed on the bench in the silicone oil bath. One end of the tube is fixed to the bench thanks to the thread. A submersible LVDT is placed at the free end. Automatic logging is achieved thanks to an autonomous logger. Most measurements started between 30 and 60 min after mixing. All mixes are replicated twice or thrice and showed little deviation within a given mix.

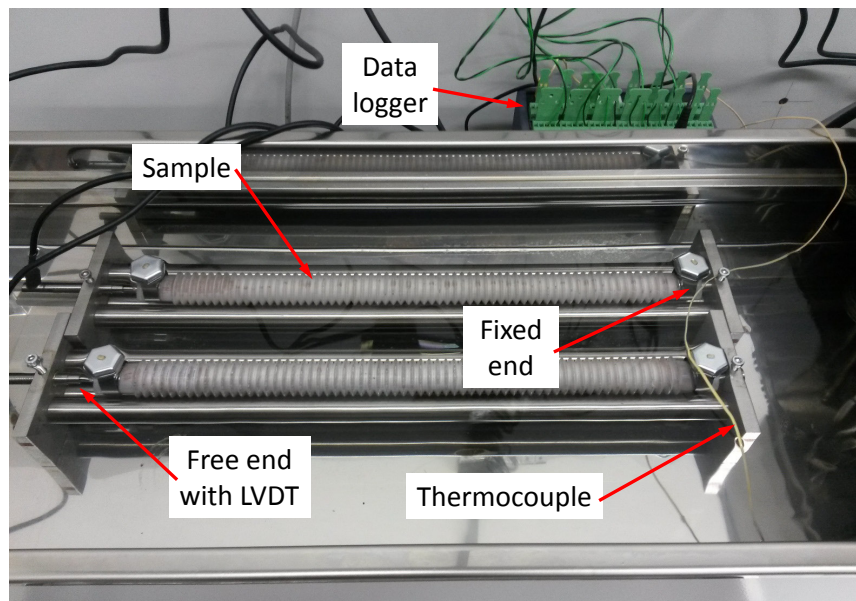


Figure 4.5 – This picture shows the corrugated tube set-up. Cement paste was mixed and immediately cast into two corrugated tubes and placed in the oil bath. The steel bench holding the tube also serves to fix one of its ends and to hold the LVDT in place. The external logger is also used to monitor the bath temperature. A later design of the bench allowed to place 6 tubes in parallel.

4.2.2 Relative humidity

As discussed, the capillary pressure is function of the relative humidity through the Kelvin-Laplace equation (Eq. 4.5). The relative humidity of the paste samples was monitored using HC2-AW-USB water activity probes from *Rotronic*. The probes measure the RH of the air surrounding the sample. Due to the limited size of the chamber, it is assumed that the RH of the air is at equilibrium with that of the pore network. A water cooling system kept the samples and the sensor at a constant temperature of 20°C. In a time range between 16h and 24h after casting, samples to be tested are crushed to sub-centimetre pieces and placed in the device, in a plastic container fitting the cavity. The set-up is equipped with 3 cells, and every mix was replicated on the 3 cells in parallel. The reading interval was set to 5 min during the first 5 to 7 days of hydration, and then reduced to one reading per hour. A calibration routine is carried out in-between each run, using the built-in software calibration tool (*HW4 v.3*). Saturated solutions of different salts (K_2SO_4 , K_2NO_3 , KCl, NaCl) were used to calibrate the sensors at fixed RH points between 98% and 75%. When measuring RH, the obtained reading actually is a combination of the RH drop caused by the desaturation of the pores (RH_K) and the water activity of the pore solution (RH_S), which is linked to the amount and species of ions dissolved. According to the results from [16] (Chapter 3), water activity only slightly decreases during the first month after hydration, and in a similar fashion for PC or blended cements. When required, (RH_S) was approximated by the following function:

$$RH_S(t) = 0.9872 - 0.0025 \cdot \ln(t) \quad (4.11)$$

with time t expressed in days.

4.3 Experimental results

This section presents all the experimental results of autogenous shrinkage on the mixes introduced in Chapter 2.

4.3.1 Influence of cement type

Figure 4.6 shows the evolution of autogenous shrinkage during the two first months of hydration for a series of samples with different cements. All cements used show a qualitatively similar behaviour: an initial expansion, followed by a sharp shrinkage and a stabilization. The maximum expansion (time zero) takes place after 24h of hydration for the LabCement and the Normo 4, but as soon as 12h for the white cement. The higher fineness of the white cement is likely to be the cause of the faster initial kinetics, combined with the lower W/C.

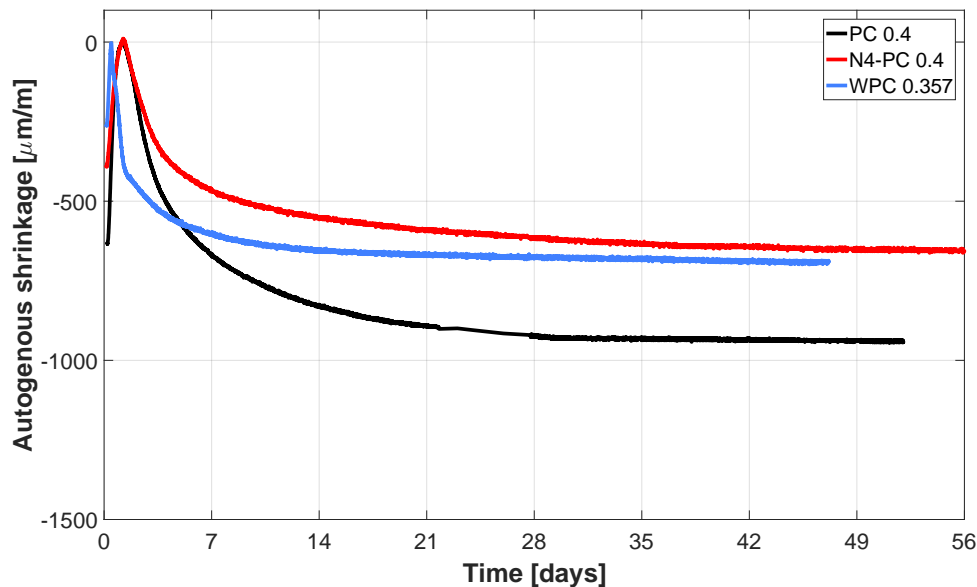


Figure 4.6 – Autogenous shrinkage of plain cement paste for 56 days of hydration.

Figure 4.7 compares shrinkage of plain cement and LC³ mixes prepared with two different cements (LabCement in 4.7a and Normo 4 in 4.7b) during the first 28 days. As observed in Figure 4.6, the plain cement has a different shrinkage behaviour, but in the ternary blends, the effect of the replacement material is similar between both cements. Compared to the behaviour of plain cement, the LC³-50 mixes with the 45% clay show a delay of the shrinkage. This is an expected feature of the clinker dilution effect when using SCM. Indeed, as the replacement materials are not as reactive as cement, clinker phases are the only ones reacting during the first days. As LC³-50 only contains about half of fast-reacting material by mass, a larger amount of water is available, porosity remains saturated and relative humidity stays elevated, causing low shrinkage at an early stage. On the other hand, both mixes with

Chapter 4. Autogenous shrinkage

high-grade metakaolin (MQ95) only show a very limited initial expansion, followed by a short shrinkage period with a timing and rate close to that of cement. A very stable plateau appears after about 5 days of hydration. Calorimetry (see Avet's thesis [2]) and MIP (see Chapter 2) also confirm the slowing down of reaction and quick refining and stabilization of microstructure during the first days of hydration.

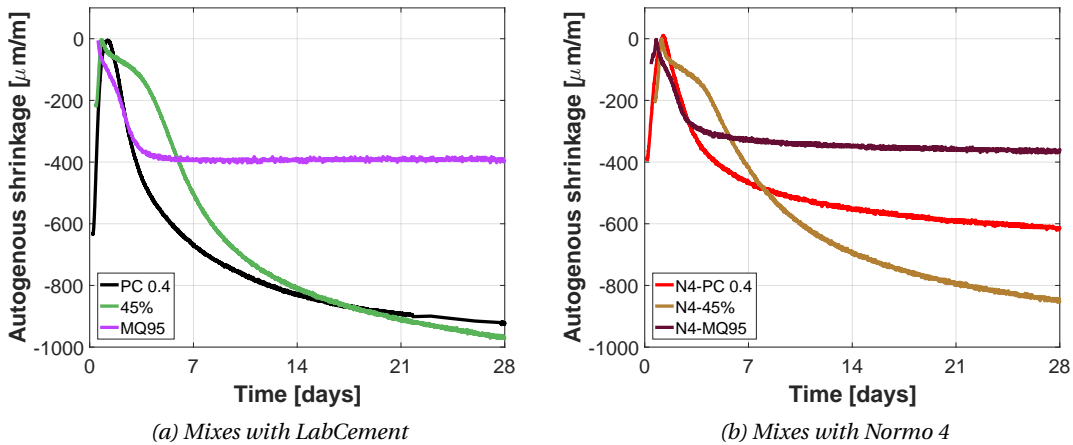


Figure 4.7 – Comparison of autogenous shrinkage during the 28 days of hydration for a plain cement, an LC^3 with a natural clay and an LC^3 with a model clay.

Figure 4.8 shows the shrinkage of the same mixes up to 56 days. The delaying effect is very consistent between mixtures using the 45% clay, and the fast stabilisation of the MQ95 mixes has a very similar duration as well. Similar to the behaviour of the plain cement sample, LC^3 with Normo 4 show a slightly lower shrinkage than mixes using LabCement.

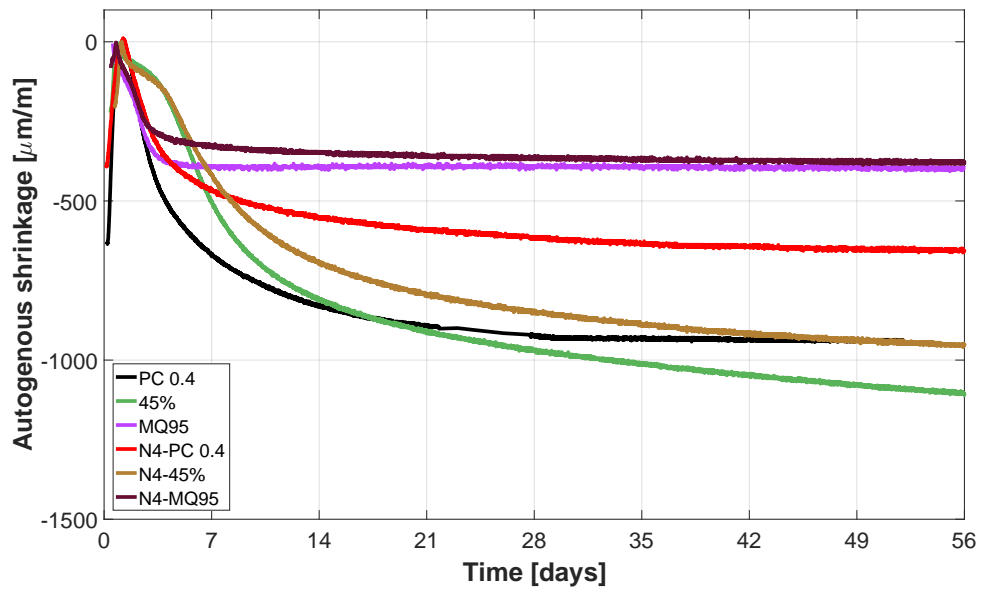


Figure 4.8 – Autogenous shrinkage of LC^3 -50 and plain cement samples with comparable mix designs. The initial trend of cement powder is preserved to the blends.

4.3.2 Influence of initial water content

Figure 4.9 compares the results for cement and LC³ mixes prepared with different initial water contents (see Table 4.1). In both plain cement and LC³, a decrease of the W/B increases the shrinkage, but has no noticeable effect on the time-zero. A diminution of shrinkage with more initial water is in accordance with the theories on autogenous shrinkage. In LC³ in particular, the initial shrinkage delay is prolonged when W/B is increased.

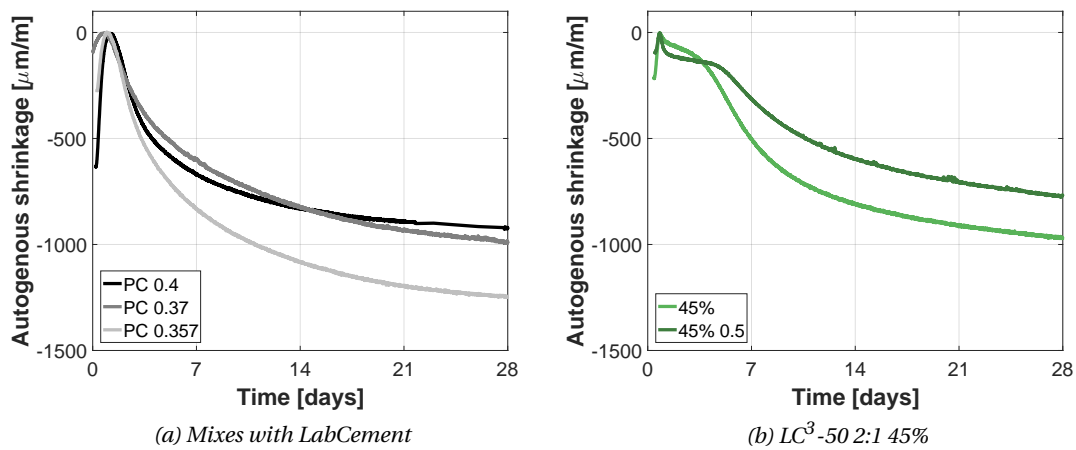


Figure 4.9 – Autogenous shrinkage during 28 days for mixes with different initial water content. a) Mixes using LabCement b) LC³-50 2:1 with the same cement and 45% clay.

Table 4.1 – Summary of the mix designs used to evaluate the effect of initial water. Water content expressed in ml/l.

	PC 0.4	PC 0.37	PC 0.357	45% 0.4	45% 0.5
W/C	0.4	0.37	0.357	0.4	0.5
W/S	1.32	1.23	1.18	1.18	1.46
Water cont.	567	548	539	539	594

Figure 4.10 summarizes these results up to 56 days of hydration. For these mixes using the LabCement, LC³ shows lower shrinkage than plain cement at equivalent W/S.

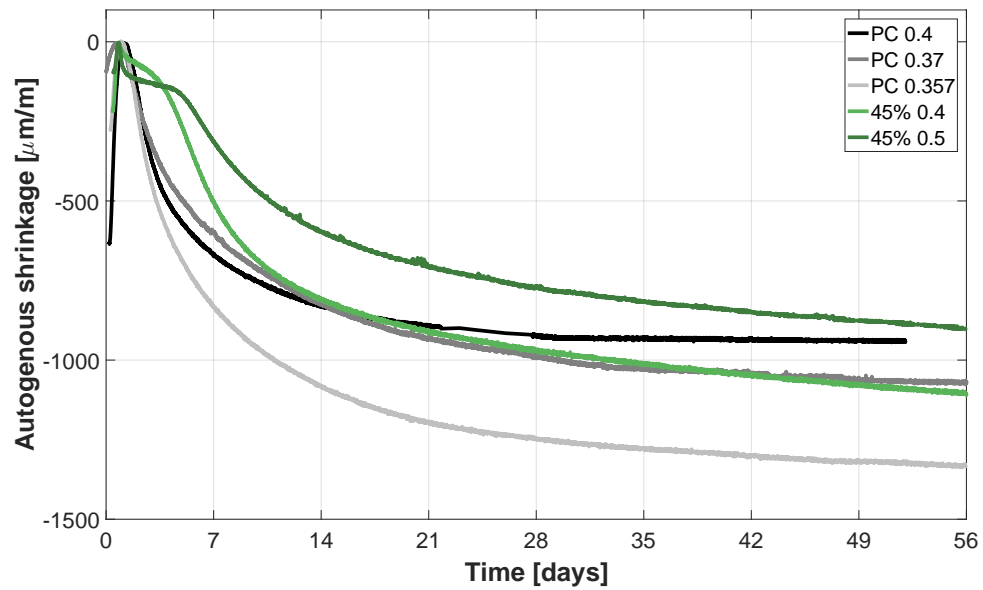


Figure 4.10 – Autogenous shrinkage of samples with varying water content. An increased amount of mixing water reduces the total shrinkage amplitude and the retardation effect and amplified in LC^3 .

4.3.3 Natural calcined clays

Figure 4.11 shows the evolution of autogenous shrinkage over time for the subset of samples prepared with calcined natural clays with a kaolinite content ranging from 15% to 60% and mix design LC³-50 2:1, W/B of 0.4. All samples showed a variable amount of swelling during the first day, before reaching a monotonous shrinkage regime. It is worth noticing that the swelling amplitude is dependent on the calcined kaolinite content of the clay. Higher grade clays mitigate this initial expansion more. A delay of the onset of shrinkage can be observed on all the ternary blends compared to the plain cement reference. The first acceleration of the strain occurs 3 to 4 days after casting for this set of LC³ blends, versus 1 to 2 days for the plain cement sample. As discussed previously, this is an expected consequence of diluting the cement with slower reacting powders.

In the longer term, all the LC³ samples except the 15% fall into a quite a narrow region of the graph. In spite of a varying clay grade, both kinetics and total amplitude remain similar among the samples, which indicates that similar shrinkage forces are acting on microstructures of comparable stiffness. The system with the lowest grade clay shows only a very modest shrinkage, possibly an indication of a high relative humidity in the pore network. The delay is also visible on the RH evolution, see Figure 4.13. The overall trend of internal relative humidity closely follows that of shrinkage.

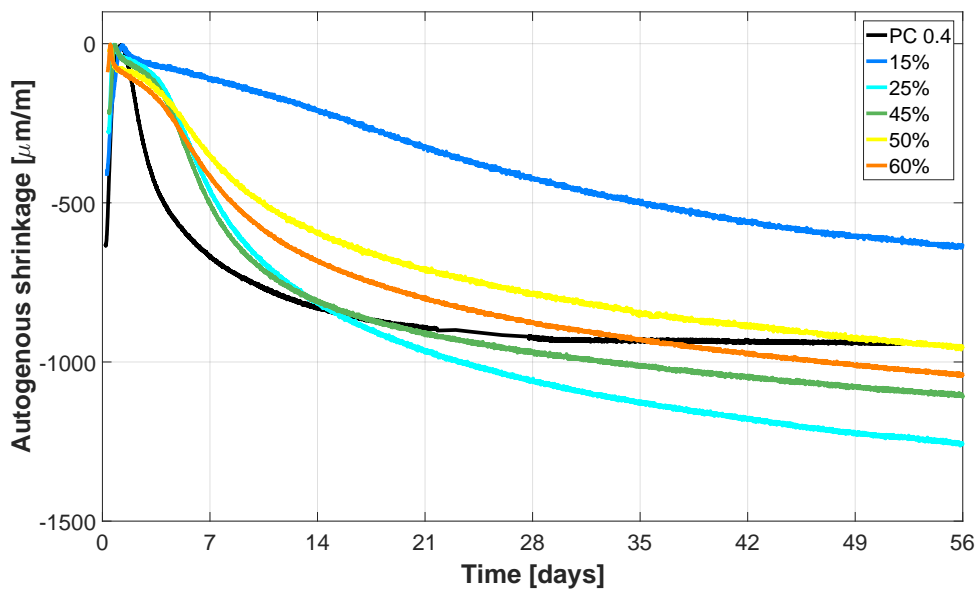


Figure 4.11 – Autogenous shrinkage of LC³-50 samples with natural clays compared to a same W/B cement mix. The delay caused by the dilution effect is clearly visible at the beginning of the measurement. Clays above 25% of kaolinite content have a comparable effect on autogenous shrinkage.

4.3. Experimental results

Figure 4.12 aggregates results for LC³-50 and LC³-65 mixes prepared with the 45% clay and a calcined clay to limestone ratio of 2 or 1. Firstly, the effect of the limestone addition on shrinkage is negligible. This is in accordance with the results of the previous figure, showing the low dependence of kaolinite content on autogenous shrinkage. This shows that blending calcined clay with limestone is equivalent as using a lower grade clay, regarding shrinkage behaviour. The initial delay is shorter in LC³-65 due to the lower clinker replacement fraction. For the LC³-65 mix design, the samples show about 40% more shrinkage than the plain cement reference after 2 months of hydration. The reason for a higher shrinkage has to be the result of the slightly lower Young's modulus and a higher amplitude of the driving force, as LC³ materials show a lower creep compliance. This is supported by the RH measurements reported in Figure 4.13, where the moisture level of the LC³-65 sample reaches a lower level than the PC 0.4.

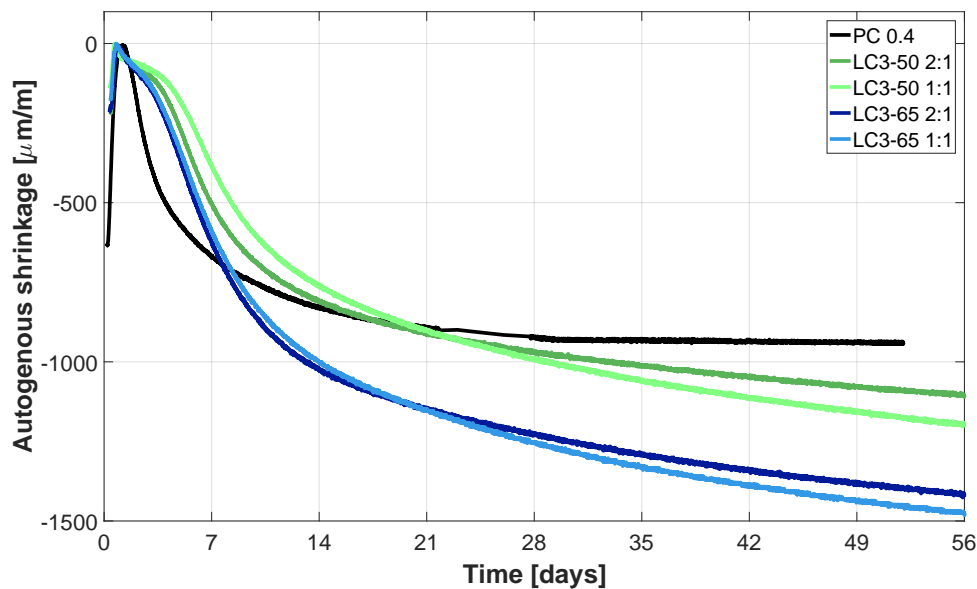


Figure 4.12 – Autogenous shrinkage during 56 days of LC³-50 and LC³-65 samples with varying clay content. The same clay at 45% of kaolinite content is used for all LC³. The calcined clay to limestone ratio is variable.

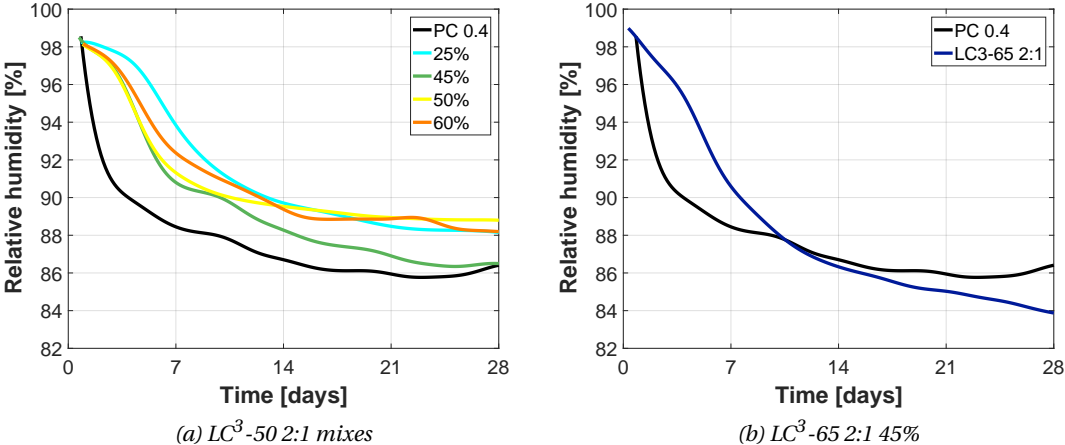


Figure 4.13 – Internal relative humidity evolution of LC^3 -50 (a) and LC^3 -65 (b) mixes compared to PC 0.4. The initial delay from clinker dilution is clearly visible in the RH evolution.

4.3.4 Model clays

The results concerning the mixes prepared using model clays are presented on Figures 4.14 and 4.16. Model clays are mixtures of industrial grade, flash-calcined metakaolin and quartz powder. For instance, MQ45 stands for a mixture of 45% metakaolin and 55% quartz. Figure 4.14a compares two LC³ with model clays to a plain cement and an LC³ with natural clay. In contrast to basic creep, it appears that model systems are not able to reproduce the behaviour of natural calcined clays. Both mixes with model clay quickly shrink during the first week of hydration and then show very low or no evolution, whereas the LC³ with a natural clay of equivalent metakaolin content shows a progressive shrinkage for at least 28 days. This feature is also clearly visible in the evolution of internal relative humidity, Figure 4.15. A delay of shrinkage is observed in the MQ45 sample, but not as long as with the natural clay.

Figure 4.14b shows the results of LC³ using model clays and white cement. All LC³ samples exhibit the distinctive delay. The evolution of the W-MQ60 and W-MQ80 samples is similar, but the W-MQ40 shows a different progression. The shrinkage of an LC³-50 with a natural 60% clay, but a different cement is also plotted on this graph. Its behaviour is very close to that of the W-MQ40. This indicates that a MQ60-type is not able to capture the behaviour of and equivalent natural clay, but a MQ40-type mix can efficiently mimic a mix with a 45% to 60% kaolinite natural clay. A reason might be a better availability of the metakaolin in the case of the model clay, but evidence is lacking to confirm this supposition.

Lastly, Figure 4.16 shows the shrinkage evolution up to 56 days for the discussed samples using model clays. The main observations are that the behaviour of the first month represents well the later trends as well, and that the W-MQ40 and LC³-50 with a natural 60% clay continue to have a very similar shrinkage.

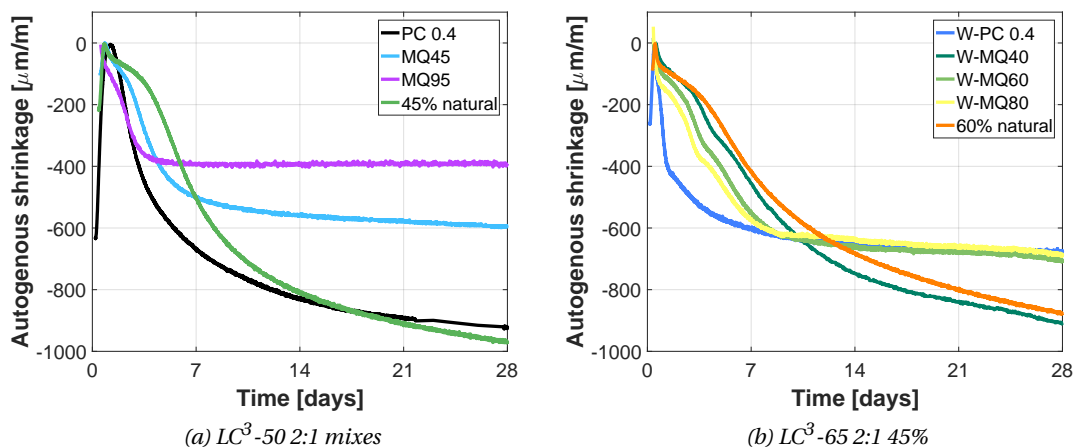


Figure 4.14 – Autogenous shrinkage during 28 days for mixes with model clays, using (a) LabCement or (b) white cement, compared to an LC³ with natural clay and the LabCement. Model clays are not able to emulate the behaviour of natural clays with the same kaolinite content, but it seems that a low grade model clays can mimic a higher grade natural clay.

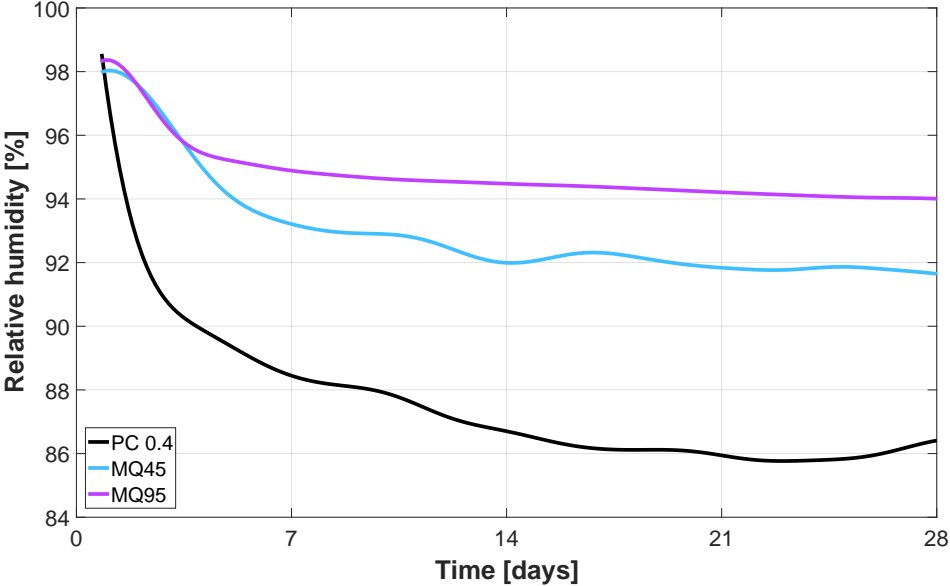


Figure 4.15 – Internal relative humidity during 28 days for the model clay systems. The stabilisation of shrinkage coincides with a stabilisation of the relative humidity.

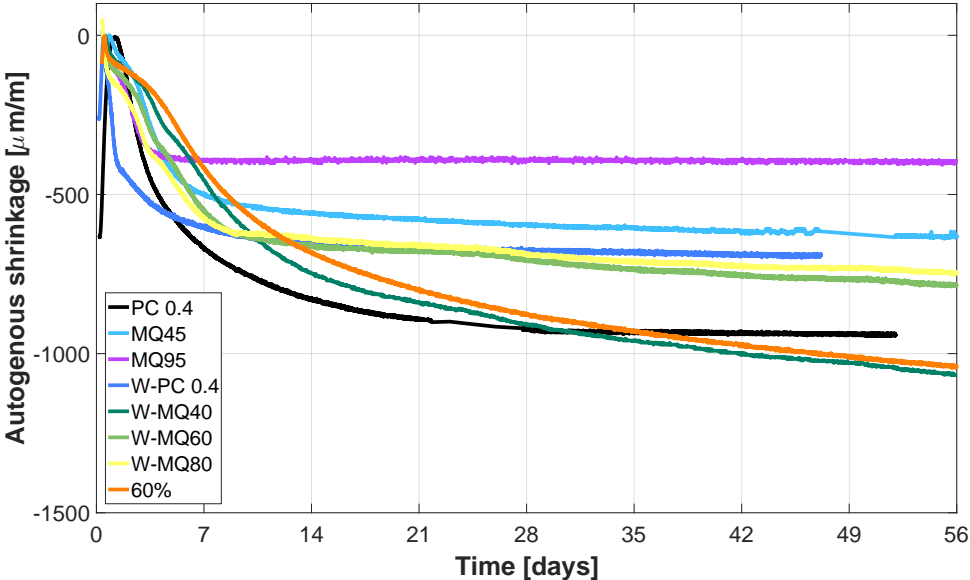


Figure 4.16 – Autogenous shrinkage of the LC³-50 samples with model clays for the two first months of hydration. The trends during the first month of hydration are carried on.

4.3.5 Average pore pressure

The average pore pressure, considered as the main driving force for autogenous shrinkage, can be estimated knowing the relative humidity and saturation level of the porous network. The plot in Figure 4.17 compares the magnitude of this force to the autogenous shrinkage. There is a very clear relationship between these two quantities, for all the measured samples. In particular, the low shrinkage of the MQ (model clays) samples is associated with a low pore pressure and, at the opposite, the LC³-65 has the highest pressure and shrinkage.

According to the Kelvin equation (Eq. 4.4), the Kelvin radius at 28 days — ignoring any adsorbed water — would be around 8 to 9 nm for the LC³-50 25% mix, 7 nm for the LC³-50 45% and the PC 0.4, and around 6 nm for the LC³-65 2:1 mix.

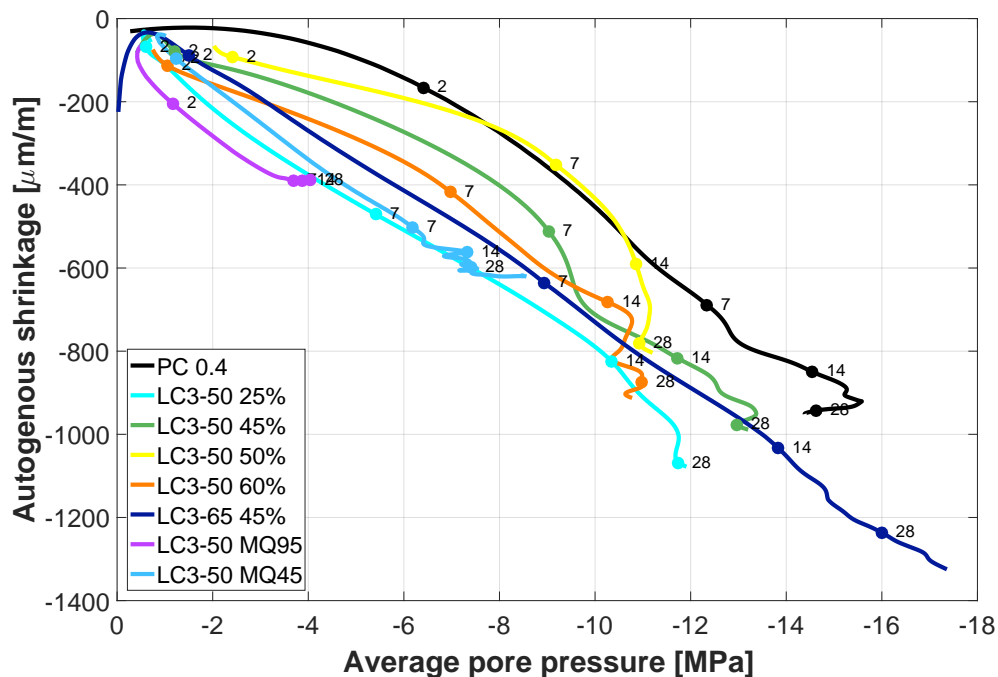


Figure 4.17 – This plot shows the evolution of autogenous shrinkage with progress of the average pore pressure. The marks with the figures indicate the age of the sample. All LC³ samples are cast with a 2:1 calcined to limestone ratio and a W/B of 0.4. MQ samples are cast using a mixture of metakaolin and quartz to emulate a clay of variable grade.

4.4 Shrinkage and microstructure evolution

This section explores potential relations between autogenous shrinkage and microstructural features. As self-desiccation is related to chemical reactions consuming water, ongoing reactions could be the reason for the sustained RH drop and shrinkage of some LC³ samples.

To illustrate, Figures 4.18 to 4.20 compare autogenous shrinkage to degree of reaction of clinker phases and consumed metakaolin from mass balance. Figure 4.18 regroups a plain cement and LC³-50 using natural calcined clays. In the plain cement mix, shrinkage progression happens together with clinker hydration. A common feature among the LC³ blends with clay from 25% to 60% grade is the fast hydration of clinker during the 3 first days, followed by a plateau. Clinker hydration is not associated with much shrinkage, as the curves are mostly horizontal from 3 days on. Clinker in LC³ with the 15% clay reaches a higher degree of hydration than mixtures with higher grade clay. This mix contains very little pozzolanic material (90% of metakaolin has reacted by 7 days), allowing clinker phases to hydrate more thanks to the abundance of water and available space in the microstructure.

In the LC³ mixes (except he 15%), most of metakaolin reacts between 3 and 56 days, a period during which shrinkage progresses steadily. This is a strong indication that it is indeed the reaction of metakaolin — be it to produce C-A-S-H or carboaluminates — which

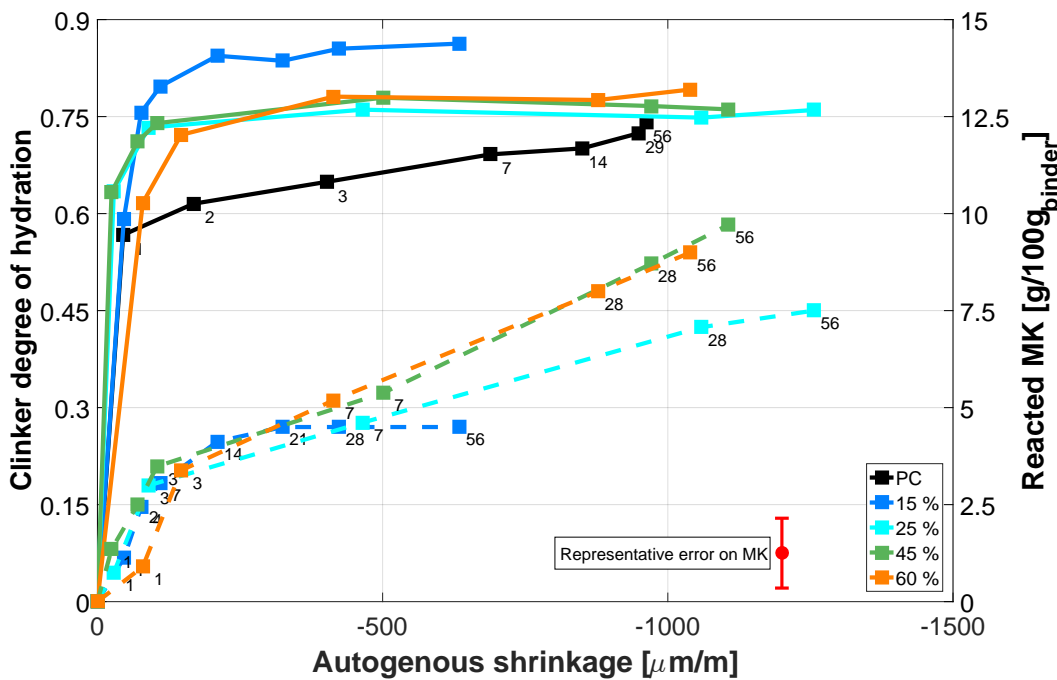


Figure 4.18 – This figure represents the evolution of autogenous shrinkage compared to the degree of hydration of cement (solid lines, left axis) and to the metakaolin consumption (dashed lines, right axis). Figures next to data points represent the sampling age, which is the same for both curves for a given sample.

4.4. Shrinkage and microstructure evolution

is responsible for self-desiccation and build up of sufficient pore pressure to initiate shrinkage. Interestingly, the metakaolin consumption rate is correlated to the shrinkage rate. This is visible in the similar slope of the dashed curves and the similar distance between the time points.

All these features are also visible in Figure 4.19, plotting the same results for LC³-65 mixes. Here, clinker phases hydrate for about 5 days before slowing down. By then, metakaolin has reached about 40 to 45% of hydration and continues to react until depletion (around 56 days for the LC³-65 2:1 and 21 days for the LC³-65 1:1), along with a considerable shrinkage of the material. This suggests that in LC³-65, clinker reaction is already sufficient to provoke enough pore pressure for significant shrinkage. The parallel pozzolanic of metakaolin further desaturate and refines porosity, resulting in important shrinkage. Even the lower amount of metakaolin in LC³-65 1:1 is sufficient to induce enough capillary pressure in the material. The same figure also includes the results for the MQ95 samples, using the same cement but 95% pure metakaolin instead of calcined clay. This highly reactive flash-calcined metakaolin has a very rapid reaction during the 3 first days and then slows down abruptly, similar to the clinker reaction and shrinkage of the material. The high amount of reacted metakaolin suggests that most of the available portlandite is consumed shortly after precipitation. Porosity is quickly refined, but stays mostly saturated as indicated by the relative humidity evolution (see Figure

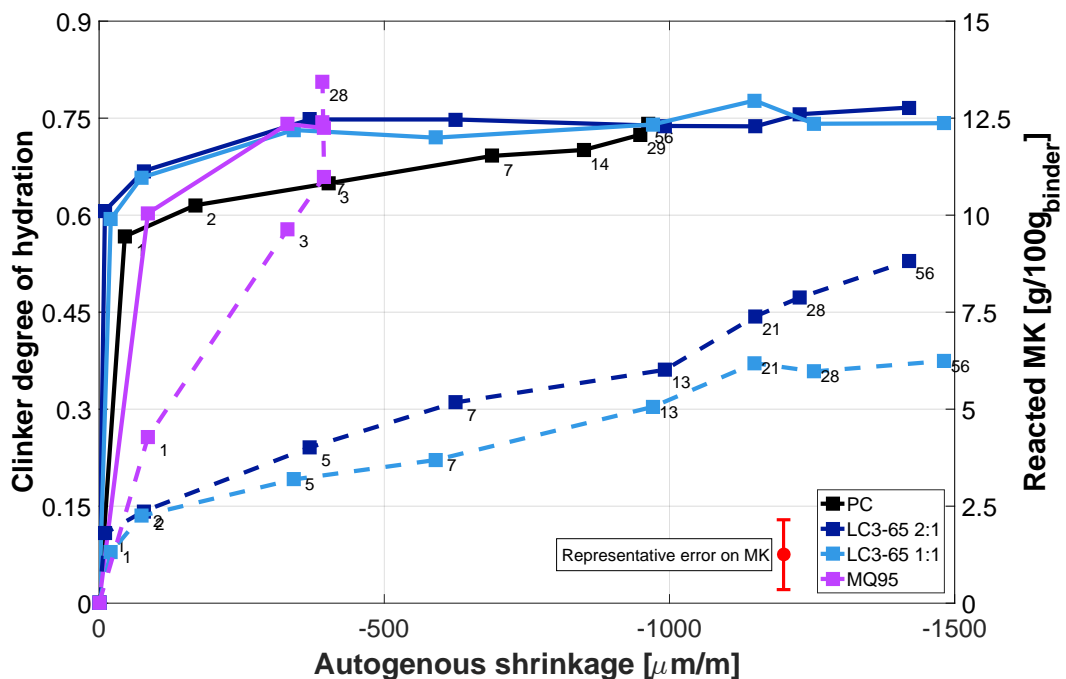


Figure 4.19 – This figure represents the evolution of autogenous shrinkage compared to the degree of hydration of cement (solid lines, left axis) and to the metakaolin consumption (dashed lines, right axis). Figures next to data points represent the sampling age, which is the same for both curves for a given sample.

Chapter 4. Autogenous shrinkage

4.15), resulting in low pore pressure. Note that this is also a consequence of the lower initial porosity of this mix, due to the low density of this specific metakaolin.

This reasoning is also valid for the mixes using white cement, as visible in Figure 4.20. In this case, the relation between clinker degree of hydration and shrinkage is obvious for the plain cement mix. These specific results would be worth a second check, as they were not replicated due to a failure in the shrinkage set-up. The continuous shrinkage measured in the W-MQ40 sample is explained by a larger amount of metakaolin being consumed. This results in a higher pore pressure because of a further desaturation, as demonstrated above with the natural clays. Relative humidity monitoring was not carried out on these samples, but this is likely to be the explanation.

As reported in [4] and [3], the onset of metakaolin reaction corresponds to the sharp increase in compressive strength. This illustrates that space filling and pore refinement from the metakaolin are main actors in strength build-up, together with a consumption of capillary water, increasing pore pressure.

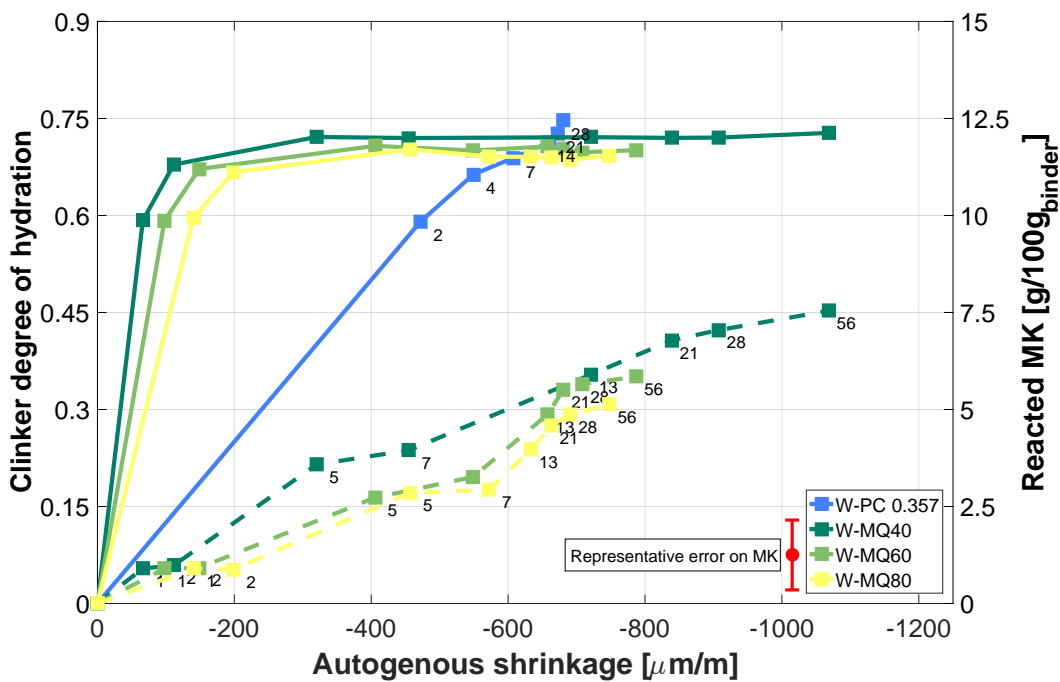


Figure 4.20 – This figure represents the evolution of autogenous shrinkage compared to the degree of hydration of cement (solid lines, left axis) and to the metakaolin consumption (dashed lines, right axis). Figures next to data points represent the sampling age, which is the same for both curves for a given sample.

4.5 Modelling

A poro-visco-elastic model, similar to that described in [16] and in this chapter's introduction was applied to an LC³ material and a plain cement paste. The main purpose is to probe the model with a different type of sample and assess the validity of the superposition principle for such a study. This approach is not entirely predictive, as some of the inputs are obtained using experimental data of autogenous shrinkage. In short, this model estimates the autogenous shrinkage deformation by summing the elastic strain obtained through the Biot-Bishop approach for porous materials and the viscous flow of the material, as a result of an ageing Kelvin-Voigt rheological model (see Chapter 3). The chosen mix were the LC³-50 45%, with a 2:1 calcined clay to limestone ratio and a W/B of 0.4 and the PC 0.4 plain cement mix.

4.5.1 Numerical scheme

The problem is discretized over time domain only and solved for a linear deformation. The elastic strain ε_e is computed incrementally at each time step:

$$\varepsilon_e^{(i)} = \varepsilon_e^{(i-1)} + \frac{1}{3} \left(\frac{1}{K^{(i)}} - \frac{1}{K_s} \right) \cdot (\Delta P \cdot S^{(i)} + P^{(i)} \cdot \Delta S) \quad (4.12)$$

The bulk modulus $K^{(i)}$ at the current time is obtained from the Young's modulus and the Poisson's ratio at the concerned time. ΔP and ΔS are the increment in capillary pressure or saturation level from the previous tie step.

Basic creep compliance is obtained through the ageing Kelvin-Voigt rheological model presented in Chapter 3. At each time step, the properties of every elements of the branches are updated, the stress in each component is computed according to the change in average pore pressure and strains of all the branches are added. At the end of each iteration, the product $\frac{\partial J(t, \tau)}{\partial t} dt \cdot d\sigma$, representing the viscous strain from a uniaxial stress on the material, is computed. The complete resolution scheme is available in this publication from Hilaire [14].

4.5.2 Inputs of the model

This model requires a number of inputs from experimental data. Some of them are already presented in the previous sections or chapters but are summarized again here. Certain inputs are approximated using an appropriate function. As the model is discretized over time but most physical parameters are related to the degree of hydration, both representations are used. The time window of the simulation spans from about 1.2 (earliest stable RH reading) to 30 days.

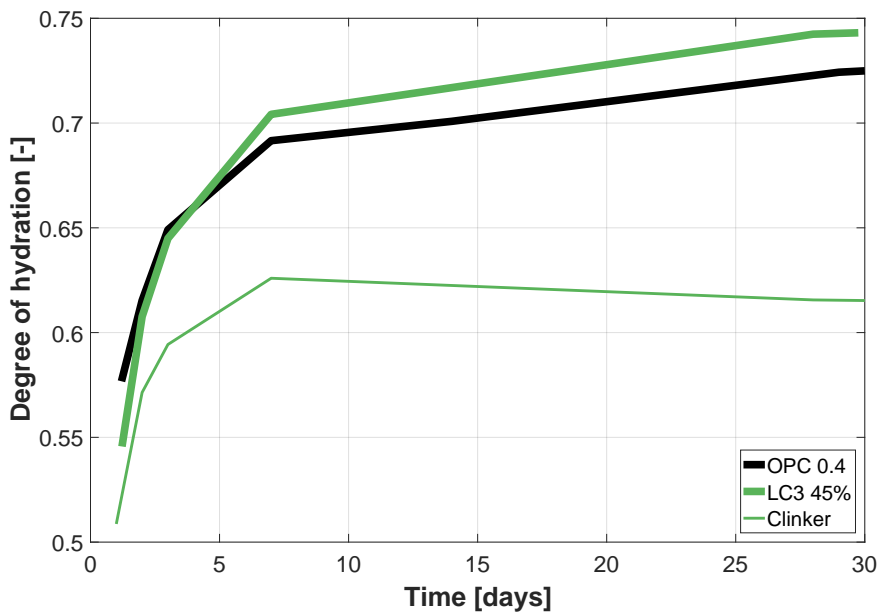


Figure 4.21 – Degree of hydration over time of clinker phases and metakaolin combined. The thin line represents the contribution of clinker to the degree of hydration of the binder. The seemingly downward trend is within the calculation error.

Degree of hydration

In LC³, previous results showed that mechanical properties in general were affected by the metakaolin hydration, and that the degree of hydration of clinker was almost constant after 3 to 5 days. The choice was made to consider the degree of hydration of both clinker and metakaolin. Degree of hydration is the variable used for ageing of the rheological model. Figure 4.21 shows its evolution over the considered time. The sharp increase at the beginning is mostly due to the rapid hydration of cement, whereas the slow increase from about 7 days on is the result of metakaolin reaction.

Relative humidity

Evolution of relative humidity from self-desiccation (RH_k) is summarized on Figure 4.22. As observed earlier, the high water to clinker ratio of LC³-50 means that the pore network remains saturated during most of the clinker reaction period and then the metakaolin reaction causes a drop in relative humidity.

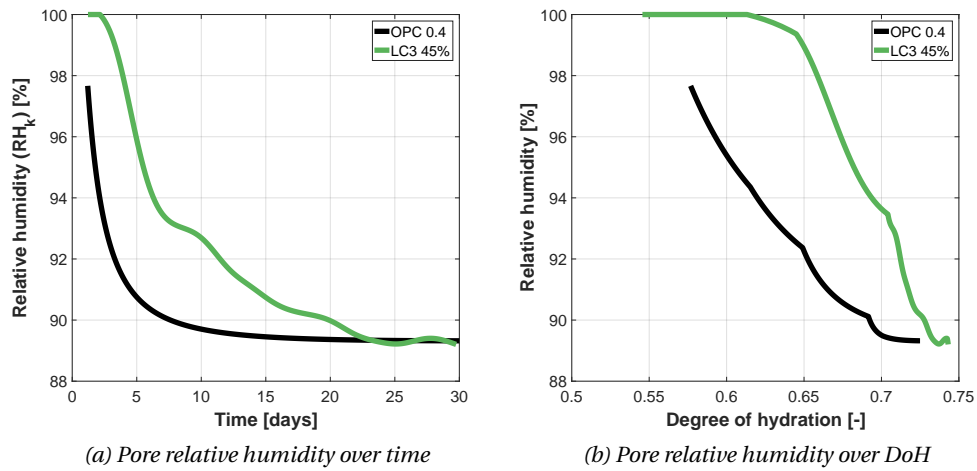


Figure 4.22 – Evolution of relative humidity in the pore network over time and degree of hydration.

Saturation level

Evolution of saturation level, obtained through mass balance calculation, is summed up on Figure 4.23. It is well approximated with a logarithmic function over the considered time period.

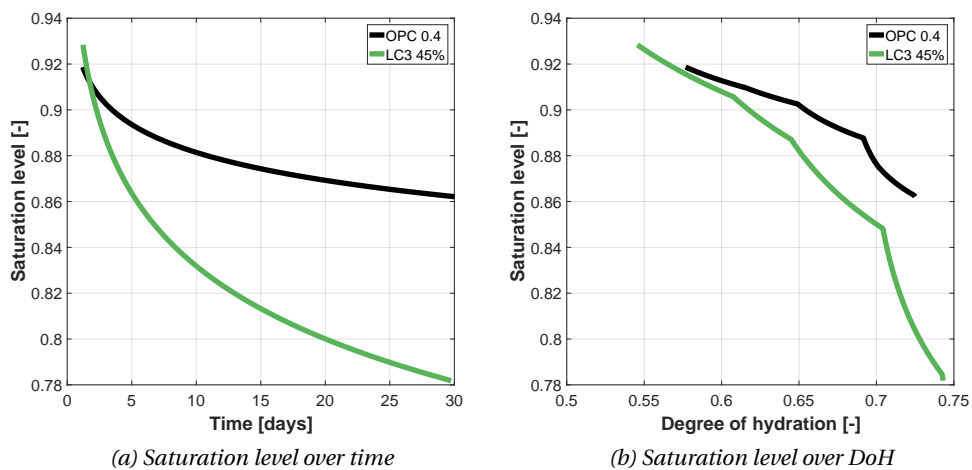


Figure 4.23 – Evolution of the saturation level of the porosity, considering gel and interlayer water as part of the evaporable water.

Average pore pressure

The product of capillary pressure and saturation level is called average pore pressure and is an approximation of the total pore pressure that would be obtained if knowing the exact geometry of the pores. It is the driving force for modelling autogenous shrinkage. As depicted on Figure 4.24, the average capillary stresses can reach 12 MPa in these materials, which is higher than the stress applied for the creep test, but still in the linear domain.

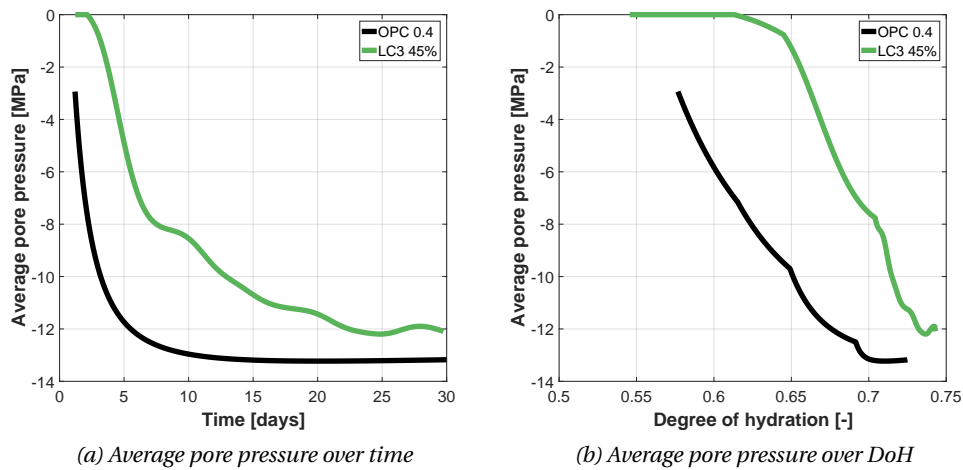


Figure 4.24 – Evolution the average pore pressure over time and degree of hydration. Average pore pressure is the product of capillary pressure and saturation level.

Young's modulus

Evolution of the macroscopic Young's modulus from a combination of data from the EMM-ARM set-up and loading/unloading cycles from the creep tests is reported in Figure 4.25. To obtain a smooth curve, experimental data was fit using a sigmoid function. Progress of Young's modulus is almost linear with respect to degree of hydration.

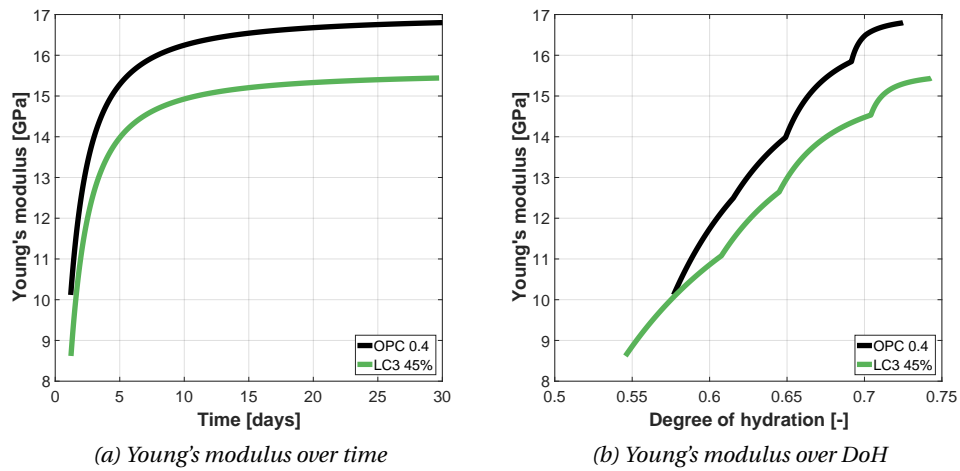


Figure 4.25 – Evolution Young's modulus over time and degree of hydration. Data were fit using a sigmoid equation.

Other parameters

As presented in the introductory section, the Biot-Bishop approach for poro-elasticity requires a number of additional parameters. The elastic Poisson's ratio was considered constant and equal to 0.22. The K_S parameter, the bulk modulus of the solid material composing the cement paste, was set to 44 GPa and constant. The viscous Poisson's ratio was set to 0.22 and constant, similarly to the elastic ratio. The computational time steps were set to 0.003 day, in order to have a time increment of the order of one third of the shortest characteristics time of the rheological model.

4.5.3 Model output and discussion

Elastic and viscous strain were computed at each time step and summed to obtain the total autogenous shrinkage. Results are shown on Figure 4.26, splitting the elastic and viscous components of the strain. The overall trend of the predictions is in reasonable agreement with the experimental data. However, the shrinkage amplitude for the PC 0.4 is overestimated by the model by about 400 μm and the amplitude of the LC³ is underestimated by about 200 μm . The computed elastic strain is comparable between both samples and this is in accordance with similar pore pressures and a lower Young's modulus for the LC³. The simulated viscous strain is about three times higher for the PC than the LC³, which is in agreement with the previously presented results on basic creep compliance. Results from Hu [16] on plain cement paste at a W/C of 0.35 predicted a viscous strain about three times more important than the elastic one, which is similar to what was calculated here.

The discrepancy between the simulations and the experimental data could be of various origins, considering the number of assumptions required to build this model. The next part is an attempt at understanding the possible causes and implications.

- If the superposition principle is not valid for the materials and the coupling between creep and shrinkage is important, the creep data processing would not be valid and the rheological model would not be representative of the materials.
- An wrong estimation of the driving force could explain the different responses in the simulation. Relative humidity was consistent among the various studied samples, but average pore pressure was then estimated using only the saturation level combined with

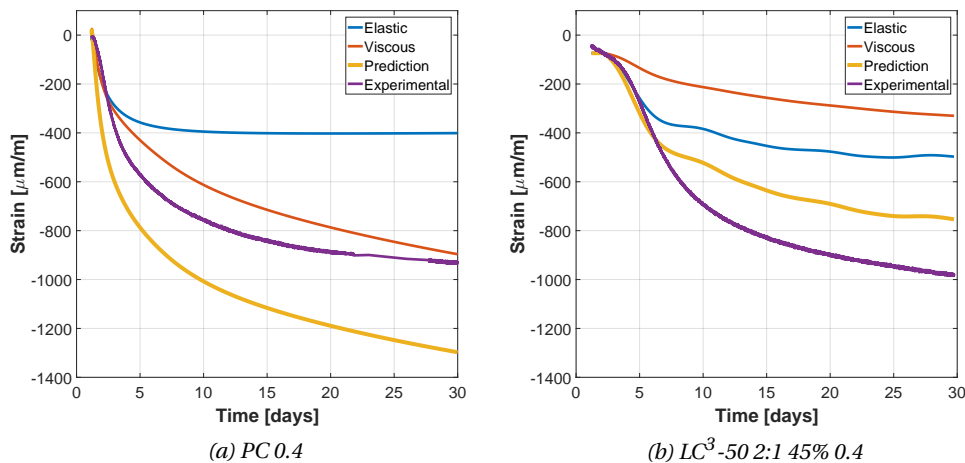


Figure 4.26 – Autogenous shrinkage modelling results. The elastic and viscous strain contributions of the prediction are plotted individually. The elastic strain is comparable in both simulations. That is not the case for the viscous strain, which is nevertheless in agreement with the observations on uniaxial compressive basic creep.

capillary pressure. Saturation level of the porosity is not a value that is easily measured experimentally and must be obtained through calculation. Moreover, saturation level is an approximation of Bishop's coefficient, which represents the fraction of the pore network surface in contact with pore water. The validity of this assumption has been questioned [13].

- A higher bulk modulus K_S of the solid material would increase the total strain undergone by the porous material. However, this quantity is more likely to decrease with hydration, as it represents the bulk modulus of the non-porous binder matrix, and hydrates in general have a lower stiffness than the clinker phases [32], [20]. This effect could nevertheless be tempered in LC^3 : the Young's modulus of the clay mineral is rather close to that of C-S-H [7].
- Lower elastic and/or viscous Poisson's ratios would increase the calculated strains. This could indeed be a source of error, as a slight variation (± 0.02) in these ratios could decrease the difference between the model and the experiment to about $100 \mu\text{m}$. Nevertheless, the initial value of 0.22 is already on the lower end for Poisson's ratio in cementitious material.
- The rapidly evolving properties of the rheological model implies that a short advance or time delay in the estimation of the average pore pressure can cause an important over- or underestimation of the strain at early age.
- Lastly, the viscous contribution of strain is obtained from uniaxial creep behaviour of the material, which is then converted to a linear bulk strain using a viscous Poisson's ratio. This simple transition from a strain due to an axial stress to a strain caused by a hydrostatic pressure could not reflect the real situation.

To sum up, the model seems to indicate that the superposition principle is adapted as a first order approximation. The amount of experimental or calculated inputs required for the calculation, each coming with their own uncertainty, could in addition explain part of the discrepancy.

4.6 Conclusions

This study on autogenous shrinkage of LC³ paste leads to the following findings. Firstly, as expected with SCMs and the dilution effect on clinker, LC³ mixes show a delay of the initial shrinkage onset. This retardation is longer for higher substitution levels and, for naturally occurring clays, independent of the grade of the clay. This effect is much reduced when using model clays based on industrial grade, flash-calcined metakaolin. As illustrated in the previous plots, plain cement-based mixtures have a noticeable initial expansion before the monotonous shrinkage regime. This expansion is extremely reduced when using calcined clays, even in low amounts (as in LC³-65 1:1 for instance). Overall, the studied LC³ blends had similar shrinkage amplitude to equivalent W/S plain cement mixes, except for the LC³-65 — solely studied with the 45% clay — which showed a larger shrinkage than cement references. The main reason for this important strain is the high average pore pressure.

At equivalent W/S, LC³ binders show lower shrinkage than plain cement mixtures. This is a consequence of the higher internal relative humidity and saturation level. The comparable level of shrinkage among LC³-50 binders is explained by the very similar microstructure and water content over time. In these mixes, clinker quickly reacts up to about 75% hydration during the first 2 to 3 days, producing a similar amount of hydrates in all cases. This is followed by the onset of the pozzolanic reaction of metakaolin. The rate and amount of consumed metakaolin is very consistent among all LC³ samples with clays from 25% to 60% grade. This implies that the amount of water and portlandite consumed, as well as the new hydrates formed, are similar. Hence, this indicates that the relative humidity and saturation level of all these blends should be similar. This is supported by the calculation of the average pore pressure, showing similar values for the studied mixes. Together with a similar Young's modulus, this explains the similar shrinkage behaviour of this set of samples. This behaviour is also observed in model clays. However, data showed that a model clay could not mimic a natural clay with the same amount of metakaolin. The suggested reason is the better availability and reactivity of the flash-calcined metakaolin used in these mixes.

The modelling approach based on the stress superposition principle of visco-elastic materials yielded a reasonable estimation of the autogenous shrinkage. In spite of the creep measurements being carried out under an axial stress that was about half of the average pore pressure undergone by the samples, the model is able to grasp the changes in strain rate quite well. This shows that the superposition principle is a satisfactory method to deal with creep data, although not being formerly proved or disproved.

4.7 References

- [1] ASTM C157/C157M - 08. “Standard Test Method for Length Change of Hardened Hydraulic-Cement Mortar and Concrete”. *ASTM International, West Conshohocken, PA* (2014).
- [2] François Henri Avet. “Investigation of the grade of calcined clays used as clinker substitute in Limestone Calcined Clay Cement (LC3)” (2017), p. 169.
- [3] François Avet and Karen Scrivener. “Investigation of the calcined kaolinite content on the hydration of Limestone Calcined Clay Cement (LC 3)”. *Cement and Concrete Research* 107 (2018), pp. 124–135.
- [4] François Avet et al. “Development of a new rapid, relevant and reliable (R3) test method to evaluate the pozzolanic reactivity of calcined kaolinitic clays”. *Cement and Concrete Research* 85 (2016), pp. 1–11.
- [5] Bangham D. H., Fakhoury Nazim, and Chapman David Leonard. “The swelling of charcoal. Part I.—Preliminary experiments with water vapour, carbon dioxide, ammonia, and sulphur dioxide”. *Proceedings of the Royal Society of London. Series A, Containing Papers of a Mathematical and Physical Character* 130.812 (Dec. 1930), pp. 81–89.
- [6] Bangham D. H. et al. “The swelling of charcoal. Part II.—Some factors controlling the expansion caused by water, benzene and pyridine vapours”. *Proceedings of the Royal Society of London. Series A, Containing Papers of a Mathematical and Physical Character* 138.834 (Oct. 1932), pp. 162–183.
- [7] Arpita Pal Bathija. “Elastic properties of clays”. en (), p. 129.
- [8] Françoise Beltzung and Folker H. Wittmann. “Role of disjoining pressure in cement based materials”. *Cement and Concrete Research* 35.12 (Dec. 2005), pp. 2364–2370.
- [9] ASTM C1698-09. “Standard Test Method for Autogenous Strain of Cement Paste and Mortar” (2014).
- [10] CEB-FIP Model Code. “Model code for concrete structures”. *Comité Euro-International du Béton, Secretariat Permanent, Case Postale* 88 (1990).
- [11] O. Coussy et al. “The equivalent pore pressure and the swelling and shrinkage of cement-based materials”. en. *Materials and Structures* 37.1 (Jan. 2004), pp. 15–20.
- [12] C. F. Ferraris and F. H. Wittmann. “Shrinkage mechanisms of hardened cement paste”. *Cement and Concrete Research* 17.3 (May 1987), pp. 453–464.
- [13] Dariusz Gawin, Francesco Pesavento, and Bernhard A. Schrefler. “Hygro-thermo-chemo-mechanical modelling of concrete at early ages and beyond. Part II: shrinkage and creep of concrete”. fr. *International Journal for Numerical Methods in Engineering* 67.3 (2006), pp. 332–363.

- [14] Adrien Hilaire et al. “Modeling basic creep in concrete at early-age under compressive and tensile loading”. *Nuclear Engineering and Design*. Special Issue - The International Conference on Structural Mechanics in Reactor Technology (SMiRT21), New Delhi India, Nov 06-11, 2011 269 (Apr. 2014), pp. 222–230.
- [15] KH Hiller. “Strength reduction and length changes in porous glass caused by water vapor adsorption”. *Journal of Applied Physics* 35.5 (1964), pp. 1622–1628.
- [16] Zhangli Hu. “Prediction of autogenous shrinkage in fly ash blended cement systems” (2017), p. 213.
- [17] C Hua, P Acker, and A Ehlacher. “Analyses and models of the autogenous shrinkage of hardening cement paste: I. Modelling at macroscopic scale”. *Cement and Concrete research* 25.7 (1995), pp. 1457–1468.
- [18] Jun Liu et al. “Prediction of autogenous shrinkage of concretes by support vector machine”. *International Journal of Pavement Research and Technology* 9.3 (May 2016), pp. 169–177.
- [19] Pietro Lura, Ole Mejlhede Jensen, and Klaas van Breugel. “Autogenous shrinkage in high-performance cement paste: an evaluation of basic mechanisms”. *Cement and Concrete Research* 33.2 (2003), pp. 223–232.
- [20] J. Moon et al. “First-principles elasticity of monocarboaluminate hydrates”. en. *American Mineralogist* 99.7 (July 2014), pp. 1360–1368.
- [21] Moncef L. Nehdi and Ahmed M. Soliman. “Artificial Intelligence Model for Early-Age Autogenous Shrinkage of Concrete”. English. *Materials Journal* 109.3 (May 2012), pp. 353–362.
- [22] István Nemes. “Revisiting the applications of drainage capillary pressure curves in water-wet hydrocarbon systems”. *Open Geosciences* 8.1 (2016), pp. 22–38.
- [23] Ch. Pichler and Roman Lackner. “A multiscale creep model as basis for simulation of early-age concrete behavior”. 2008.
- [24] Treval C Powers. “Mechanism of shrinkage and reversible creep of hardened cement paste”. *Proc. Int. Symp. Concr., London, 1965*. 1965.
- [25] Mohammad H Rafiei et al. “Neural Network, Machine Learning, and Evolutionary Approaches for Concrete Material Characterization.” *ACI Materials Journal* 113.6 (2016).
- [26] Gaurav Niteen Sant, Pietro Lura, and Weiss. “Measurement of volume change in cementitious materials at early ages” (2006).
- [27] R Shuttleworth. “The Surface Tension of Solids”. *Proc. Phys. Soc.* 63 (1950).
- [28] I. Soroka. *Portland Cement Paste and Concrete*. Macmillan, 1979.
- [29] E Tazawa and S Miyazawa. “Influence of constituents and composition on autogenous shrinkage of cementitious materials”. *Magazine of Concrete Research* 49.178 (1997), pp. 15–22.
- [30] Ei-ichi Tazawa. *Autogenous shrinkage of concrete*. CRC Press, 2014.

- [31] Ei-ichi Tazawa et al. “Work of JCI committee on autogenous shrinkage”. *Shrinkage of Concrete, Shrinkage* (2000), pp. 21–33.
- [32] Karine Velez et al. “Determination by nanoindentation of elastic modulus and hardness of pure constituents of Portland cement clinker”. *Cement and Concrete Research* 31.4 (Apr. 2001), pp. 555–561.
- [33] Ivan Vlahinić, Hamlin M. Jennings, and Jeffrey J. Thomas. “A constitutive model for drying of a partially saturated porous material”. *Mechanics of Materials* 41.3 (Mar. 2009), pp. 319–328.
- [34] R Wendner, MH Hubler, and ZP Bažant. “The B4 model for multi-decade creep and shrinkage prediction”. In: *Mechanics and Physics of Creep, Shrinkage, and Durability of Concrete: A Tribute to Zdeňk P. Bažant*. 2013, pp. 429–436.
- [35] Mateusz Wyrzykowski and Pietro Lura. “Effect of relative humidity decrease due to self-desiccation on the hydration kinetics of cement”. *Cement and Concrete Research* 85 (July 2016), pp. 75–81.
- [36] Mateusz Wyrzykowski et al. “Corrugated tube protocol for autogenous shrinkage measurements: review and statistical assessment”. en. *Materials and Structures* 50.1 (Aug. 2016), p. 57.
- [37] J. C. Yates. “Effect of Calcium Chloride On readings of a Volumeter Inclosing Portland cement Pastes and on Linear Changes of Concrete”. *Highway Research Board Proc.* 40.21 (1941), pp. 294–304.

5 Conclusions and future perspectives

The main goal of this research project was to investigate delayed strains in LC³ materials, specifically basic creep and autogenous shrinkage strains. The final chapter of this thesis summarizes the main findings concerning these phenomena and their potential links with microstructure evolution. Numerical models were also used to interpret the experimental results further. Naturally, questions rose from this investigation; the last part of these chapters suggests steps to be taken for further research.

Contents

5.1 Basic creep of LC³ mature paste	118
5.1.1 Experimental part	118
5.1.2 Creep kinetics and microstructure	118
5.1.3 Basic creep modelling	119
5.1.4 Perspectives	120
5.2 Autogenous shrinkage	122
5.2.1 Experimental part	122
5.2.2 Shrinkage and hydration	122
5.2.3 Autogenous shrinkage modelling	123
5.2.4 Perspectives	123
5.3 Closing words	124
5.4 References	124

5.1 Basic creep of LC³ mature paste

5.1.1 Experimental part

Basic compressive creep tests were carried out on plain cement and LC³ samples, using calcined clays of different grades. Measurement started after 28 days of curing and lasted 28 days. The main findings from the experimental results are listed:

- Basic compressive creep compliance of mature LC³ binders is lower than that of plain cement samples. This is valid for clays with a calcined kaolinite content as low as 25% in a LC³-50 type mix.
- The compliance reduction in LC³-50 is similar for all mixtures containing at least 10% of metakaolin in total. This is illustrated on Figure 5.1 below. This corresponds to the necessary amount of metakaolin to consume most of the portlandite from clinker hydration.
- At equivalent W/B or W/S, LC³-50 binders have a lower creep compliance than plain cement mixes.

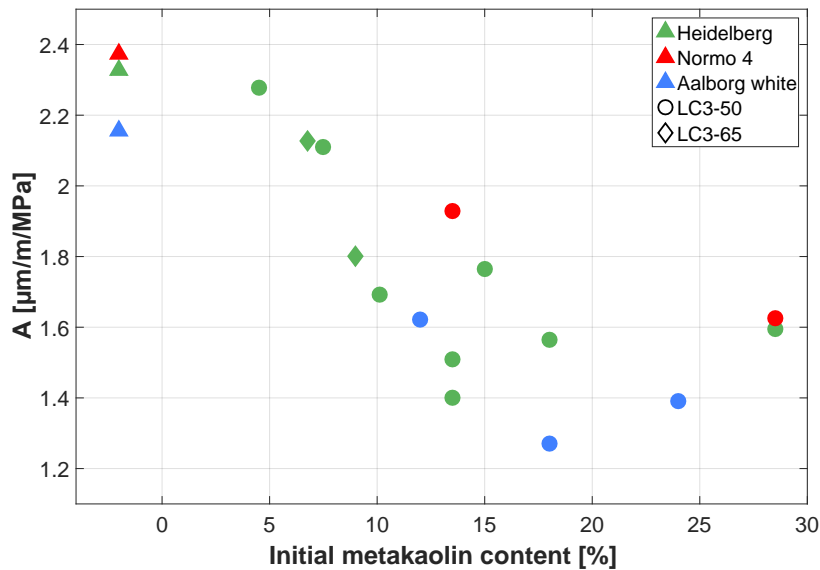


Figure 5.1 – This graphs show the evolution of the fitted creep amplitude factor with initial metakaolin content for mixes with a W/B of 0.4. The amplitude factor is not decreasing significantly after a threshold value of about 12% of initial metakaolin content.

5.1.2 Creep kinetics and microstructure

Creep data was processed and fitted with either a power law or a logarithmic function. The power function was better adapted to fit experimental data shortly after loading, whereas

the logarithm was better suited to later age. A microstructural characterisation of the samples at loading age was carried out using XRD, SEM-EDS and mass balance. The results help to interpret the experimental data in the following way:

- When fitting with a power law, a similar exponent could be used to fit all studied samples (plain cement, LC³-50 or LC³-65). This means that the observed differences in compliance can be expressed as a single amplitude factor.
- The amplitude of such factor appeared to be partly correlated to the C–A–S–H volume amount in the paste, but also to the average chemical composition of the C–A–S–H, indicating that the lower amount of amorphous hydrates in LC³ was a reason for the decreased compliance, but that the properties of C–S–H could be different.

5.1.3 Basic creep modelling

A two-dimensional finite elements model was used to simulate the viscoelastic behaviour of the samples being studied. The inputs of the model are the volume fractions of phases from mass balance calculation. The only viscoelastic phase is the C–S–H matrix, comprised of C–S–H gel, capillary water and air voids. The properties of the matrix were back-calculated to fit the experimental data. Elastic and viscous properties of the C–S–H gel were obtained through an analytical poromechanical approach. The outcome of the model helped to draw the following conclusions:

- The back-calculated Young's modulus of the C–S–H gel fell within a range from 22 to 26 GPa, and from 60 to 75 GPa for the bulk C–S–H, for all modelled systems, including plain cement and LC³ with varied clays, see Figure 5.2. This is in good agreement with the existing literature, be it for C–S–H gel or bulk C–S–H, which is close to values for tobermorite. This modulus characterizes the average C–S–H gel, as no distinction was made between inner and outer products in the mass balance calculation.
- The poromechanical approach indicated that a C–S–H gel with similar elastic properties could be used to model all the systems, and that variations could be explained by a different amount of C–S–H gel and capillary porosity.
- The model indicated a much lower creep compliance of the C–S–H gel in the LC³ systems, for all clays being studied, independent of the W/B or clay purity, see Figure 5.3.
- The lower compressive basic creep compliance of the LC³ materials is then the result of a lower amount of C–S–H gel, and also of its different rheological properties.

Together with the results from the microstructural analysis, this indicates that the higher viscosity of C–S–H could originate from a different arrangement or intermixing with other

phases rather than a significant change of rheology due to the chemical compositions, as the modelled C–S–H is the same for all the LC³, regardless of its average atomic ratios. The physical effects causing a change of compliance at the C–S–H scale could be a structural reinforcement from the clayey particles or an increased amount of interface due to the filler effect of the limestone and clay powders. The isolation of these effects needs specific investigation.

5.1.4 Perspectives

At the paste scale, longer compressive creep tests should be carried out to isolate the long-term behaviour of the ternary blends properly. A better monitoring of the compliance evolution could be obtained by applying minute-long creep tests, as described in Irfan-ul-Hassans’s work [1]. This would allow for comparisons of the time-dependence of creep modulus between plain cement and ternary blends, for a better orientation of building codes for LC³.

Nano-indentation, coupled with a statistical analysis of the results, could provide a set of data allowing for a direct inference or even a confirmation of the lower compliance of C–S–H gel in LC³ materials [2]. Such a study could be carried out on binders with a C–S–H composition and quantity similar to LC³, but without metakaolin as a source of aluminium and silicon. This could prompt us to consider the impact of the chemistry of C–S–H on its viscous properties and the importance of embedding plate-like particles in the microstructure.

Convincing results at the paste scale should be followed by a creep campaign at the concrete scale, possibly in tension and bending as well. Standard tests should be carried out to demonstrated that these materials comply with the various national guidelines.

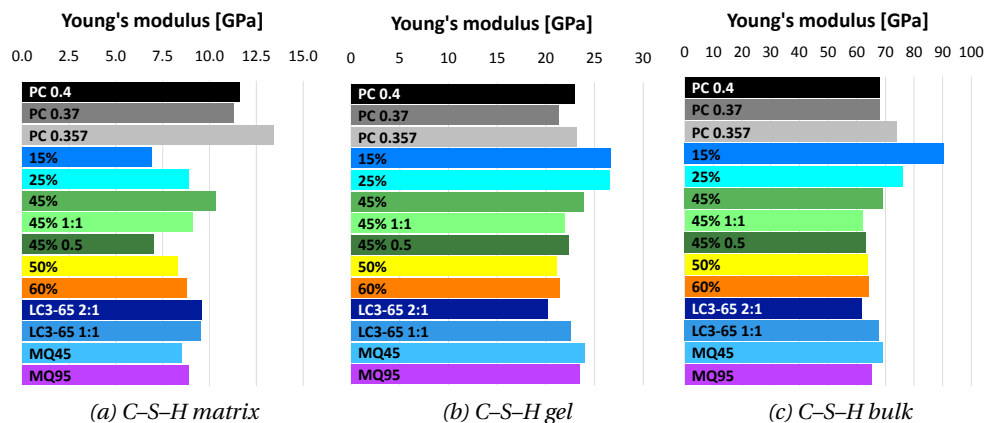


Figure 5.2 – Summary of the back-calculated C–S–H elastic properties, obtained using an analytical, poromechanical approach on the model output.

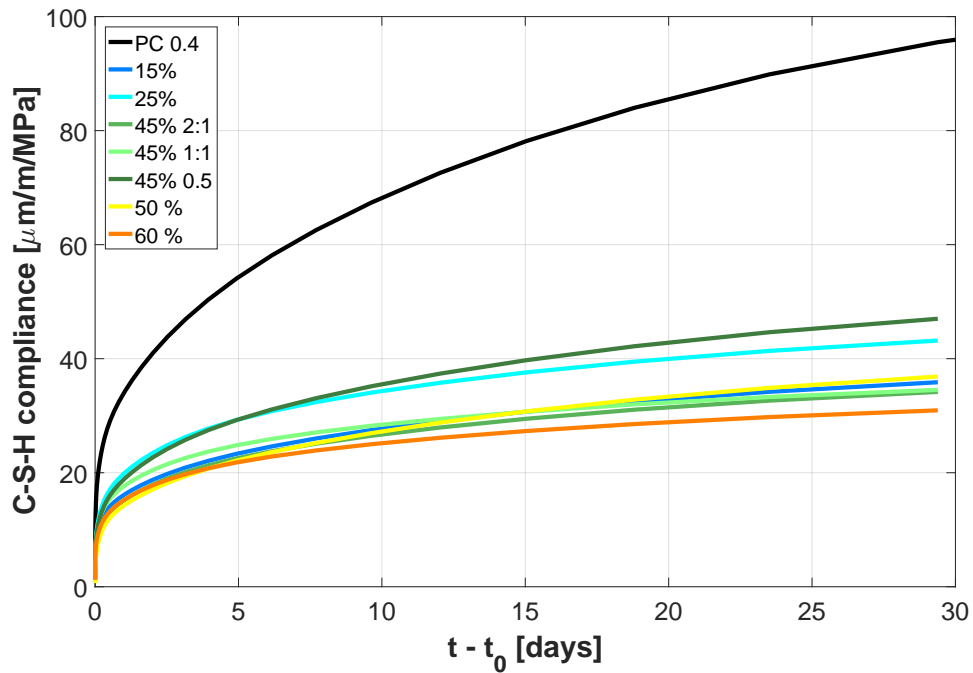


Figure 5.3 – C–S–H gel compliance calculated from the statistical model for the LC³-50 mixes using natural clays of variable kaolinite content (15% to 50%), calcined clay to limestone ratio (generally 2:1, except for one sample at 1:1) and W/B (0.4, except for one sample at 0.5). The aluminium content of the C–S–H is linked to the metakaolin content of the mix, but no correlation is seen here.

As for shrinkage, creep measurements in drying conditions should be carried out. The higher amount of available capillary water in the LC³ pore network could have an effect on drying strains.

5.2 Autogenous shrinkage

5.2.1 Experimental part

Autogenous shrinkage of LC³ binders with various clays was monitored for 56 days after casting and compared to plain cement samples. The following list summarizes the main observations from these tests:

- The presence of SCM causes a dilution effect and a delay of the shrinkage onset, which is proportional to the replacement fraction.
- LC³-50 type mixes showed a comparable shrinkage than W/B or W/S equivalent plain cement after two months of hydration.
- Low-reactivity clays caused only a modest amount of shrinkage, whereas moderate to high reactivity natural calcined clays had a similar effect on autogenous shrinkage. Pure metakaolin as pozzolan caused a rapid shrinkage followed by a stable regime from about 7 days on.
- Shrinkage of LC³-65 mixes (*i.e.* containing 65% of clinker) was found to be higher than plain cement mixes.

5.2.2 Shrinkage and hydration

- For all studied mixes, a clear and expected correlation between autogenous shrinkage and average pore pressure was highlighted.
- The similar shrinkage rate and amplitude observed for the LC³-50 mixes with moderately to highly reactive clays is explained by a similar microstructure evolution. In these mixes, clinker phases quickly reach a similar degree of hydration within 3 to 5 days. The pozzolanic reaction of calcined kaolinite begins around 2 to 3 days after mixing, consuming the portlandite produced and the capillary water at a similar rate for these blends. If there is enough metakaolin to consume most of the accessible portlandite, this will cause a comparable refinement and desaturation of the porosity in these samples. The result is an analogous capillary force at the origin of autogenous shrinkage.
- The situation is comparable in LC³-65, but the higher cement content can further decrease saturation before relative humidity is further decreased by the pozzolanic reaction, resulting in higher capillary stresses and shrinkage than LC³-50.

This implies that autogenous shrinkage in LC³ is controlled by the amount of clinker rather than the grade of the clay. This means that shrinkage mitigation has to come from the mix design and not by a selection or blending of the available clay.

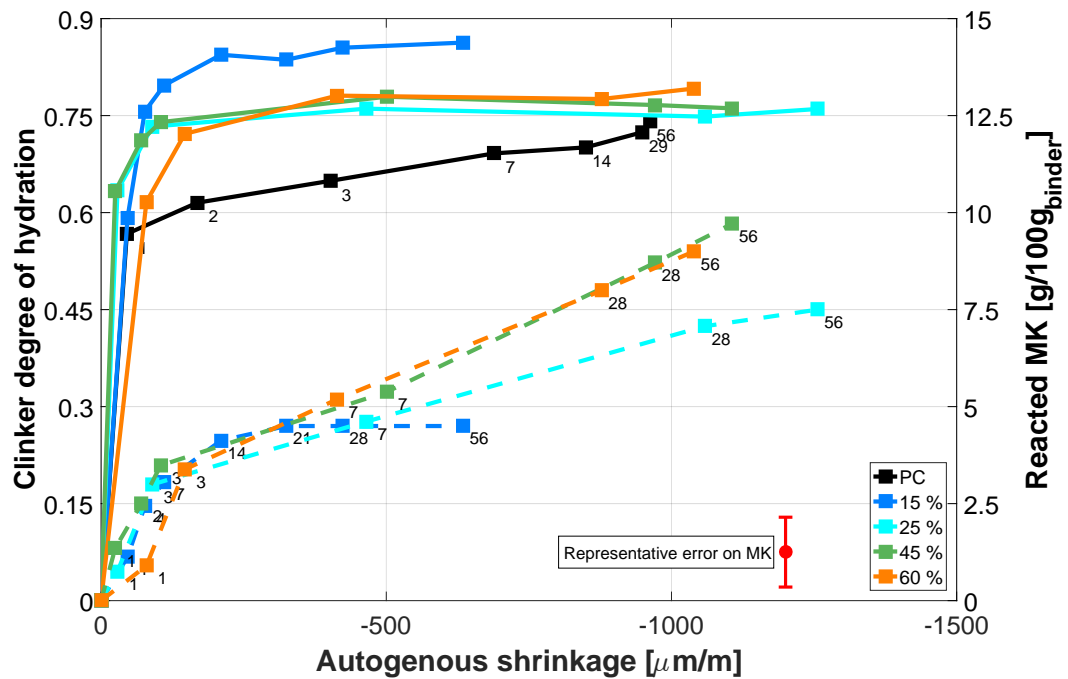


Figure 5.4 – This figure represents the evolution of autogenous shrinkage compared to the degree of hydration of cement (solid lines, left axis) and to the metakaolin consumption (dashed lines, right axis). Figures next to data points represent the sampling age, which is the same for both curves for a given sample.

5.2.3 Autogenous shrinkage modelling

The poro-viscoelastic model could grasp the trend of autogenous shrinkage for a plain cement and LC³ mix, by separate computation of the elastic and viscous strains. The addition of a Kelvin-Voigt unit and suppression of the single damper from the initial model allowed a better fit of the ageing creep behaviour than the original model. The model is still very sensitive to the initial conditions, as a temporal mismatch between the pore pressure and ageing rheological model can result in an over- or underestimation of the strain during the first days. Nevertheless, this approach used the stress superposition principle for viscoelastic materials and yielded qualitatively reasonable results, illustrating that the principle is applicable to such materials.

5.2.4 Perspectives

As for creep, a test campaign in drying conditions would be advised to monitor shrinkage of LC³ in field-like conditions. The high free water content in early age LC³ samples could imply a higher drying strain and potentially a great risk of cracking, especially if exposed to drying during the 3 first days of hydration.

The predictive model could be improved using a different approach to obtain the viscous behaviour of the material. One suggestion would be to apply a short duration test method, such as that described in [1]. This procedure would have the advantage of not requiring an independent measurement of the autogenous shrinkage. Ageing viscosity could then be expressed as a power or logarithmic function, with time-dependent coefficients.

5.3 Closing words

This research project allowed to shed light on the visco-elastic behaviour of the promising ternary mixes of limestone and calcined clays. Experiments and models helped to highlight the specific visco-elastic behaviour of C-A-S-H gel in LC³ and to understand how microstructure evolution was related to macroscopic shrinkage thanks to a combination of various experimental techniques and numerical tools. The low creep observed in LC³ binders is of great interest for engineering applications, as is it an asset for the long term stability of structures. Moreover, a slower viscous flow could easily be taken into account in the actual building codes by means of simple coefficients when dealing with LC³. Some creep is advantageous at the early age for relaxing constraints, but, as demonstrated here, the early age autogenous shrinkage of these binders is limited and should not pose any problem if the structures are correctly engineered.

Data gathered in this work are valuable to tailor the mix design of LC³ to the available resources. It was demonstrated here that only a certain amount of metakaolin was consumed during the evolution of the microstructure, and it is also known that only a fraction of the limestone is reacting. Therefore, a part on these materials could be replaced with even more inexpensive filler or low-value — potentially harmful for the environment — industrial by-products, such as ashes or sludge, effectively increasing the sustainability of LC³ further.

Experimental data from basic creep and autogenous shrinkage measurement are available on-line from go.epfl.ch/thesis_ston.

5.4 References

- [1] M. Irfan-ul-Hassan et al. “Elastic and creep properties of young cement paste, as determined from hourly repeated minute-long quasi-static tests”. *Cement and Concrete Research* 82 (Apr. 2016), pp. 36–49.
- [2] William Wilson, Luca Sorelli, and Arezki Tagnit-Hamou. “Automated coupling of NanoIndentation and Quantitative Energy-Dispersive Spectroscopy (NI-QEDS): A comprehensive method to disclose the micro-chemo-mechanical properties of cement pastes”. *Cement and Concrete Research* 103.Supplement C (Jan. 2018), pp. 49–65.

A Experimental data processing

Some specific methodology is necessary in order to study the first time derivative of experimental data. Indeed, a direct $\Delta y / \Delta x$ derivation may not give any usable results, especially if the raw data is smeared with high frequency noise. The main workarounds are either to fit the experimental data with a set of derivable functions or to use a specialized algorithm. For this study, 10-fold Tikhonov regularisation [1] was used both to smooth the raw data and get the first derivative. In essence, instead of a direct derivation, this algorithm numerically solves an integral equation on the second derivative of the dataset, using parameters that minimize the error from the experimental dataset. The optimization is carried out through applying the algorithm on 90% of the data points, then comparing the outcome of the fitting to the 10% remaining points. The set of parameters giving the lowest error is kept to process the whole set of data. The output can then easily be used for further fitting or processing.

This fitting of the first derivative is then carried out using a least squares method. To ensure that the fitting function is appropriate to describe the material behaviour, the fitting can be done on a forward extending time windows. Fitting is carried out iteratively increasing the amount of considered data points forward in time. The convergence of the fitting coefficients and RMSE is then analysed. The stability of the coefficients and reduction, or at least stability, of the RMSE are indicators that the fitting function is adapted to the problem.

In the present study, considering the experiment duration (28 days), the maturity of the samples at loading (28 days as well) and the load level (10% to 15% of the strength) the obtained data should fall in the period of short-term basic creep and therefore could be efficiently fitted with a power law. However, the data is approximated both with a power law or a logarithm to determine which function is best suited to the experimental framework. The main difference between these functions is their long-term behaviour. Indeed, as logarithmic functions eventually increase slower than any other function, strain predictions made using a power law will be higher than when using a logarithm. As long-term predictions are well beyond the scope of this study, either functions should be adapted to interpret and model the phenomena within the considered time frame.

A.1 References

- [1] AS Lubansky et al. "A general method of computing the derivative of experimental data". *AIChE journal* 52.1 (2006), pp. 323–332.

B Data on concrete

Compressive creep tests were carried out on some concrete specimens during this research project. Mix designs and experimental results are summarized in this appendix.

B.1 Materials and method

Cement used was Heidelberg *LabCement*, with *Durcal 5* Limestone, and either 66% calcined kaolinite content clay from South America or 45% from South Asia. The LC³ binders had a 2:1 calcined clay to limestone ratio. The aggregates used were Swiss siliceous aggregates from riverbed, with a maximal diameter of 16 mm and a granulometry satisfying the SN EN 206-1 standard. Table B.1 summarizes the mix properties of the studied concretes.

Table B.1 – Summary of the mix designs, curing procedure and mechanical strength of the concrete samples used for compressive creep tests. U stands for underwater cure and S for sealed cure.

Sample name	W/B	Binder dosage [kg/m ³]	Curing time	Comp. Str. (28d) [MPa]
PC 0.45-340	0.45	340	28d (U)	64.1
LC3-50 (66%) 0.45-340	0.45	340	28d (U)	68.3
PC 0.45-340	0.45	340	90d (S)	63.1
LC3-50 (45%) 0.6-300	0.6	300	90d (S)	31.6
LC3-65 (45%) 0.6-350	0.6	350	90d (S)	42.1

B.2 Experimental results

Figure B.1 shows the results of basic compressive creep and autogenous shrinkage measurement tests. At similar mix design by mass, LC³ concrete has a dramatically lower compliance. On this aspect, tests carried out at the paste and concrete scales are qualitatively comparable.

Appendix B. Data on concrete

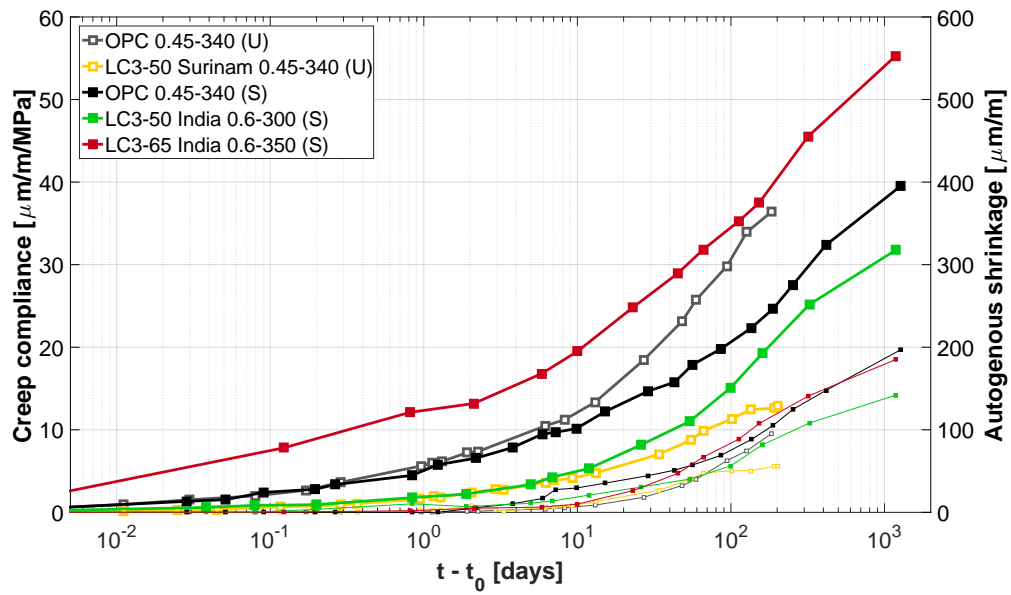


Figure B.1 – Basic creep compliance and autogenous shrinkage of tested concrete. Hollowed symbols are used for the samples cured underwater for 28 days, solid symbols for the 90 days sealed cure. Thick lines represent creep compliance and thin lines autogenous shrinkage.

List of publications

Journal papers

- J. Ston and K. Scrivener, "Basic creep of Limestone - Calcined Clay Cements: an experimental and numerical approach", submitted to *Theoretical and Applied Fracture Mechanics*.
- Z. Hu, A. Hilaire, J. Ston, M. Wyrzykowski, P. Lura and K. Scrivener, "Intrinsic viscoelasticity of C-S-H assessed from basic creep of cement pastes", *Cement and Concrete Research*, vol. 121, pp. 11-20, July 2019.
- K. Scrivener, F. Avet, H. Maraghechi, F. Zunino, J. Ston, W. Hanpongpun, A. Favier, "Impacting factors and properties of limestone calcined clay cements (LC3)", *Green Materials*, pp. 1–12, Nov. 2018.
- A. Terrier, J. Ston, A. Dewarrat, F. Becce, and A. Farron, "Dégénérescence des muscles de la coiffe des rotateurs dans l'arthrose primaire. Mesure par tomodensitométrie quantitative semi-automatisée", *Revue de Chirurgie Orthopédique et Traumatologique*, vol. 103, no. 2, pp. 113–119, Apr. 2017.
- A. Terrier, J. Ston, A. Dewarrat, F. Becce, and A. Farron, "A semi-automated quantitative CT method for measuring rotator cuff muscle degeneration in shoulders with primary osteoarthritis", *Orthopaedics & Traumatology: Surgery & Research*, vol. 103, no. 2, pp. 151–157, Apr. 2017.
- A. Terrier, J. Ston, and A. Farron, "Importance of a three-dimensional measure of humeral head subluxation in osteoarthritic shoulders", *Journal of Shoulder and Elbow Surgery*, vol. 24, no. 2, pp. 295–301, Feb. 2015.
- U. Kettenberger, J. Ston, E. Thein, P. Procter, and D. P. Pioletti, "Does locally delivered Zoledronate influence peri-implant bone formation? – Spatio-temporal monitoring of bone remodeling in vivo", *Biomaterials*, vol. 35, no. 37, pp. 9995–10006, Dec. 2014.

Conference papers

- J. Ston and K. Scrivener, "Basic creep of LC3 paste: links between properties and microstructure", submitted to *3rd Conference on Calcined Clay for Sustainable Concrete*, 15-17 October 2019, New Delhi (India).
- J. Ston and K. Scrivener, "Autogenous shrinkage and creep of LC3 cement paste", submitted to *15th International Congress on the Chemistry of Cement*, 16-20 September 2019, Prague (CZ).
- J. Ston and K. Scrivener, "Autogenous shrinkage and creep of LC3 cement paste", *Conference for the Centennial of LMC*, 19-22 August 2018, Lausanne (CH).
- J. Ston, A. Hilaire and K. Scrivener, "Autogenous shrinkage and creep of limestone and calcined clay based binders", *2nd Conference on Calcined Clay for Sustainable Concrete*, 5-7 December 2017, La Havana (Cuba).
- J. Ston, A. Hilaire and K. Scrivener, "Delayed strains in limestone and calcined clay blended cement", *36th Cement and Concrete Science Conference*, 5-6 September 2016, Cardiff (UK).

Julien STON

Avenue de la Poste 19c
1020 Renens

+41 79 721 32 90 (mobile)
julien.ston@alumni.epfl.ch

Birth date: 08.10.1986
Swiss nationality

EDUCATION

- From Sept 2014** **Swiss Federal Institute of Technology (EPFL), Lausanne (CH)**
LMC (Laboratory of Construction Materials)
PhD thesis within the LC³ project : shrinkage and creep of limestone and calcined clay cements, supervised by Prof. K. Scrivener and including:
- Supervision and teaching of construction materials classes, student projects and laboratory works
 - Teacher-assistant for the *Numerical Analysis* class
 - Teacher for the 2018 ICRC Cement and Concrete Applications Course
- 2008 - 2011 (Sept)** **EPFL, School of Engineering (STI)**
Master in Materials Science and Engineering
Orientation: *Structural materials for use in transport, energy and infrastructure*
Minor in Space Technology
- 2005 - 2008** **EPFL (STI) Bachelor in Materials Science and Engineering**
- 2002 - 2005** **Maturité fédérale (bilingual fr-eng) with merit, Lycée Denis-de-Rougemont, Neuchâtel (CH)**
Orientations: *Physics and Applied Mathematics (SO) and Chemistry (CO)*

WORK EXPERIENCES

- 2011 (Dec) – 2014 (Aug)** **LBO (Laboratory of Biomechanics and Orthopaedics, EPFL)** Scientific collaborator in a joint project between EPFL, CHUV and Tornier on 3D models of the shoulder, involving:
- Building of patient-specific shoulder models, using clinical CT and reconstruction tools (Amira, Geomagic, Solidworks)
 - Evaluation of the stresses in the bone and implant of prosthetic shoulders (Abaqus)
 - Development of a software for surgeons to evaluate bone wear prior to shoulder replacement (Matlab)
 - Scientific papers writing and presentations at specialized congresses
 - Management of student projects
- 2011 (Apr – Nov)** **LMC (EPFL)** Master Thesis: Study of composite cement containing burned oil shale. Collaborative project with *Holcim Suisse*, including:
- Preparation and mechanical testing of concrete sample
 - Preparation of concrete and cement samples for SEM study
 - SEM analysis of ITZ in concrete
 - Granulometric, MIP, XRD, TGA and calorimetric analysis of cements
- 2010 (autumn)** **LMC (EPFL)** Exploratory project on clinkers for Holcim Swiss, including SEM study of cements and calorimetry
- 2009 (Sept) - 2010 (Jul)** **LSMX (Computational Materials Laboratory, EPFL)** Student-assistant for the course *Introduction to Material Science* for 1st year STI students 131

2009 (summer)	LMC (EPFL) Laboratory work assistant for PhD students
2008 (Nov) - 2009 (Mar)	LSMX (EPFL) Internship as student-assistant on the European project Impress. 2D modelling of TiAl solidification front
2007 (Aug)	ETML (École Technique et des Métiers de Lausanne) Machining training

RESEARCH PROJECTS (EPFL)

2011 (summer)	Master Thesis: Study of composite cement containing burned oil shale (<i>LMC – Laboratory of Construction Materials</i>)
2010 (autumn)	Damping behaviour of melt-spun NiMnGa magnetic shape-memory alloy composites (<i>LTC – Laboratory of Composites and Polymers Technology</i>)
2010 (spring)	Conceptual design of a composite propellant tank (<i>Space Centre</i>)
2009 (autumn)	Possibilities of using alkali-activated materials as a binder in wood acoustics panels (<i>LMC</i>)
2009 (spring)	Study of model cements containing gypsum in different quantities (<i>LMC</i>)
2008 (spring)	AFM study of polymer brushes (<i>LP – Laboratory of Polymers</i>)
2008 (autumn)	Innovations in transparent conductive films for flexible screens and solar cells (<i>LTC</i>)

LANGUAGES

French	Native language
Italian	Fluent (C2)
English	Fluent (C1-C2)
German	School knowledge (B1)
Japanese	Basic (A2)

SKILLS

Programming	C, C++, Basic
Software	MS Office, Mathematica, Catia, Solidworks, Abaqus/CAE, Amira, Matlab, Adobe Photoshop, Adobe Lightroom

INTERESTS

Sports	Running, hiking, swimming, martial arts, archery
Social activities	Volunteer or committee in several events (Gaming Federation, EPFL Astronomy club, EPFL Photo Club, Japan Impact [VD], Parabôle [NE]), photographer in public events (Balélec [VD], ParaBôle [NE]) Writer at Semper Ludo (video games reviews)
Others	Photography, Japanese culture, fantasy literature, folk dance

